INFORMATION TO USERS

This material was produced from a microfilm copy of the original document. While the most advanced technological means to photograph and reproduce this document have been used, the quality is heavily dependent upon the quality of the original submitted.

The following explanation of techniques is provided to help you understand markings or patterns which may appear on this reproduction.

1. The sign or "target" for pages apparently lacking from the document photographed is "Missing Page(s)". If it was possible to obtain the missing page(s) or section, they are spliced into the film along with adjacent pages. This may have necessitated cutting thru an image and duplicating adjacent pages to insure you complete continuity.

2. When an image on the film is obliterated with a large round black mark, it is an indication that the photographer suspected that the copy may have moved during exposure and thus cause a blurred image. You will find a good image of the page in the adjacent frame.

3. When a map, drawing or chart, etc., was part of the material being photographed the photographer followed a definite method in "sectioning" the material. It is customary to begin photoing at the upper left hand corner of a large sheet and to continue photoing from left to right in equal sections with a small overlap. If necessary, sectioning is continued again — beginning below the first row and continuing on until complete.

4. The majority of users indicate that the textual content is of greatest value, however, a somewhat higher quality reproduction could be made from "photographs" if essential to the understanding of the dissertation. Silver prints of "photographs" may be ordered at additional charge by writing the Order Department, giving the catalog number, title, author and specific pages you wish reproduced.

5. PLEASE NOTE: Some pages may have indistinct print. Filmed as received.

75-10,468

CANNATA, Robert Frank, 1944-
SPECTRAL ANALYSIS OF BIOLOGICAL SIGNALS USING
COHERENT OPTICAL TECHNIQUES.

Iowa State University, Ph.D., 1974
Engineering, electrical

Xerox University Microfilms, Ann Arbor, Michigan 48106

Spectral analysis of biological signals

using coherent optical techniques

by

Robert Frank Cannata

A Dissertation Submitted to the

Graduate Faculty in Partial Fulfillment of

The Requirements for the Degree of

DOCTOR OF PHILOSOPHY

Departments: Electrical Engineering
Biomedical Engineering

Approved:

In Charge of Major Work

For the Major Departments

For the Graduate College

Iowa State University
Ames, Iowa

1974

TABLE OF CONTENTS

INTRODUCTION

Within the last three decades, researchers in the life sciences have been adopting many of the mathematical tools and processing techniques initially developed in the physical sciences for analyzing signals derived from physical systems. By applying these methods, the life science researcher has acquired powerful techniques for analyzing and characterizing biological signals which have enhanced the study of living systems. An objective of this dissertation is to apply a relatively new computing technique, namely coherent optical data processing, to the analysis of biological signals.

There are essentially two distinct but related methods of representing a real one-dimensional signal; by its time domain description or by its frequency domain distribution. The time domain description specifies the amplitude of the signal at each instant of time, while the frequency domain distribution specifies the amplitude and phase of the various orthogonal frequency components of the signal. Each representation has specific advantages that are dependent upon the application or information to be derived from the signal, but either representation uniquely defines the signal.

The time domain description of a signal and its frequency domain distribution are related by the mathematical concepts of Fourier analysis. Fourier series analysis is a method for representing a physically realizable one-dimensional periodic function by an infinite sum of weighted sinusoidal functions. If $g(t)$ is a periodic function with a period T, and is defined for all time t, then the Fourier series representation is

$$g(t) = a_0 + \sum_{n=1}^{\infty} (a_n \cos 2\pi n f_0 t + b_n \sin 2\pi n f_0 t) \tag{1}$$

where $f_0 = 1/T$ is called the fundamental frequency, n is an integer, and the coefficients a_0, a_n, and b_n are given by

$$a_0 = \frac{1}{T} \int_{-T/2}^{T/2} g(t) dt \tag{2}$$

$$a_n = \frac{2}{T} \int_{-T/2}^{T/2} g(t) \cos(2\pi n f_0 t) dt \tag{3}$$

$$b_n = \frac{2}{T} \int_{-T/2}^{T/2} g(t) \sin(2\pi n f_0 t) dt \tag{4}$$

This Fourier series can also be written in a more compact form by replacing the sinusoidal functions with their exponential equivalents. The resultant series is

$$g(t) = \sum_{n=-\infty}^{\infty} c_n \exp[j2\pi n f_0 t] \tag{5}$$

where

$$c_n = \frac{1}{T} \int_{-T/2}^{T/2} g(t) \exp[-j2\pi n f_0 t] \, dt \tag{6}$$

and where coefficient c_n is related to a_n and b_n by

$$c_n = \frac{1}{2}(a_n - jb_n)$$

$$c_{-n} = \frac{1}{2}(a_n + jb_n) \tag{7}$$

with $c_0 = a_0$.

The Fourier series decomposes a periodic function into its components at various frequencies including d-c. The nonzero frequencies (nf_0) are integer multiples of the fundamental frequency (f_0) and are called the harmonic frequencies. Thus, a periodic function is represented by a spectrum of frequencies. If g(t) is specified, its frequency spectrum can be determined, and conversely, if the frequency spectrum is known, the periodic function can be determined. The convenience of Fourier series analysis is that each sinusoidal component may be handled by the familiar mathematical properties and operations governing sinusoidal calculations.

If the period, T, of a function is large, then the fundamental frequency will be small. As the fundamental frequency becomes smaller, the separation between harmonic frequencies will also become smaller. For a nonperiodic function (a function whose period can be viewed as being infinite) the separation between harmonics is infinitesimal. The time domain and the frequency domain for this type of function are related by the Fourier integral equations

$$g(t) = \int_{-\infty}^{\infty} \underline{G}(f) \exp[j2\pi ft] \, df \tag{8}$$

and

$$\underline{G}(f) = \int_{-\infty}^{\infty} g(t) \exp[-j2\pi ft] \, dt \tag{9}$$

where $\underline{G}(f)$ is the Fourier transform or frequency spectrum of g(t), and f is a continuous frequency variable. The Fourier integral equations are simply an extension of the concepts of Fourier series to a nonrepeating situation. Equations 8 and 9 form a Fourier transform pair and are

exactly analogous to the Fourier series pair given by Equations 5 and 6. Quantitative information concerning the frequency content of a signal may be conveniently determined from its frequency domain distribution. Also, since signals with different time domain descriptions have different frequency distributions, signals may be classified and compared by their frequency spectrums.

Conversely, signals may also be compared in the time domain on the basis of similarity of waveforms. The crosscorrelation function provides such a measure by relating the similarity of two signals as one signal is shifted in time with respect to the other. If $g_1(t)$ and $g_2(t)$ are two real signals, then the crosscorrelation function may be defined as

$$\psi_{12}(\tau) = \int_{-\infty}^{\infty} g_1(t)g_2(t-\tau) \, dt \tag{10}$$

where τ is the time shifting or displacement parameter. If the two signals are similar, the crosscorrelation function will be nonzero over some range of τ. If the crosscorrelation function is zero for all τ, the two signals are said to be uncorrelated.

A detailed discussion of correlation and Fourier transform theory is beyond the intent of this section. For further discussions concerning these subjects, the reader should consult a reference such as: Lee [1]; Lathi [2]; Bracewell [3]; or Papoulis [4].

As previously stated, researchers in the life sciences have been adopting the mathematical tools and techniques used extensively in the physical sciences for analyzing signals. They are increasingly using the techniques of frequency spectral analysis and crosscorrelation to charac-

terize and compare biological signals. Some examples of this type of research activity include: spectral analysis of the normal resting electrocardiogram [5]; electroencephalogram spectral signatures from normal and dyslexic children [6]; energy spectra of heart sounds [7]; and cross-correlation analysis of the spontaneous electrical activity in nerves [8].

Prior to adopting these processing techniques, the analysis of physiological signals had been more of an art than a science. The conventional method of analysis consisted of visually inspecting the recorded signals, and when performed by experienced persons this had been an acceptable technique. However, it was difficult to obtain accurate quantitative spectral information about the signal, and this difficulty increased as the quantity of recorded information increased.

With the development of sophisticated and reliable electronic systems, the analysis of physiological signals has become much more quantitative. The mathematical processing of these signals has been accomplished for the most part with the aid of digital computer systems using program algorithms such as the Fast Fourier Transform (FFT). The FFT is basically an efficient method for computing the discrete Fourier transform of a digitized section of a signal waveform.

A major problem exists in that experimental and clinical biologists and physiologists are often interested in the analysis of very long signal records. In spite of advantageous algorithms such as the FFT, the processing of data records may become time consuming and prohibitively expensive when performed by a digital computer. A compromise is usually made at this point by selecting a representative section of the signal to be processed and analyzed. It is often assumed that the information con-

tent in this small section of data is statistically the same as that contained in the entire data record. In some cases this may be a valid assumption, but in many cases subtle changes occur over a period of time in signals recorded from living systems. These changes may be the result of experimental stimuli or events naturally and uncontrollably occurring within the system or its environment. Coherent optical data processing techniques provide a solution to this processing and analyzing problem.

The mathematical and physical principles of optical computing are based primarily on the phenomenon of diffracted coherent monochromatic light and the inherent optical properties of a thin converging lens. The information to be processed by this technique must be recorded on an optical transparency as a spatial light amplitude variation. Illuminating this transparency with coherent monochromatic light will result in the light being diffracted in a manner determined by the amplitude and phase at each point on the back side of the transparency. The effect of the thin converging lens is to focus the diffraction pattern on an appropriate plane behind the lens. The resultant amplitude and phase of the light distribution across this plane is directly proportional to the two-dimensional Fourier transform of the light amplitude transmitted by the input transparency.

An optically produced one-dimensional Fourier transform is a special case of this two-dimensional transformation. Optical processing of one-dimensional data, such as biological signals, requires an initial conversion of the signal into the spatial domain. This may be accomplished by properly recording the signal on an optical transparency such that the light amplitude transmittance as a function of one spatial coordinate is

directly related to the signal amplitude as a function of time. Illuminating this transparency with coherent light will produce a Fourier transform pattern behind the converging lens. The light amplitude distribution along one spatial coordinate in the transform plane will be directly related to the one-dimensional Fourier transform of the input signal.

Coherent optical processing techniques provide spectral information in a continuous form. In addition, once the signal has been recorded on an appropriate input format, it provides nearly instantaneous spectral information for any section of record the user wishes to view.

The main objectives of the research presented in this dissertation are twofold. The first objective is to demonstrate the feasibility and practicality of using coherent optical techniques to spectrally analyze biological signals such as the electrocardiogram (ECG), electroencephalogram (EEG), blood flow and blood pressure waveforms. These signals were obtained from canine experimental animals and were selected on the basis of being typical physiological signals. Various data input formats, using photographic film as the recording medium, are discussed and demonstrated. Spectrum plots of an optically processed ECG signal using various input formats are given and the results are compared with a digital computer calculated spectrum of the same signal.

The second objective of this research is to apply the inherent two-dimensional parallel processing capabilities of a coherent optical computing system in developing a technique to simultaneously process two signals. It will be shown that spectral information pertaining to each individual signal, and information concerning the correlation between signals may easily be determined by this technique.

LITERATURE REVIEW

The optical processing of information has been understood for nearly a century, but it remained relatively impractical until the advent of the laser as a source of intense monochromatic coherent light. The great power of coherent optical computing is derived primarily from the natural property of a lens to perform parallel processing of information that contains two-degrees of freedom. Thus, the primary applications of coherent optical computers have been in processing two-dimensional data such as photographs and synthetic aperture radar signals. Although the extent to which coherent optical information processing is being employed has been limited, the list of applications is rapidly growing. Optical computing may have a revolutionary impact on almost every field of science. Excellent reference texts on this developing field include: Goodman [9]; Preston [10]; Stroke [11]; and Shulman [12].

Many of the coherent optical processing techniques are based upon the holographic principles first proposed by Gabor [13,14]. In 1948, Gabor proposed a method for recording and regenerating the amplitude and phase of a wavefront by combining this wavefront with a coherent reference wave. The original concept was invented to correct the aberrations and thus improve the resolution of an electron microscope. Although he was unable to demonstrate the validity of his principle with electron waves, he was able to do so using visible light. Lacking an intense source of coherent light, the image results were not of good quality but the process clearly worked. When the laser became available, Leith and Upatnieks [15] were able to demonstrate the principles of holography outlined by Gabor. While

the application of holography to the electron microscope has not yet been successful, holography has been successfully applied to other areas of science and technology [16,17].

Coherent optical processing, from a purely mathematical point of view, is an extension into the two-dimensional space domain of the theories and concepts used in the time domain by communications and other systems engineers and scientists. Optical processing systems employ many mathematical concepts that are analogous to the design of electrical filtering systems [18]. A primary advantage of optical techniques over electrical or digital processing is best realized when the information to be processed contains two degrees of freedom such as a photograph or multichannel one-dimensional information.

Cutrona et al. [19] have outlined many of the fundamental principles and techniques useful in understanding and designing coherent optical systems. A coherent optical computer basically consists of a source of coherent monochromatic light, a spatial filter, and a thin convex lens. The information to be processed is usually recorded on an optical transparency such as photographic film. The data is recorded on film as an amplitude transmittance variation. If this transparency is placed at the front focal plane of the lens and is illuminated by collimated coherent monochromatic light, a resultant diffraction pattern will be produced at the back focal plane. The light amplitude of this diffraction pattern will have all the properties of the Fourier transform of the input spatial information. The spatial location of the back focal plane is called the transform or frequency plane.

The fundamental operation which can be performed by a coherent optical computer is the Fourier transform of an input pattern. A successive Fourier transform can easily be implemented by placing a second thin convex lens a distance of one focal length beyond the transform plane. The second lens performs a two-dimensional Fourier transform on the light amplitude distribution in its front focal plane. The resultant transform is displayed as a light amplitude distribution at the back focal plane of this second lens. However, since the transform of a transform of a function is the original function spatially inverted, the final reconstructed image is the same as the original input image except for possibly a magnification factor. If the diffraction pattern in the transform plane is altered, as for example, by blocking the light corresponding to certain spatial frequencies, then the reconstructed image will contain all the information of the original input image except for that which has been removed in the transform plane. This is the basis for optical spatial filtering, and is analogous to filtering of electrical signals.

In its simplest form, a spatial filter may consist of a slit formed by two opaque surfaces. The construction of spatial filters with sharp band-pass, high-pass, or low-pass characteristics are easily implemented. More complicated spatial filters can be realized by placing a transparency in the frequency plane of the optical computing system. The applications of spatial filtering as a method to process information were greatly increased when Vander Lugt [20] proposed a holographic method to produce complex spatial filters. With this ability to produce complex spatial filters, the mathematical techniques of correlation and convolution for two-dimensional data can be realized in an optical system.

The ability to perform spatial filtering, optical correlation, and also spatial frequency processing for two-dimensional data has led to many diverse applications of coherent optical processing. Preston [21] describes a sample of the many successful applications. These include: spectral analysis for pattern recognition in location of chromosome spreads on microscope slides; word recognition using matched filtering of speech spectrograms of spoken words; and fingerprint identification using matched filtering.

Alphanumeric character recognition by complex spatial filtering is another application of optical processing. Hård and Feuk [22] have investigated the possibility of constructing an optical character recognition reading machine for the blind. Their results have indicated that it is possible to build a reading machine capable of reading one printed character at a time with sufficient accuracy for most reading purposes. The only obstacle to making this instrument practical is the construction of an appropriate input device.

The concept of correlation between two images has been utilized to produce automatic terrain profiling systems [23]. The information content of the transform plane of an optical system is in a form that is exceptionally convenient for frequency analysis. The application of frequency spectrum analysis of pictorial information has been applied effectively in the earth and space sciences [24,25].

Many applications of coherent optical processing have dealt with image enhancement. Stroke and Halioua [26] have been successful in further increasing the sharpness of images obtained from a ultra-high resolution electron microscope. These results have significantly improved

the effective resolution capabilities of the microscope. Although this technique is not the holographic procedure outlined by Gabor, it is a great step in improving electron microscope image resolution. Other researchers [27] have applied their efforts to image enhancement of medical x-ray photographs. They have improved the resolution and contrast of x-ray photographs by filtering in the frequency plane to compensate for the extended x-ray source inherent for all x-ray generating tubes.

Image processing, such as enhancement, can also be performed by digital computers. Andrews et al. [28] presents a concise summary of the digital processing approach. The computational requirements in digital processing has been greatly reduced by the Fast Fourier Transform (FFT) algorithm. Even with this advantage, however, processing of two-dimensional data requires digital computers with large memories and often results in long computing times. Optical processing, with its inherent two-dimensional parallel processing capability offers a distinct advantage over digital computation in terms of speed. Preston [21] gives a comparison between present optical analog and digital techniques for pattern recognition. An equivalent performance comparison is given in bits/second/dollar which shows that present optical processors are superior to the general purpose computer by a factor of approximately 10^3. In another comparison between optical and digital picture processing, Stroke [29] has indicated the superiority of optical processing to restore sharpness to images that have been blurred by such parameters as movement, atmospheric turbulence, improper focusing, or instrument imperfections.

To take advantage of the capabilities of both optical and digital processing, Casasent [30] has proposed an on-line hybrid digital/optical

computer system to process two-dimensional data. The control of the system and the decision making operations are handled by a programmable digital computer. The fundamental operations of Fourier transform and spatial filtering are performed by a coherent optical system. An on-line image forming light modulating device is used to input data into the processing system.

In nearly all the applications of coherent optical computing reported above, the researchers have concerned themselves with the processing of two-dimensional data. Indeed, a vast majority of the applications reported to date have dealt with processing this type of data. Coherent optical systems have the inherent power to parallel process in two dimensions, and not to capitalize on such a property would be a grave mistake. The important point here is that coherent optical systems also have the power to process one-dimensional data. Many of the advantages and properties of optical processing, such as parallel processing, reduced computation time for frequency spectrum processing, filtering, correlation, and convolution, can also be realized for one-dimensional data.

To capitalize on the Fourier transform properties of a coherent optical system, a technique for optically processing time varying signals has been investigated by Pernick et al. [31]. The input signals, used in this study, modulated the light intensity of an undeflected CRT beam. This intensity variation was continuously recorded on film as a transmittance variation, the developed film was then illuminated by a coherent laser beam and the diffracted light was collected by a transform lens. The light amplitude distribution in the back focal plane of the lens was

directly proportional to the Fourier transform of the input transmittance variation. An alternate and much more simplified method for recording time varying signals on film has been used by Felstead [32]. This method is area modulation and is the technique commonly used to record the sound track on motion picture films. The principle behind area modulation is that a one-dimensional signal may be represented spatially by an aperture in an opaque screen where the aperture width is proportional to the signal. When such an area modulated aperture is placed in the input of a coherent optical system, the light amplitude along one axis in the transform plane is directly proportional to the Fourier transform of the original function. Area modulation recording as opposed to film density modulation represents one way to permit relaxation of the exposure and processing requirements of the film. In area modulation, transmissions of only 0 and 1 are required, and exposure and processing need only be such as to satisfy these binary requirements.

The application of coherent optical techniques to the processing of physiologically derived electrical signals has been quite limited. Anderson and Everett [33] describe a technique for recording twenty-five channels of physiological data. This data represents spatially localized time-varying quantities and is processed for frequency content by coherent optical methods. Details of a prototype device used for directly recording parallel channels of physiological data in a density modulated format are given. The ultimate goal of this processing technique is to reduce the data handling expense in both research and clinical physiological data analysis.

Often physiological signals are recorded as conventional ink tracings and it is customary to analyze these curves by visual observation. Such a representation does contain all the information carried by the signal, provided the frequency response of the recorder is adequate. However, it is sometimes difficult to obtain accurate quantitative information using this type of processing. Taylor et al. [34] have presented a method for obtaining spectral information from signals recorded as conventional ink tracings. The theory behind this method assumes the transmission characteristics of a photograph of the ink tracings may be approximated by a continuous two-dimensional impulse function. By placing this transparency in the input of a coherent optical computing system, it is possible to obtain spectral information about the recorded signal. The advantages of this method are that no special recording apparatus is required, and the film development is not critical since there are no shades of gray to be produced. The disadvantage of this technique is that the accuracy of the spectral information is questionable.

The main drawback for using coherent optical processing techniques is the difficulty to input data into the system to perform nearly real-time data processing. In most applications, photographic film is the medium used to input data into the optical system. Photographic film offers the advantages of low cost and high resolution, but the possibility of performing real-time data analysis is not achievable. New devices and methods such as membrane light modulators, elastooptic delay lines, thermoplastic films, and photochromatic materials are being studied [10]. In terms of future developments and applications, the most dramatic results will likely come from the implementation of real-time data processing for two-dimensional and also one-dimensional data.

PART I. ONE-DIMENSIONAL ANALYSIS

THEORETICAL AND PRACTICAL CONSIDERATIONS

Optical Processing

The basic mathematical and physical concepts useful in understanding coherent optical processing will be presented in this section. For a more rigorous theoretical development, the reader should consult a reference such as Goodman [9].

The foundation of optical processing is based upon the diffraction of coherent monochromatic light by an aperture, but exact mathematical calculations of diffraction patterns are often extremely complicated. To reduce this complexity, a number of simplifying assumptions and approximations are usually made. The initial assumption is to treat light as a scalar phenomenon such that only the scalar amplitude of one transverse electric or magnetic field component is considered. The conditions that the diffracting aperture is large compared to the wavelength (λ) of illumination, and that the diffracted fields are observed far from the aperture are also assumed. Other approximations to this scalar diffraction theory are made so that calculations of the diffracted light amplitude distributions will reduce to more familiar mathematical manipulations. These approximations are referred to as the Fresnel (near-field) and the Fraunhofer (far-field) approximations.

In order to describe the phenomenon of diffracted light, the wave nature of light must be considered. The electric field of an incident wave at a position (x,y,z) and time t can be represented by the scalar function $u(x,y,z,t)$. If this function is an optical wave, then it must satisfy the scalar wave equation

$$\nabla^2 u - \frac{1}{c^2} \frac{\partial^2 u}{\partial t^2} = 0 \tag{1-1}$$

where c is the velocity of light and ∇^2 is the Laplacian operator. If this light wave is monochromatic of optical frequency ν, then a solution to Equation 1-1 is the sinusoidal scalar field

$$u(x,y,z,t) = U(x,y,z) \cos[2\pi\nu t + \phi(x,y,z)] \tag{1-2}$$

where $U(x,y,z)$ and $\phi(x,y,z)$ are the amplitude and phase, respectively, of the wave at position (x,y,z). Equation 1-2 may be written in a more compact form using the complex notation[1]

$$u(x,y,z,t) = \text{Re}[\underline{U}(x,y,z) \exp(-j2\pi\nu t)] \tag{1-3}$$

where Re [] indicates the real part of the complex quantity within the brackets and $\underline{U}(x,y,z)$ is the phasor notation for the complex amplitude function of position. The phasor $\underline{U}(x,y,z)$ is given by

$$\underline{U}(x,y,z) = U(x,y,z) \exp[-j\phi(x,y,z)] \tag{1-4}$$

To simplify the mathematical operations and descriptions to follow, coherent[2] monochromatic illumination will be represented by this phasor notation.

It would be instructive at this point to consider the phasor form for particular types of illumination. Consider first a uniform plane wave of amplitude A and wavelength λ propagating in the positive z direction. The complex amplitude function for such a wave is

---

[1]An underline will be used to indicate a complex function.

[2]The term coherent implies a particular type of illumination such that the phase relationship between stationary points in the light beam are invariant with time.

$$U(x,y,z) = A \exp(jkz) \tag{1-5}$$

where k is the wave number given by

$$k = 2\pi/\lambda \tag{1.6}$$

A spherical wave at a point $p_1(x_1,y_1,z_1)$ diverging from a point

$p_0(x_0,y_0,z_0)$ can be represented as

$$\underline{U}(x_1,y_1,z_1) = \frac{A}{r_{01}} \exp(jkr_{01}) \tag{1-7}$$

where r_{01} is the distance from p_0 to p_1. Similarly, a spherical wave at a

point $p_0(x_0,y_0,z_0)$ converging to a point $p_1(x_1,y_1,z_1)$ can be represented

as

$$\underline{U}(x_0,y_0,z_0) = \frac{A}{r_{01}} \exp(-jkr_{01}) \tag{1-8}$$

The diffraction of coherent monochromatic light by an infinite opaque

screen containing a finite aperture (Figure 1) will now be considered.

The dimensions of this aperture are assumed to be large in comparison to

the illuminating wavelength. Also, the screen is assumed to be planar and

located in a rectangular coordinate system $(x_0,y_0,0)$. The light amplitude

transmittance function for the screen may be defined as

$$t_0(x_0,y_0) = \begin{cases} 1 & \text{for } (x_0,y_0) \text{ within the aperture} \\ 0 & \text{otherwise} \end{cases} \tag{1-9}$$

If the complex light amplitude incident on the screen is given by

$\underline{U}_0'(x_0,y_0)$, then the complex light amplitude across the plane immediately

behind the screen is

$$\underline{U}_0(x_0,y_0) = \underline{U}_0'(x_0,y_0)\, t_0(x_0,y_0) \tag{1-10}$$

The observation plane shown in Figure 1 is assumed to be in plane

parallel to the plane of the screen and at a distance z_1 from the screen.

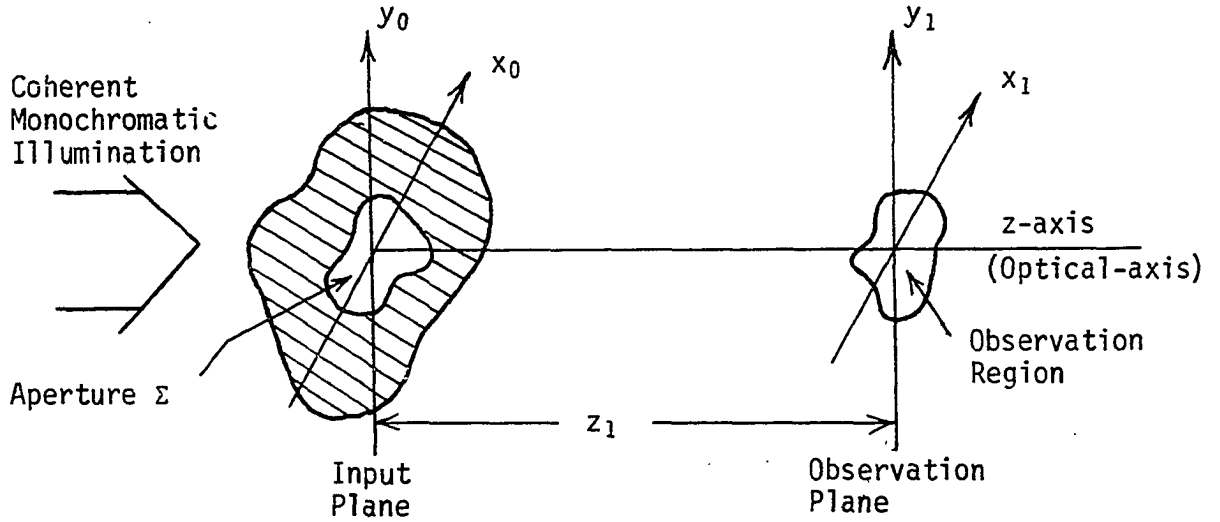Using the mathematical expression of the Huygens-Fresnel principle, the

Figure 1. Diffraction geometry for a finite aperture illuminated by coherent monochromatic illumination.

complex field amplitude at a point (x_1, y_1) in the observation plane is[1]

$$\underline{U}_1(x_1, y_1) = \frac{1}{j\lambda} \iint_\Sigma \underline{U}_0(x_0, y_0) \ \frac{\exp(jkr_{01})}{r_{01}} \ \cos\theta \ dx_0 dy_0 \qquad (1\text{-}11)$$

where the limits of integration are taken to be the boundary of the aperture Σ. The term r_{01} is the distance between the point $p_0(x_0, y_0, 0)$ in the aperture and a point $p_1(x_1, y_1, z_1)$ in the observation plane, that is,

$$r_{01} = \left[z_1^2 + (x_1-x_0)^2 + (y_1-y_0)^2\right]^{\frac{1}{2}} \qquad (1\text{-}12)$$

This distance is assumed to be much greater than the wavelength (λ). The angle θ is formed by the positive z-axis and the straight line connecting points p_0 and p_1, thus $\cos\theta = z_1/r_{01}$.

---

[1]This integral equation is called the Rayleigh-Sommerfield diffraction formula and is derived in Chapter 3 of Goodman [9].

Assuming the observation region is restricted to a finite region around the z-axis (optical axis) and the distance z_1 is much greater than the maximum linear dimensions of both the observation region and the aperture area, the following approximations can be made:

1) $\cos \theta \approx 1$

2) $r_{01} \approx z_1$ for the denominator term within the integral of Equation 1-11.

3) $r_{01} \approx z_1 + \frac{(x_1-x_0)^2}{2z_1} + \frac{(y_1-y_0)^2}{2z_1}$ for r_{01} within the exponential term of Equation 1-11.

This last approximation, often called the paraxial approximation, was determined by using the binomial expansion for r_{01} and neglecting terms beyond the second order.

If z_1 is sufficiently large for the above approximations to be valid, then the observation area is said to be in the region of Fresnel or near-field diffraction. The complex light amplitude in the observation region is given by[1]

$$\underline{U}_1(x_1,y_1) = \underline{K} \exp\left[\frac{j\pi}{\lambda z_1} (x_1^2 + y_1^2)\right] \int\int_{-\infty}^{\infty} \underline{U}_0(x_0,y_0) \exp\left[\frac{j\pi}{\lambda z_1} (x_0^2 + y_0^2)\right]$$

$$\exp\left[\frac{-j2\pi}{\lambda z_1} (x_1 x_0 + y_1 y_0)\right] dx_0 dy_0 \qquad (1\text{-}13)$$

where $\underline{K}$ is the complex term given by

$$\underline{K} = \frac{\exp[j2\pi z_1/\lambda]}{j\lambda z_1} \qquad (1\text{-}14)$$

---

[1] When a single limit of integration appears above and below a double integral, then that limit will apply to both integrations.

and the limits of integration have been extended to include all space since $\underline{U}(x_0,y_0) = 0$ outside the aperture area. By making the following substitutions

$$f_x = x_1/\lambda z_1$$

$$f_y = y_1/\lambda z_1 \tag{1-15}$$

Equation 1-13 can be written as

$$\underline{U}_1(x_1,y_1) = \underline{K} \exp\left[\frac{j\pi}{\lambda z_1}(x_1{}^2 + y_1{}^2)\right] F\left\{\underline{U}_0(x_0,y_0) \exp\left[\frac{j\pi}{\lambda z_1}(x_0{}^2 + y_0{}^2)\right]\right\}$$

$$\tag{1-16}$$

where $F\{\ \}$ is the notation for the two-dimensional Fourier transform[1] of the quantity within the brackets. Thus, aside from the multiplicative amplitude and quadratic phase term, the complex light amplitude in the observation region is given by the two-dimensional Fourier transform of $\underline{U}_0(x_0,y_0) \exp\left[\frac{j\pi}{\lambda z_1}(x_0{}^2 + y_0{}^2)\right]$, where the transform is evaluated at the spatial frequencies $f_x = x_1/\lambda z_1$ and $f_y = y_1/\lambda z_1$.

The diffraction pattern calculations may be further simplified if the Fraunhofer assumption

$$z_1 >> \frac{\pi(x_0{}^2 + y_0{}^2)}{\lambda} \text{ max} \tag{1-17}$$

---

[1]The two-dimensional Fourier transform of a function $g(x,y)$ of two independent variables, x and y, is defined as

$$F\{g(x,y)\} = \underline{G}(f_x,f_y) = \int\int_{-\infty}^{\infty} g(x,y) \exp\left[-j2\pi(f_x x + f_y y)\right] dx\ dy$$

where f_x and f_y are sinusoidal frequencies.

is adopted. Using this assumption, the quadratic phase factor,

$\exp \left[\frac{j\pi}{\lambda z_1} (x_0^2 + y_0^2) \right]$, is approximately unity over the entire aperture.

Thus, the complex light amplitude in the observation region can be found directly from the two-dimensional Fourier transform of $\underline{U}_0(x_0,y_0)$. That is

$$\underline{U}_1(x_1,y_1) = \underline{K} \exp \left[\frac{j\pi}{\lambda z_1} (x_1^2 + y_1^2) \right] F \left\{ \underline{U}_0(x_0,y_0) \right\} \qquad (1-18)$$

where the transform is evaluated at spatial frequencies $f_x = x_1/\lambda z_1$ and $f_y = y_1/\lambda z_1$.

The conditions for observing the Fraunhofer diffraction pattern place much more stringent restrictions on the geometry of the system than the approximations previously assumed. For example, if a circular aperture of radius equal to 1 cm were illuminated by light with a wavelength $\lambda = 6 \times 10^{-7}$ meter, then, according to the Fraunhofer assumption, the observation distance z_1 must be greater than 525 meters. This indicates that to observe the Fraunhofer diffraction pattern of the field distribution $\underline{U}_0(x_0,y_0)$, a large observation distance is required. Closer examination of this problem reveals a number of techniques that will allow diffraction patterns to be observed at shorter distances than implied above. Since the primary interest is in using the diffraction pattern to obtain frequency spectral information about the amplitude transmittance characteristics of the screen, one solution is to illuminate the screen with a monochromatic spherical wave that converges to a point $(0,0,b)$ behind the screen (see Figure 2). This wave can be represented, using the paraxial approximation given previously, as

$$\underline{U}_0'(x_0,y_0) = \exp \left[\frac{-j\pi}{\lambda b} (x_0^2 + y_0^2) \right] \qquad (1-19)$$
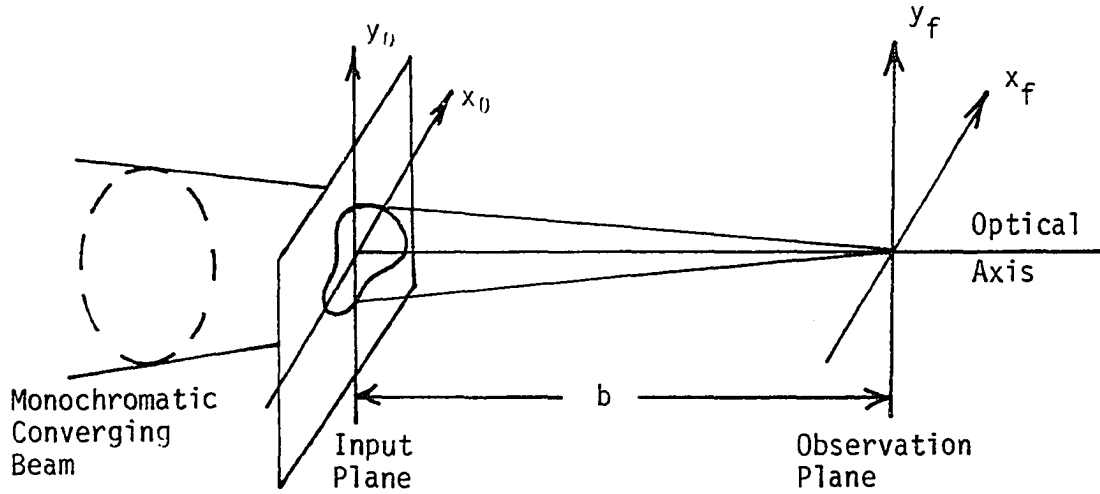
Figure 2. A method for observing the Fraunhofer diffraction pattern at a distance b behind the input plane.

where the amplitude of the wave has been normalized to unity. The field distribution behind the screen is now given by

$$\underline{U}_0(x_0,y_0) = t_0(x_0,y_0) \exp\left[\frac{-j\pi}{\lambda b}(x_0^2 + y_0^2)\right] \qquad (1\text{-}20)$$

By substituting Equation 1-20 into Equation 1-16 with $z_1 = b$ and the coordinates (x_1,y_1) replaced by (x_f,y_f), the light distribution in the observation plane is $\underline{U}_f(x_f,y_f)$ and is given by

$$\underline{U}_f(x_f,y_f) = \underline{K} \exp\left[\frac{j\pi}{\lambda b}(x_f^2 + y_f^2)\right] F\left\{t_0(x_0,y_0)\right\}$$

$$f_x = x_f/\lambda b \ , \quad f_y = y_f/\lambda b \qquad (1\text{-}21)$$

Note that the distance implied by the Fraunhofer assumption given previously is no longer required, and it is only necessary that the paraxial approximation be valid for this particular geometry. Thus the diffraction pattern in the observation plane, which can be called the frequency plane, is proportional to the two-dimensional Fourier transform of the input

amplitude transmittance function, but it is not a direct Fourier transformation because of the complex term $\underline{K} \exp\left[\frac{j\pi}{\lambda b} (x_f^2 + y_f^2)\right]$. This fact does not limit the application of coherent optical processing since in nearly all cases it is the light intensity across the frequency plane that is of prime interest. This intensity is given by

$$I(x_f, y_f) = \left|\underline{U}_f(x_f, y_f)\right|^2 = \underline{U}_f(x_f, y_f) \; \underline{U}_f^*(x_f, y_f)$$

$$= \frac{1}{\lambda^2 b^2} \left| F \left\{t_0(x_0, y_0)\right\} \right|^2$$

$$f_x = x_f/\lambda b \; , \quad f_y = y_f/\lambda b \tag{1-22}$$

where $\underline{U}_f^*(x_f, y_f)$ is the complex conjugate of $\underline{U}_f(x_f, y_f)$. The characteristics of light detectors, including the human eye, photographic film, and photocells, are such that they respond only to the intensity of light. By using such a detector to observe, record, or measure the intensity distribution, knowledge of the energy density spectrum[1] of the input amplitude transmittance function may be obtained.

Alternate solutions to the problem of observing the Fraunhofer diffraction pattern of an input transmittance function involve using a thin converging lens. This lens is assumed to be sufficiently thin such that it modifies only the phase of the normally incidence light, and a ray incident at a point (x,y) on the front surface of the lens will exit the back surface at the same coordinates (x,y).

---

[1] Some authors choose to use the term Weiner spectrum to describe this distribution. Others use "power spectrum" to indicate the squared amplitude of the Fourier transform, and this is the correct terminology if the function is periodic. For aperiodic nonrandom functions of finite length, the squared amplitude of the Fourier transform is directly related to the energy density spectrum of the function, and the term power spectrum is not technically applicable.

Considering only paraxial rays[1], a thin converging lens of focal length F_L can be represented by the amplitude transmittance function[2]

$$\underline{t}_L(x,y) = \underline{K}_1 \exp\left[\frac{-j\pi}{\lambda F_L}(x^2 + y^2)\right] P(x,y) \tag{1-23}$$

where $\underline{K}_1$ is a constant phase delay term due to the lens material and thickness, and $P(x,y)$ is an aperture function signifying the finite aperture dimensions of the lens. This function, $P(x,y)$, is defined as being unity for coordinates (x,y) within the lens aperture and zero elsewhere. If the normally incident light on this lens is $\underline{U}'(x,y)$, then the distribution of light immediately behind the lens is $\underline{U}(x,y)$ and is given by

$$\underline{U}(x,y) = \underline{U}'(x,y)\,\underline{t}_L(x,y) = \underline{U}'(x,y) \exp\left[\frac{-j\pi}{\lambda F_L}(x^2 + y^2)\right] P(x,y)$$
$$\tag{1-24}$$

where the constant phase delay term has been neglected.

Assume that an input transparency, with amplitude transmittance characteristics $\underline{t}_0(x_0,y_0)$, was placed against the front side of the lens. If this object were uniformly illuminated by plane wave monochromatic light (see Figure 3), then the light distribution immediately behind the lens is given by

$$\begin{aligned}
\underline{U}_0(x_0,y_0) &= \underline{U}'_0(x_0,y_0)\,\underline{t}_L(x_0,y_0) \\
&= \underline{t}_0(x_0,y_0)\,\underline{t}_L(x_0,y_0) \\
&= \underline{t}_0(x_0,y_0) \exp\left[\frac{-j\pi}{\lambda F_L}(x_0^2 + y_0^2)\right] P(x_0,y_0) \tag{1-25}
\end{aligned}$$

---

[1] Rays that make small angles with the optical axis and travel close to the optical axis.

[2] This transmittance function is derived in Goodman [9].
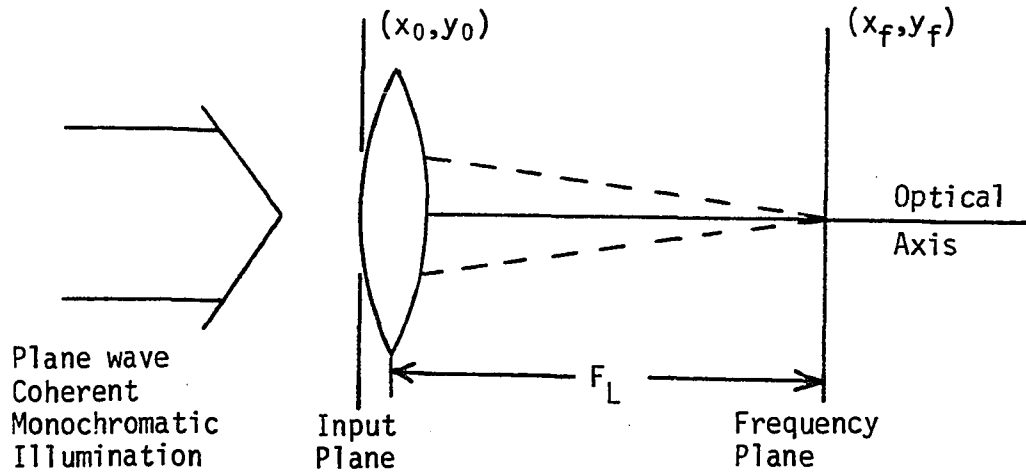
Figure 3. Optical configuration employing a thin converging lens to ob-
serve the Fraunhofer diffraction pattern of an input trans-
mittance function.

where the illuminating light is assumed to be of unit amplitude. If the

maximum dimensions of the input transmittance function, $\underline{t}_0(x_0,y_0)$, are

smaller than the lens aperture dimensions, then the aperture function

$P(x_0,y_0)$ can be neglected. Using this result and applying Equation 1-16,

the field distribution in the frequency plane is

$$\underline{U}_f(x_f,y_f) = \underline{K} \exp\left[\frac{j\pi}{\lambda F_L} (x_f^2 + y_f^2)\right] F\left\{\underline{t}_0(x_0,y_0)\right\}$$

$$f_x = x_f/\lambda F_L \ , \quad f_y = y_f/\lambda F_L \tag{1-26}$$

where the frequency plane is now located one focal length, F_L, behind the

lens.

A summary of other optical configurations is shown in Figure 4.

Note, the optical system given in Figure 4a is the same as that given in

Figure 3 when $d = 0$. Also, when $d = F_L$, the quadratic phase term pre-

ceding the transformation is unity and field distributions are then

Figure 4. Optical configurations employing a thin converging lens of focal length F_L to observe the Fraunhofer diffraction pattern of an input transmittance function $\underline{t}_0(x_0,y_0)$. In each case the illumination is coherent monochromatic light of normalized amplitude.

(a) The distribution in the frequency plane for this configuration is given by

$$\underline{U}_f(x_f,y_f) = \underline{K}' \exp\left[\frac{j\pi}{\lambda F_L}\left(1 - \frac{d}{F_L}\right)(x_f^2 + y_f^2)\right] F\left\{\underline{t}_0(x_0,y_0)\right\}$$

$$f_x = x_f/\lambda F_L \quad , \quad f_y = y_f/\lambda F_L$$

(b) The distribution in the frequency plane for this configuration is given by

$$\underline{U}_f(x_f,y_f) = \underline{K} \exp\left[\frac{j\pi}{\lambda b}(x_f^2 + y_f^2)\right] F\left\{\underline{t}_0(x_0,y_0)\right\}$$

$$f_x = x_f/\lambda b \quad , \quad f_y = y_f/\lambda b$$

(c) The distribution in the frequency plane for this configuration is given by

$$\underline{U}_f(x_f,y_f) = \underline{K}'' \exp\left[\frac{j\pi}{\lambda b}\left(1 - \frac{ad}{bc}\right)(x_f^2 + y_f^2)\right] F\left\{\underline{t}_0(x_0,y_0)\right\}$$

$$f_x = (a/\lambda bd)x_f \quad , \quad f_y = (a/\lambda bd)y_f$$

(a)

(b)

$$\frac{1}{a} + \frac{1}{b} = \frac{1}{F_L}$$
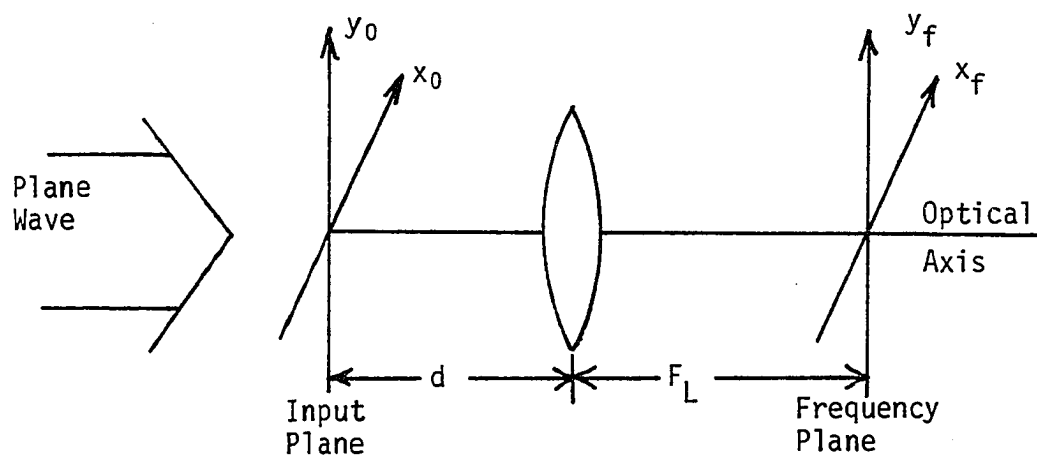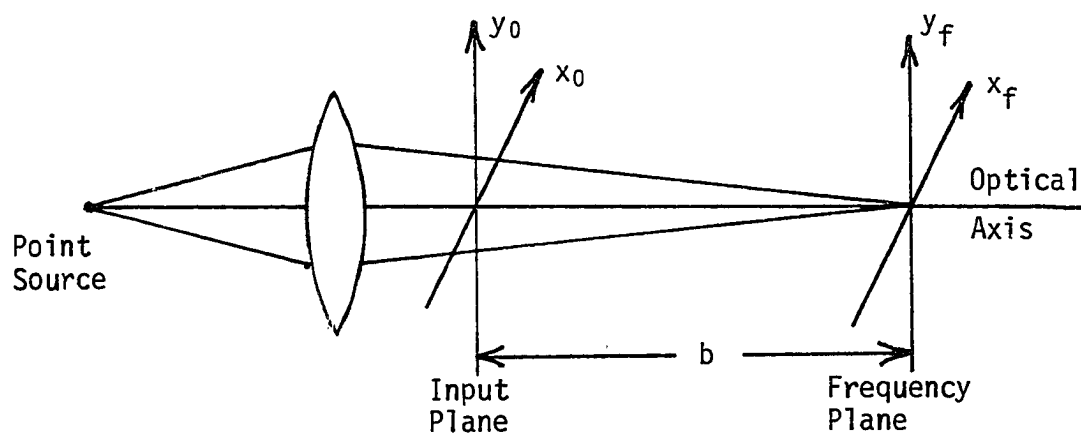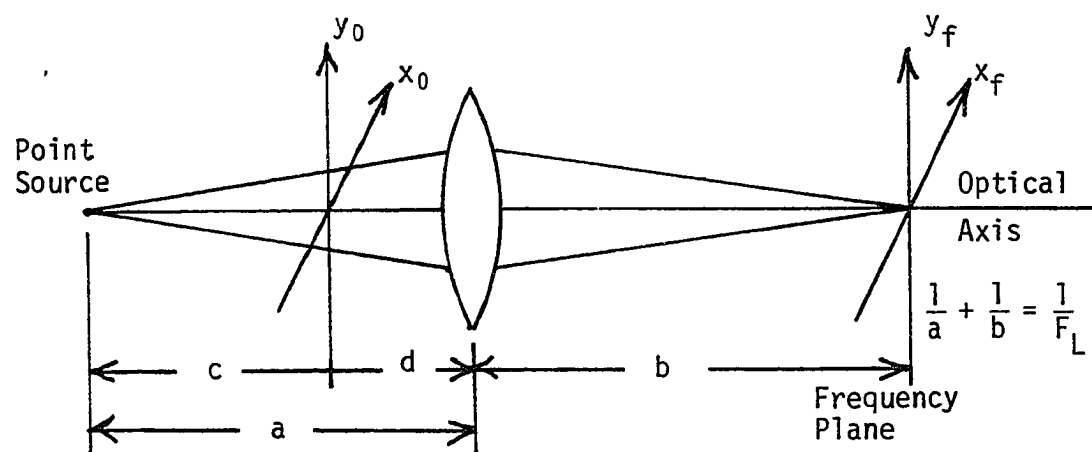
(c)

related by a direct Fourier transform operation. The optical configurations of Figures 4b and 4c, taken from Lee and Gossen [35], have an added advantage that the size of the diffraction pattern in the frequency plane can be varied by changing the location of the input plane.

Before proceeding to a development of a complete optical processing system, two examples of Fraunhofer diffraction will be given. Consider first the rectangular aperture shown in Figure 5a. The amplitude transmittance characteristic for this aperture is given by[1]

$$t_0(x_0, y_0) = \text{rect}(x_0/L_x) \, \text{rect}(y_0/L_y) \qquad (1\text{-}27)$$

where L_x and L_y are, respectively, the lengths of the aperture in the x_0 and y_0 direction. If this aperture is placed in the optical system shown in Figure 2, then the complex light amplitude of the resultant diffraction pattern can be determined from Equation 1-21. That is

$$\underline{U}_f(x_f, y_f) = \underline{K} \exp\left[\frac{j\pi}{\lambda b}(x_f^2 + y_f^2)\right] F\left\{t_0(x_0, y_0)\right\}$$

$$= \underline{K} \exp\left[\frac{j\pi}{\lambda b}(x_f^2 + y_f^2)\right] L_x L_y \, \text{sinc}(L_x f_x) \, \text{sinc}(L_y f_y) \qquad (1\text{-}28)$$

where $f_x = x_f/\lambda b$, $f_y = y_f/\lambda b$, and the function sinc $(L_x f_x)$ is defined as being $\sin(\pi L_x f_x)/\pi L_x f_x$. This function has a value of unity at $f_x = 0$ and is zero for all $f_x = n/L_x$ where n is any nonzero positive or negative integer. A similar description exists for the function $\text{sinc}(L_y f_y)$.

The intensity distribution in the frequency plane is given by

---

[1]The function rect(x/a) is a rectangular function defined as having a value of unity over the range $-a/2 \le x \le a/2$ and zero elsewhere.
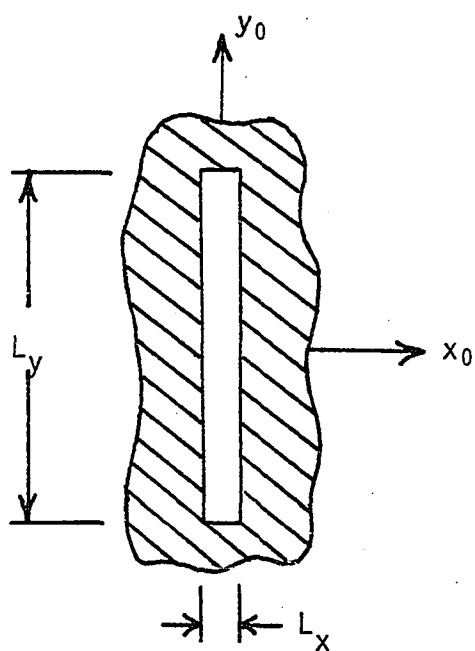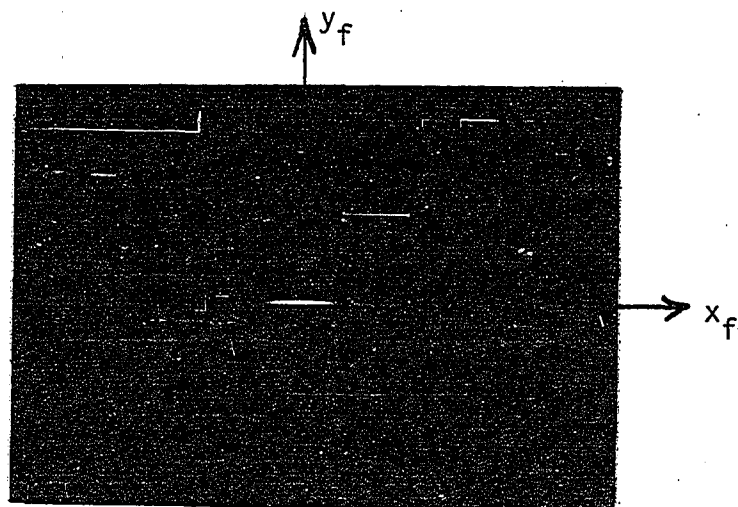
Figure 5a. Rectangular aperture of lengths L_x and L_y.

Figure 5b. Fraunhofer diffraction pattern of a rectangular aperture with $L_y = 15 \ L_x$.

$$I(x_f,y_f) = \underline{U}_f(x_f,y_f)\underline{U}_f^*(x_f,y_f)$$

$$= \left(\frac{L_x L_y}{\lambda b}\right)^2 \text{sinc}^2(L_x f_x) \, \text{sinc}^2(L_y f_y) \qquad (1\text{-}29)$$

Observation of this intensity distribution reveals a zero-order (undiffracted) wave located at a point on the optical axis. Higher orders of diffraction are located symmetrically about the optical axis at distances related to the spatial frequency components, f_x and f_y, of the aperture. The distance between successive peaks in the diffraction pattern along the x_f or the y_f-axis is inversely proportional to the length L_x or L_y, respectively. By increasing the aperture length in one dimension, the size of the diffraction pattern along the corresponding dimension will be reduced. Conversely, if this length is decreased, then the higher orders of diffraction will occur at distances further from the optical axis. An analogous situation exists for the spectrum of a rectangular time pulse. If the pulse length increases, the spectrum is confined to frequency components closer to zero, and as the pulse length decreases, a broad spectrum is produced.

A photograph of the diffraction pattern produced by a rectangular aperture with $L_y = 15L_x$ is shown in Figure 5b. By using a photocell scanner to measure the light intensity as a function of position along either the x_f or y_f-axis, it would be possible to record a relative energy density spectrum for the corresponding one-dimensional rectangular function. This is the basis of optical data processing for frequency information.

As a second example of Fraunhofer diffraction, consider the circular aperture of diameter D shown in Figure 6a. If this aperture were placed
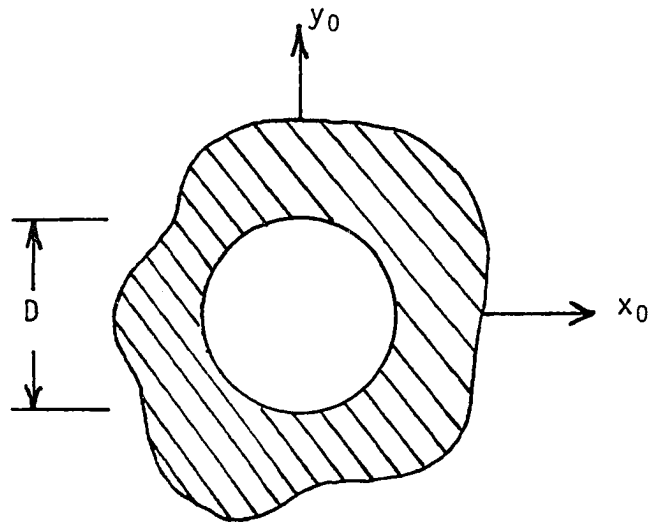
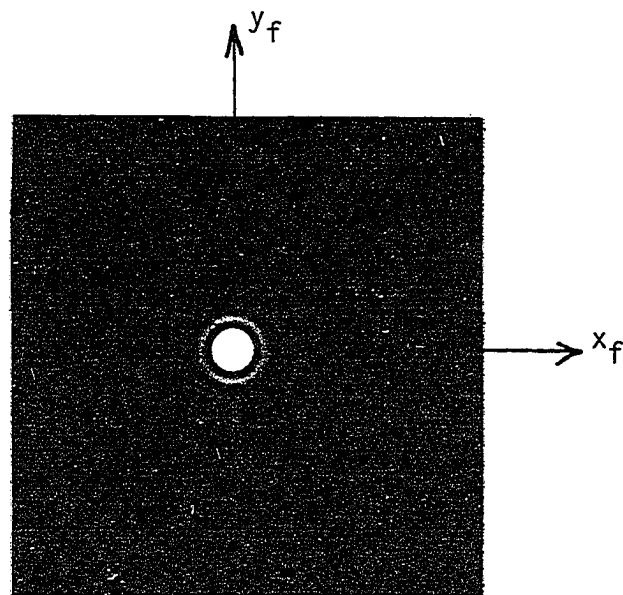Figure 6a. Circular aperture of diameter D.

Figure 6b. Fraunhofer diffraction pattern of a circular aperture.

in the optical system of Figure 2, then the resulting diffraction pattern would appear as shown in Figure 6b. This intensity distribution is called an Airy pattern, and is important in many optical processing systems. The radius of the central maximum is $1.22\lambda b/D$, and a good approximation to a point source can be made by placing in the frequency plane a small circular aperture that allows only this central portion to pass.

Optical Processing System

The two primary applications of coherent optical computing are to process an input object transparency for frequency information, and/or to reconstruct an image of a spatially filtered object transparency. The first of these applications was outlined in the previous section. In this section, a general optical configuration for performing both of these processing operations will be considered.

The following development will involve the optical system illustrated in Figure 7. In this configuration, it is assumed that there is a light
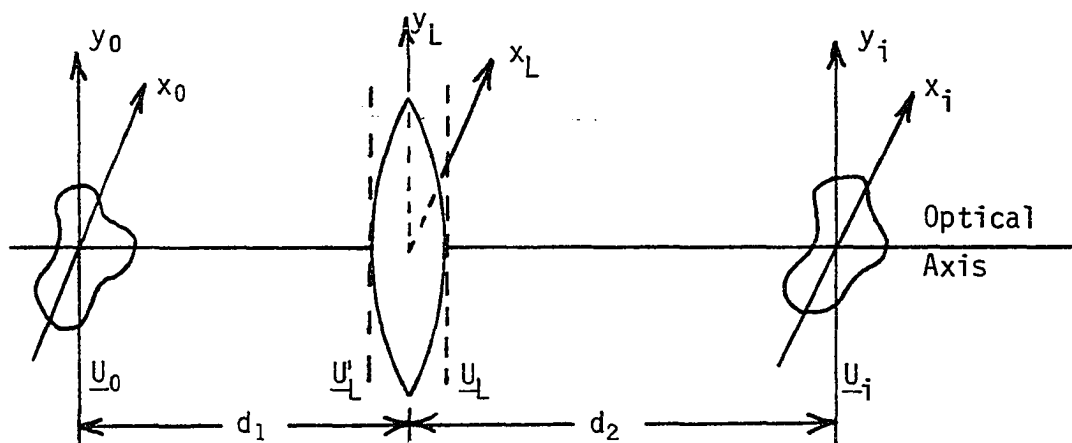
Figure 7. A general optical configuration.

distribution $\underline{U}_0$ in the x_0-y_0 plane at a distance d_1 in front of a thin

converging lens, and that there is a resulting light distribution $\underline{U}_i$ in

the x_i-y_i plane located a distance d_2 behind the lens. For convenience,

the lens aperture dimensions are assumed to be large enough that all the

information contained in $\underline{U}_0$ is transferred through the lens into $\underline{U}_i$. The

objectives of the following discussion are to first relate these two

distributions under the thin lens imaging condition

$$\frac{1}{d_1} + \frac{1}{d_2} = \frac{1}{F_L} \tag{1-30}$$

and then to consider a special case for $\underline{U}_0$ such that spatial filtering can

be accomplished.

From Figure 7, $\underline{U}'_L$ is the light distribution immediately in front of

the lens. By applying Equation 1-16, this distribution is

$$\underline{U}'_L(x_L,y_L) = \frac{\exp[j2\pi d_1/\lambda]}{j\lambda d_1} \exp\left[\frac{j\pi}{\lambda d_1}(x_L^2 + y_L^2)\right]$$

$$F\left\{\underline{U}_0(x_0,y_0) \exp\left[\frac{j\pi}{\lambda d_1}(x_0^2 + y_0^2)\right]\right\}$$

$$f_x = x_L/\lambda d_1 \quad , \quad f_y = y_L/\lambda d_1 \tag{1-31}$$

If $\underline{U}_L$ is the light distribution immediately behind the lens, then from

Equation 1-24 this distribution is

$$\underline{U}_L(x_L,y_L) = \underline{U}'_L(x_L,y_L) \exp\left[\frac{-j\pi}{\lambda F_L}(x_L^2 + y_L^2)\right] \tag{1-32}$$

Now, applying Equation 1-16 to relate $\underline{U}_i$ to $\underline{U}_L$, the result is

$$\underline{U}_i(x_i,y_i) = \frac{\exp[j2\pi d_2/\lambda]}{j\lambda d_2} \exp\left[\frac{j\pi}{\lambda d_2}(x_i^2 + y_i^2)\right]$$

$$F\left\{\underline{U}_L(x_L,y_L) \exp\left[\frac{j\pi}{\lambda d_2}(x_L^2 + y_L^2)\right]\right\}$$

$$f_x = x_i/\lambda d_2 \ , \quad f_y = y_i/\lambda d_2 \tag{1-33}$$

Combining Equations 1-31, 1-32, and 1-33 will result in

$$\underline{U}_i(x_i,y_i) = \frac{\exp\left[\frac{j2\pi}{\lambda}(d_1 + d_2)\right]}{-\lambda^2 d_1 d_2} \ \exp\left[\frac{j\pi}{\lambda d_2}(x_i^2 + y_i^2)\right]$$

$$F\left\{\exp\left[\frac{j\pi}{\lambda}(x_L^2 + y_L^2)(\frac{1}{d_1} + \frac{1}{d_2} - \frac{1}{F_L})\right] F\left\{\underline{U}_0(x_0,y_0)\right.\right.$$

$$\left.\left.\exp\left[\frac{j\pi}{\lambda d_1}(x_0^2 + y_0^2)\right]\right\}\right\} \tag{1-34}$$

where the inner Fourier transformation is evaluated at spatial frequencies

$f_x = x_L/\lambda d_1$, $f_y = y_L/\lambda d_1$, and the outer transformation is evaluated at

$f_x = x_i/\lambda d_2$, $f_y = y_i/\lambda d_2$. By applying the thin lens imaging condition

(Equation 1-30), the distribution $\underline{U}_i$ is given by

$$\underline{U}_i(x_i,y_i) = \frac{\exp\left[\frac{j2\pi}{\lambda}(d_1 + d_2)\right]}{-\lambda^2 d_1 d_2} \ \exp\left[\frac{j\pi}{\lambda d_2}(x_i^2 + y_i^2)\right]$$

$$F\left\{F\left\{\underline{U}_0(x_0,y_0) \ \exp\left[\frac{j\pi}{\lambda d_1}(x_0^2 + y_0^2)\right]\right\}\right\} \tag{1-35}$$

Replacing the Fourier transform symbols with their integral representa-

tions and then changing the order of integration, it can be shown that the

distribution $\underline{U}_i(x_i,y_i)$ will reduce to

$$\underline{U}_i(x_i,y_i) = -\frac{d_1}{d_2} \exp\left[\frac{j2\pi}{\lambda}(d_1 + d_2)\right]$$

$$\exp\left[\frac{j\pi}{\lambda d_2}(1 + \frac{d_1}{d_2})(x_i^2 + y_i^2)\right] \underline{U}_0\left(-\frac{d_1}{d_2}x_i, -\frac{d_1}{d_2}y_i\right) \tag{1-36}$$

As expected, this result indicates that the light distribution in the

x_i-y_i plane is an inverted image of the light distribution in the x_0-y_0

plane magnified by a factor d_2/d_1. Note, there is a quadratic phase de-

pendence in this distribution that is not present in the $\underline{U}_0$ distribution,

but this is of little consequence since the image is recorded as an intensity distribution, $\underline{U}_i \cdot \underline{U}_i^*$.

Assume now that the distribution $\underline{U}_0$ is the result of placing in the x_0-y_0 plane an object transparency with amplitude transmittance $\underline{t}_0$ illuminated with a beam converging to a point a distance behind this plane (Figure 8). Thus, $\underline{U}_0(x_0,y_0)$ is given by

$$\underline{U}_0(x_0,y_0) = \exp\left[\frac{-j\pi}{\lambda b}(x_0{}^2 + y_0{}^2)\right]\underline{t}_0(x_0,y_0) \qquad (1\text{-}37)$$
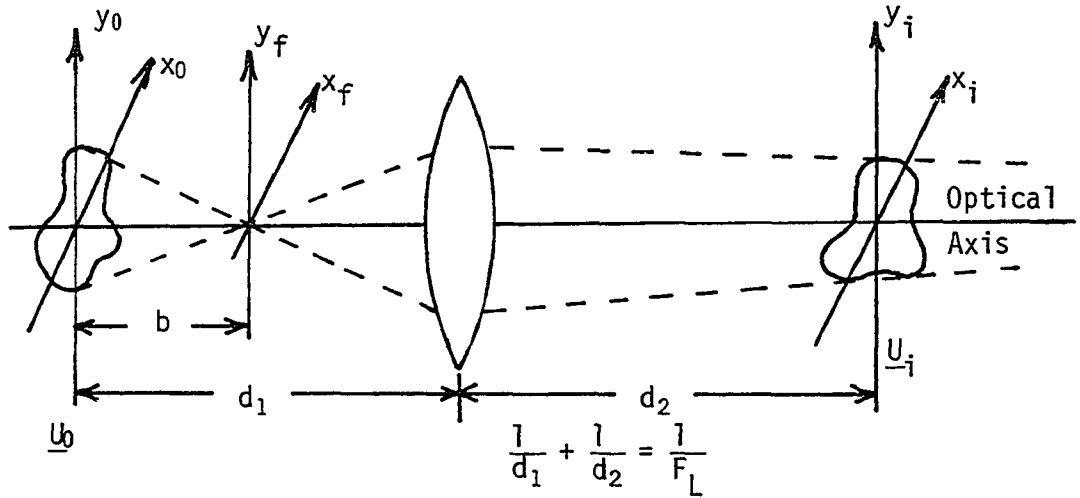
Figure 8.   Optical configuration in which an object transparency, $\underline{t}_0(x_0,y_0)$, is illuminated with a converging beam.

and from Equation 1-36, the distribution in the x_i-y_i plane (image plane) is

$$\underline{U}_i(x_i,y_i) = -\frac{d_1}{d_2} \exp\left[\frac{j2\pi}{\lambda}(d_1 + d_2)\right]$$

$$\exp\left[\frac{j\pi}{\lambda d_2}(1 + \frac{d_1}{d_2} - \frac{d_1{}^2}{bd_2})(x_i{}^2 + y_i{}^2)\right]\underline{t}_0\left(-\frac{d_1}{d_2}x_i, -\frac{d_1}{d_2}y_i\right)$$

$$(1\text{-}38)$$

This distribution is an inverted magnified version of the input amplitude transmittance function. Unless $d_1-b = F_L$ there will be a quadratic phase dependence in the amplitude distribution. However, this will not affect the intensity distribution.

Taking this analysis one step further, consider now the situation where the distribution in the x_f-y_f plane (frequency plane) is altered by some operation. This distribution is, from Equation 1-21, given by

$$\underline{U}_f(x_f,y_f) = \underline{K} \exp\left[\frac{j\pi}{\lambda b}(x_f^2 + y_f^2)\right] F\left\{\underline{t}_0(x_0,y_0)\right\}$$

$$f_x = x_f/\lambda b \quad, \quad f_y = y_f/\lambda b \tag{1-39}$$

By placing a spatial filter[1] with amplitude transmittance characteristics $\underline{H}\left(\frac{x_f}{\lambda b}, \frac{y_f}{\lambda b}\right)$ in the frequency plane, the light distribution immediately behind the spatial filter is

$$\underline{U}_f(x_f,y_f) = \underline{K} \exp\left[\frac{j\pi}{\lambda b}(x_f^2 + y_f^2)\right] \underline{H}\left(\frac{x_f}{\lambda b}, \frac{y_f}{\lambda b}\right) F\left\{\underline{t}_0(x_0,y_0)\right\}$$

$$f_x = x_f/\lambda b \quad, \quad f_y = y_f/\lambda b \tag{1-40}$$

This result is equivalent to having an input object transparency with amplitude transmittance characteristics $\underline{t}_0'(x_0,y_0)$, where

$$F\left\{\underline{t}_0'(x_0,y_0)\right\} = \underline{H}(f_x,f_y) F\left\{\underline{t}_0(x_0,y_0)\right\}$$

$$f_x = x_f/\lambda b \quad, \quad f_y/\lambda b \tag{1-41}$$

It is recognized that the transmittance function $\underline{t}_0'$ is merely the spatially filtered version of $\underline{t}_0$. Thus, the distribution in the image plane

---

[1]A spatial filter is an optical transparency or an aperture with amplitude transmittance characteristics that alter in some prescribed manner the light passing beyond the frequency plane.

is

$$\underline{U}_i(x_i,y_i) = -\frac{d_1}{d_2} \exp\left[\frac{j2\pi}{\lambda}(d_1 + d_2)\right]$$

$$\exp\left[\frac{j\pi}{\lambda d_2}(1 + \frac{d_1}{d_2} - \frac{d_1^2}{bd_2})(x_i^2 + y_i^2)\right] \underline{t}_0'\left(-\frac{d_1}{d_2}x_i, -\frac{d_1}{d_2}y_i\right) \quad (1-42)$$

This distribution represents the spatially filtered version of the object

transparency $\underline{t}_0$, magnified by a factor d_2/d_1 and inverted. Although there

is a quadratic phase error, the intensity in the image plane will be that

of the magnified, inverted, and filtered version of $\underline{t}_0 \cdot \underline{t}_0^*$.

An optical system for performing the operations of optical frequency

processing, spatial filtering, and image reconstruction is shown in Figure

9. Note, from the thin lens imaging condition

$$\frac{1}{d_1-b} + \frac{1}{q_1} = \frac{1}{F_L} \quad (1-43)$$

the distribution in the x_2-y_2 plane is the inverted and magnified version

of the frequency plane distribution. Thus, using this optical configura-

tion it is possible to frequency process a transparency, image the spa-

tially filtered version of this transparency, and observe the frequency

characteristics of the filtered transparency.

Throughout the analysis just completed and also that of the previous

section, many approximations and assumptions have been made that inherent-

ly affect the accuracy of optical processing. The paraxial approximation

affects both the amplitude and frequency accuracy of the Fourier transform

relationship in the frequency plane. Also, by considering a realistic

lens with finite aperture dimensions, some information may be lost in the

imaging operation. Under practical operating conditions, however, these

approximations and assumptions are very accurate and valid. As an example,

$\underline{U}_0(x_0,y_0)$ $\underline{U}_f(x_f,y_f)$ $\underline{U}_i(x_i,y_i)$ $\underline{U}_2(x_2,y_2)$

Point
Source

Frequency
Plane

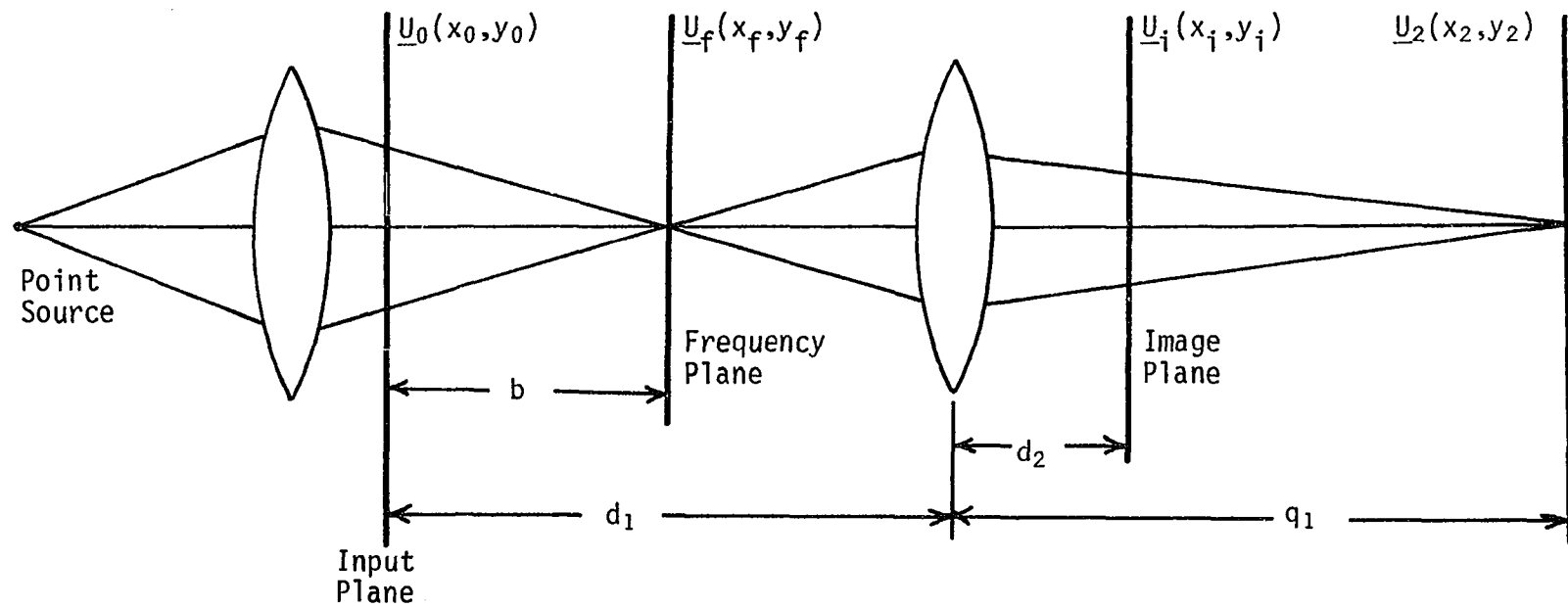Image
Plane

b

d_2

d_1

q_1

Input
Plane

40

Figure 9.   Optical system used for frequency processing, filtering, and imaging an input
object transparency.

consider a one-dimensional transmittance function placed in the optical

system of Figure 9. If

$$\lambda = 6 \times 10^{-5} \text{ cm}$$

$$b = 50 \text{ cm}$$

$$x_{0 \text{ max}} = 0.5 \text{ cm}$$

$$x_{f \text{ max}} = 1.5 \text{ cm (thus } f_{x \text{ max}} = 50 \text{ cycles/mm)}$$

$$d_1 = 75 \text{ cm}$$

then the error in assuming the paraxial approximation is much less than

1%, and minimum lens diameter required to image all frequency components

below 50 cycles/mm is 5 cm.

Data Input Format

The discussions in the previous sections have been concerned with

optically processing input amplitude transmittance functions of the form

$\underline{t}_0(x_0, y_0)$. It has been shown that the light amplitude distribution in the

frequency plane of various optical configurations is related to the

Fourier transform of these transmittance functions. However, very little

physical significance has been given to the information that is represent-

ed by these transmittance functions. The purpose of this section is to

consider various recording formats that can be used in representing a real

one-dimensional function of time as a spatial amplitude transmittance

function.

Black and white photographic film is the medium used most often in

optical processing to convert signals from the time domain into the spa-

tial domain. This medium has the advantages of being low in cost and easy

to use, as well as having good spatial frequency characteristics. How-

ever, it has the disadvantage of preventing real time signal analysis since an initial chemical processing step is required.

In the analysis to follow, a real one-dimensional time function, g(t), is assumed to be represented in the spatial domain as g(x). The Fourier transform of this function over the spatial limits $-L_x/2 \leq x \leq L_x/2$ is given by

$$\underline{G}(f_x) = \int_{-\infty}^{\infty} g(x) \, rect(x/L_x) \, exp\left[-j2\pi f_x x\right] dx$$

$$= \int_{-L_x/2}^{L_x/2} g(x) \, exp\left[-j2\pi f_x x\right] dx \qquad (1-44)$$

where the length of the signal, L_x, in the spatial domain is directly related to a time period, T, in the time domain. It will be shown that a number of recording formats will allow optical computation of this Fourier transformation.

Area modulation format

Area modulation recording represents one way to permit relaxation of the exposure and processing requirements of photographic film. In area modulation, the transmittance function has two values; essentially unity and essentially zero. The film exposure and processing need only be such as to satisfy these binary requirements, and thus detailed characteristics of photographic film will not be considered at this time.

An area modulated transparency can be made by moving photographic film at a constant speed past a narrow illuminating light source. If the vertical dimensions of the light source vary in accordance with the

applied signal plus a constant bias, then the positive processed film strip will represent an area modulated transparency. Figure 10 illustrates a section of an area modulated transparency. The amplitude transmittance of this transparency can be written as

$$t_0(x_0,y_0) = \text{rect}(x_0/L_x) \ \text{rect}[y_0/2(B+g(x_0))] \tag{1-45}$$

where L_x is the signal length in the x direction, and B is constant bias term added to $g(x_0)$ to ensure that this sum is positive even for negative values of $g(x_0)$. The two-dimensional Fourier transform of this transmittance function is

$$\underline{T}(f_x,f_y) = \int\int\limits_{-\infty}^{\infty} t_0(x_0,y_0) \ \exp[-j2\pi(f_x x_0 + f_y y_0)] \ dx_0 dy_0$$

$$= \int\int\limits_{-\infty}^{\infty} \text{rect}(x_0/L_x) \ \text{rect}[y_0/2(B+g(x_0))]$$

$$\exp[-j2\pi(f_x x_0 + f_y y_0)] \ dx_0 dy_0 \tag{1-46}$$
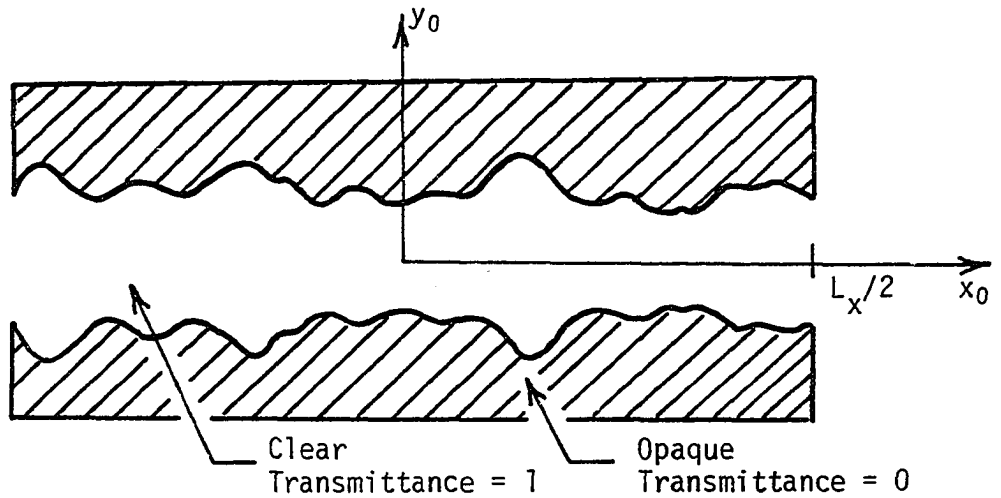
Figure 10. Illustration of an area modulated transparency.

Integrating first with respect to y_0 reduces this equation to

$$\underline{I}(f_x, f_y) = 2 \int_{-\infty}^{\infty} [B+g(x_0)] \, \text{rect}(x_0/L_x) \, \text{sinc}[f_y(B+g(x_0))]$$

$$\exp[-j\pi f_x x_0] \, dx_0 \qquad\qquad (1\text{-}47)$$

In general, $\underline{I}(f_x, f_y)$ is very involved and for $f_y \neq 0$ yields many frequency components not in the original signal. However, for $f_y = 0$ it reduces to

$$\underline{I}(f_x, 0) = 2 \int_{-\infty}^{\infty} [B+g(x_0)] \, \text{rect}(x_0/L_x) \, \exp[-j2\pi f_x x_0] \, dx_0$$

$$= 2BL_x \, \text{sinc}(f_x L_x)$$

$$+2 \int_{-\infty}^{\infty} g(x_0) \, \text{rect}(x_0/L_x) \, \exp[-j2\pi f_x x_0] \, dx_0 \qquad\qquad (1\text{-}48)$$

For the special case of $f_y = 0$, Equation 1-48 is essentially the same as Equation 1-44 except for an error produced at $f_x = 0$. Thus, if an optical sensor is placed or moved along the $f_y = 0$ axis ($y_f = 0$) of an optically produced transform, a relative energy density spectrum of the area modulating signal can be detected.

Single line format

A common method for observing a time varying signal is to record the signal on a strip chart recorder. Some information about the signal can be extracted by visual observation of this type of signal record. However, by photographing the signal record, it is possible to optically compute approximate spectral information for a section of the signal record.

An optical transparency produced by photographing and negative processing a strip chart record has an amplitude transmittance function that can be approximated by

$$t_0(x_0,y_0) = \begin{cases} 1 & \text{for } |x_0| \leq L_x/2 \text{ and } g(x_0)-\varepsilon/2 \leq y_0 \leq g(x_0)+\varepsilon/2 \\ 0 & \text{elsewhere} \end{cases} \tag{1-49}$$

where ε is the vertical line thickness which is assumed to be constant, and L_x is the length of the signal record. The two-dimensional Fourier transform of this function over the above limits is

$$\underline{T}(f_x,f_y) = \int_{-L_x/2}^{L_x/2} \int_{g(x_0)-\varepsilon/2}^{g(x_0)+\varepsilon/2} \exp[-j2\pi(f_x x_0 + f_y y_0)] \, dy_0 dx_0$$

$$= \varepsilon \, \text{sinc}(f_y\varepsilon) \int_{-L_x/2}^{L_x/2} \exp[-j2\pi f_y g(x_0)] \exp[-j2\pi f_x x_0] \, dx_0 \tag{1-50}$$

This transform is also very involved and contains many frequency components not in the original signal. However, if f_y is small but non-zero, the following approximations can be made:

$$\varepsilon \, \text{sinc}(f_y\varepsilon) \doteq \varepsilon$$

and

$$\exp[-j2\pi f_y g(x_0)] = \cos(2\pi f_y g(x_0)) - j \sin(2\pi f_y g(x_0))$$

$$\doteq 1 - j2\pi f_y g(x_0) \tag{1-51}$$

Within the validity of these approximations, $\underline{T}(f_x,f_y)$ can be written as

$$\underline{T}(f_x,f_y) \doteq \varepsilon L_x \, \text{sinc}(L_x f_x)$$

$$-j2\pi\varepsilon f_y \int_{-L_x/2}^{L_x/2} g(x_0) \exp[-j2\pi f_x x_0] \, dx_0 \tag{1-52}$$

Thus, if f_y is small but nonzero, then except for an error at $f_x = 0$, the second term provides an approximation to the desired transformation. However, this result was arrived at under the assumption that the vertical line thickness is constant. If ε is not constant, which is often the case, then Equation 1-52 is invalid, and the optically computed spectrum will contain frequency components not in the original signal.

Density modulation format

Another method for recording a one-dimensional signal on photographic film is to use this signal in some manner to density modulate the film. This technique utilizes the density exposure characteristics of photographic film, and thus some fundamental properties of photographic film will now be considered.

Unexposed film consists of a light sensitive emulsion on a base support consisting typically of acetate. The photosensitive material is a mixture of very small silver halide crystals suspended in gelatin. The size of the crystals is approximately one micron, and as a general rule the larger the silver halide crystals the greater a film's sensitivity to light. It is an empirical observation that regardless of size, a silver halide crystal requires a certain number of absorbed photons to excite it. Thus, films with large crystals require fewer photons to achieve a specified density level than films containing smaller crystals. However, a film with large crystals will lack the capability of recording fine details. A film containing smaller crystals has greater resolution capabilities, but it is less sensitive to light and thus requires a longer exposure time to absorb the needed number of photons.

When the photosensitive emulsion is exposed to light, the silver halide crystals absorb photons and undergo a complex physical change. This physical change is not usually visible until the film is subject to the action of a developer. The developer chemically changes the exposed silver halide crystals into metalic silver grains. The unexposed crystals are not affected by the action of the developer and can be removed by a chemical fixing solution. Since the silver grains are nearly opaque and the film base is essentially clear the opacity of the developed film will depend upon the density of silver grains in each region of the film. The intensity transmittance of the developed film transparency is defined as

$$\tau_I(x,y) = I_T/I_0 \tag{1-54}$$

where I_T is the light intensity transmitted at (x,y) and I_0 the incident light intensity at (x,y). The film density is defined as

$$D = \log \frac{I_0}{I_T} = \log\left(\frac{1}{\tau_I}\right) \tag{1-54}$$

A photographic emulsion that is exposed to a constant light intensity will have a developed image whose density (within limits) will increase with increasing exposure time. The relationship between density and exposure is represented by a graph called the characteristic curve. Figure 11 illustrates a typical characteristic curve for a photographic film. The graph is obtained by plotting the density versus the common logarithm of exposure. Film exposure is defined as

$$E = I_s t \tag{1-55}$$

where I_s is incident intensity of the light exposing the film, and t is the exposure time.
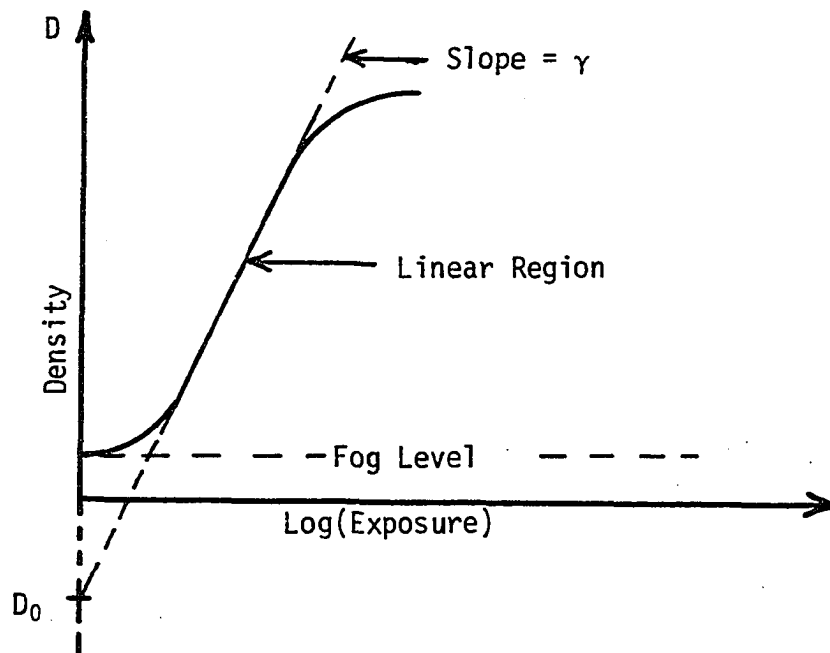
Figure 11. Characteristic curve for a photographic film.

When the exposure is below a certain level, the density is independent of the exposure and is equal to a minimum value called the fog level. As the exposure is increased from this point, the density increases nonlinearly toward a region where it then increases linearly with the logarithm of exposure. The slope of the characteristic curve in this linear region is referred to in this dissertation as the film gamma (γ). It is in this linear region that photographic film is used for most conventional applications. Beyond the linear region, the density will increase only slightly with increasing exposure.

The shape of the characteristic for a photographic film will depend upon the nature of the emulsion and the method by which it was developed. A high contrast film is characterized by a large gamma, and a low contrast

film has a low gamma. The value of gamma for each of these general film types is in turn affected by the developing process. The type of developing solution used, the temperature of this developer, and the developing time all have an effect on the value of gamma. In general, gamma will increase (within limits) as the time of developing or the developer temperature is increased. Thus, to completely describe the properties of a particular film, a family of characteristic curves is required.

Assuming that the film is used in the linear region of the characteristic curve, the density for a given developer, developing time and temperature is given by

$$D = \gamma \log E + D_0 = \gamma \log(I_s t) + D_0 \tag{1-56}$$

where D_0 is a constant determined by the straight line approximation of the linear region. The incident intensity during exposure of the film can be related to the intensity transmittance after processing the film by equating Equations 1-54 and 1-56. This result is

$$\log\left(\frac{1}{\tau_I} \right) = \gamma \log(I_s t) + D_0 \tag{1-57}$$

and solving for τ_I will give

$$\tau_I = 10^{-D_0}(I_s t)^{-\gamma} \tag{1-58}$$

which can be written as

$$\tau_I = K_1 (I_s)^{-\gamma} \tag{1-59}$$

where K_1 is a constant.

Assuming that the film is of constant thickness, the amplitude and intensity transmittance are related by

$$t(x,y) = [\tau_I(x,y)]^{\frac{1}{2}}$$

$$= K_2(I_s)^{-\gamma/2} \tag{1-60}$$

Also assume that the incident light intensity is produced by a light source whose intensity is related to the input plus a constant bias by the following equation

$$I_s = K_3/[B+g(t)]^c \tag{1-61}$$

where K_3, c, and B are constants. If the light source is contained behind a narrow slit aperture and the film is moved at a constant speed past the aperture, then the amplitude transmittance of the developed film is

$$t(x,y) = K_4[B+g(x)]^{\gamma c/2} \text{rect}(y/L_y) \tag{1-62}$$

where K_4 is a constant and L_y is the width of the exposed film. Under the conditions that $\gamma c = 2$, a section of the film will have an amplitude transmittance given by

$$t_0(x_0,y_0) = K_4[B+g(x_0)] \text{rect}(x_0/L_x) \text{rect}(y_0/L_y) \tag{1-63}$$

The two-dimensional Fourier transform of Equation 1-63 will reduce to

$$\underline{T}(f_x,f_y) = K_4 B L_x L_y \text{sinc}(f_x L_x) \text{sinc}(f_y L_y)$$

$$+ K_4 L_y \text{sinc}(f_y L_y) \int_{-\infty}^{\infty} g(x_0) \text{rect}(x_0/L_x)$$

$$\exp[-j2\pi f_x x_0] dx_0 \tag{1-64}$$

and under the condition that $f_y = 0$, this transform further reduces to

$$\underline{T}(f_x,0) = K_4 B L_y \text{sinc}(f_x L_x)$$

$$+ K_4 L_y \int_{-\infty}^{\infty} g(x_0) \text{rect}(x_0/L_x) \exp[-j2\pi f_x x_0] dx_0 \tag{1-65}$$

Equation 1-65 is essentially the same as Equation 1-44 except for an error produced at $f_x = 0$. Note also, if L_y is large, then Equation 1-64 is approximately[1]

$$\underline{T}(f_x, f_y) \simeq K_4 B L_x \delta(f_y) \, \text{sinc}(f_x L_x)$$

$$+ K_4 \delta(f_y) \int_{-\infty}^{\infty} g(x_0) \, \text{rect}(x_0/L_x)$$

$$\exp[-j2\pi f_x x_0] \, dx_0 \tag{1-66}$$

and the result will exist only along the $f_y = 0$ axis. Thus a one-dimensional Fourier transform can be produced.

It was assumed in the above development that the film thickness was constant. This assumption allowed the amplitude and intensity transmittance to be related by Equation 1-60. If the thickness is not constant, the optical path through the film is not constant and phase shifts will be introduced into the optical signal. Thus the complete description of the amplitude transmittance is

$$\underline{t}(x, y) = [\tau_I(x, y)]^{\frac{1}{2}} \exp[j\phi(x, y)] \tag{1-67}$$

---

[1]The function $\delta(f_y)$ is an impulse function defined as

$$\delta(f_y) = \begin{cases} \infty & \text{for } f_y = 0 \\ 0 & \text{otherwise} \end{cases}$$

with the additional property that

$$\int_{-\varepsilon}^{\varepsilon} \delta(f_y) df_y = 1$$

for any $\varepsilon > 0$.

where $\phi(x,y)$ describes the phase shifts introduced by the film thickness variations. These variations originate in three distinct ways. First, there exist random thickness variations in the emulsion and the film base. Second, the emulsion thickness in the developed transparency varies with the density of silver, and finally, portions of the developed transparency may shrink upon drying. These thickness variations will introduce phase shifts into the recorded signal and this may have an adverse effect on the optically computed spectrum results. These undesirable phase shifts can be removed by placing the transparency between optically flat glass plates with an oil of matching index of refraction surrounding the film (Figure 12). The oil fills the voids between the optically flat glass and the film, thus making the transparency appear to be of constant thickness. This device is called a liquid gate.

Although in principle the density modulation format provides an exact method of determining the frequency components of a signal, in practice it has a number of apparent drawbacks. The most important of these involves the critical requirements imposed on the exposure and processing of the film to make the resultant transmittance exactly correspond to the original signal. However, it has a distinct advantage over the other input formats in that a one-dimensional Fourier transform will be produced if L_y (the width of the transparency in the y_0 direction) is large. Under this condition, the light amplitude in the frequency plane will only exist along the f_x-axis (x_f-axis).

Phase modulation

In some cases it is possible to use only phase changes to introduce an input signal into the optical processing system. A transparent medium
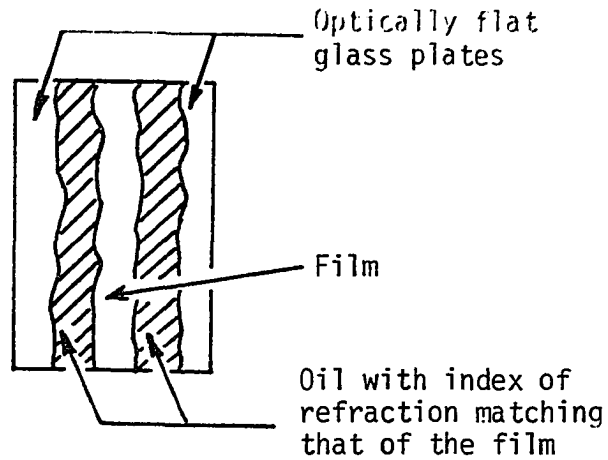
Figure 12. A method of removing the film thickness variations.

whose thickness is varied by thermal techniques in accordance with the desired input signal can be used as the input transparency. Such a transparency would have a transmittance function given by

$$\underline{t}(x_0,y_0) = \exp[jg(x_0)] \; \text{rect}(x_0/L_x) \; \text{rect}(y_0/L_y) \tag{1-68}$$

If the magnitude of $g(x_0)$ were small, this function could be approximated as

$$\underline{t}(x_0,y_0) \simeq [1+jg(x_0)] \; \text{rect}(x_0/L_x) \; \text{rect}(y_0/L_y) \tag{1-69}$$

and the resultant Fourier transform along the $f_y = 0$ axis would be

$$\underline{T}(f_x,0) = L_x L_y \; \text{sinc}(f_x L_x)$$

$$+ jL_y \int_{-\infty}^{\infty} g(x) \; \text{rect}(x_0/L_x) \; \exp[-j2\pi f_x x_0] \; dx_0 \tag{1-70}$$

Other formats using photographic film as the recording medium may also be used to input signals into an optical processing system. These formats involve combinations of area, density, or phase modulation. However, such methods are difficult to produce and control accurately.

EXPERIMENTAL APPARATUS AND PROCEDURES

Optical System

The objectives of the first part of this dissertation research are to demonstrate optical processing of real one-dimensional biological signals for frequency content, and to compare various data input formats. The optical system used in this part of the research is illustrated in Figure 13.

A continuous wave, single transverse mode, helium-neon laser[1] was used as the coherent monochromatic light source. A microscope objective lens[2] was positioned in front of the laser and was used to converge the laser beam. The pinhole aperture[3], located at the beam converging point, was used to spatially filter the converged beam. The undesirable off-axis spatial variations in the laser beam are commonly removed by such a pinhole aperture, and the light diverging from the pinhole is a good approximation to a uniform spherical wave diverging from a point source.

A second circular aperture (6mm diameter) was located between the pinhole and the converging lens. This aperture was used to limit the length of the signal transparency being processed, and also to limit the illuminated lens area. By limiting the illuminated area to the central

---

[1]Two models were used in this research: Model 124B (15 milliwatt light output); and Model 120 (5 milliwatt light output), Spectra Physics, Inc., Mountain View, California.

[2]Two magnifications were used: 40X and 10X.

[3]Two diameter sizes were used: 10 micron and 25 micron, Edmund Scientific Company, Barrington, New Jersey.
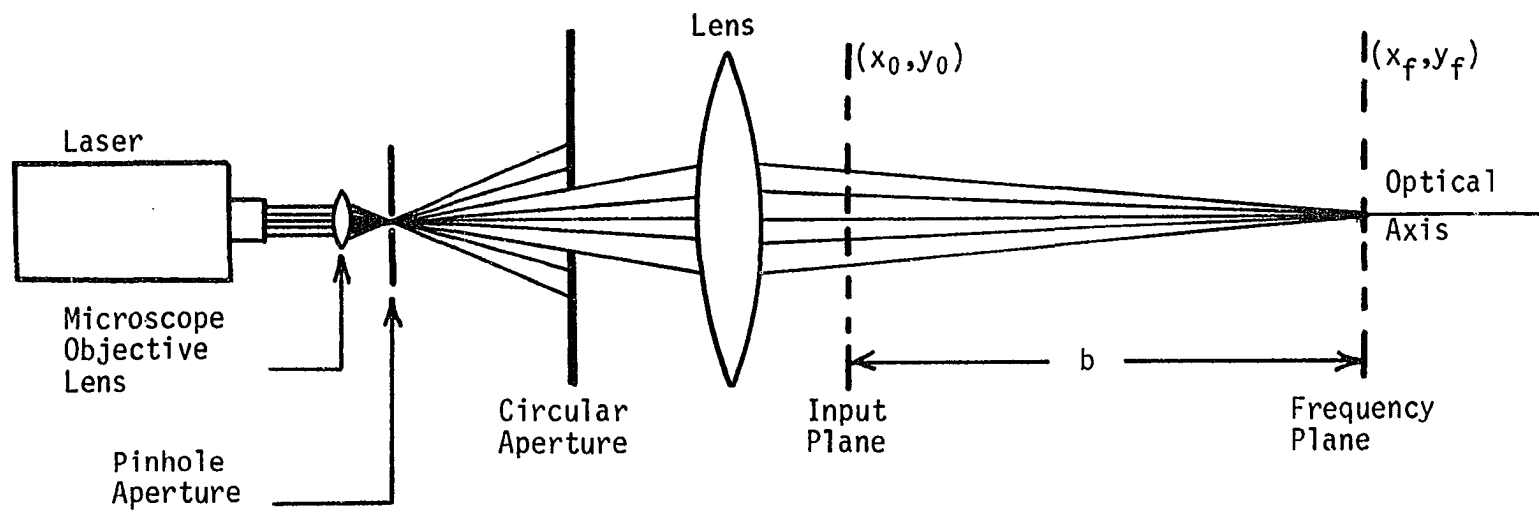
Figure 13. Optical system used to frequency process one-dimensional signals.

region of the lens, the paraxial approximations for a thin lens become applicable. The lens[1] used was a 52 mm diameter, 193 mm focal length, coated, achromatic lens.

A film transparency holder was placed in the input plane located a distance b from the frequency plane. The exact position of the frequency plane was determined by using a technique for locating the image of the point source. This technique involved placing a flat opaque object on the optic axis in the neighborhood of the frequency plane and observing the reflected light distribution on a screen. This reflected distribution was granular in appearance, and as the opaque object was moved along the optic axis, the granular size in this distribution varied. The exact location of the frequency plane was found when a pattern with maximum granular size appeared on the screen. This technique utilizes the spatial coherence of the laser light source and the optical roughness of the reflecting surface.

Detection System

A system was built to detect and record the light intensity as a function of position along the horizontal x_f-axis in the frequency plane.

The light intensity detecting portion of this system consisted of a fiber optic cable, photomultiplier tube[2], and a variable gain amplifier. The fiber optic cable was a single 80 micron diameter glass fiber sealed in a section of opaque electrical wire insulation. One end of the fiber

---

[1] Edmund Scientific Company, Barrington, New Jersey.

[2] Type 150CVP, Amperex Corp., Hicksville, New York.

optic cable was attached to a micromanipulator[1] and could be positioned along the x_f-axis. The other end of the fiber optic cable was placed in a light tight box with the photomultiplier tube, and was directed toward the photoemissive surface of this photomultiplier tube. The output voltage from the photomultiplier tube was amplified using a linear, low frequency, variable gain amplifier. The output voltage from this amplifier was directly related to the light intensity intercepted by the fiber optic cable and was used to control the y-axis of an x-y recorder.[2]

To detect and record spatial information, the shaft of a linear ten-turn potentiometer[3] was mechanically coupled to the positioning control of the micromanipulator. A constant voltage was applied across the fixed resistance terminals of this potentiometer, and voltage between the wiper arm terminal and the ground terminal was used to indicate position. This voltage was directly related to the position distance x_f in the frequency plane and was used to control the x-axis of the x-y recorder. As the fiber optic cable was swept along the x_f-axis, the light intensity as a function of position was plotted on the x-y recorder.

The complete electronic circuit diagrams for this detection system are given in the Appendix.

---

[1] Model 22, W. R. Prior and Co. LTD, England, distributed by Stoelting Co., Chicago, Illinois.

[2] Two models were used: Model 7035B and 7004B, Hewlett-Packard, San Diego, California.

[3] Model 3509, 10 kΩ, Bourns, Inc., Riverside, California.

Signals Processed

Various biological and electronically generated signals were used to demonstrate optical processing. The biological signals were recorded from two anesthetized mongrel dogs. Sections of these waveforms are shown in Figures 14 and 15. The electronically generated signals were mainly sinusoidal waveforms of frequencies below 60 Hz, and amplitudes below 1.0 volt peak-to-peak. These signals were recorded from a function generator.[1]

The electrocardiogram (ECG) and the electroencephalogram (EEG) signals, shown in Figure 14, were recorded from the same experimental animal. The ECG signal was recorded from subdermal needle electrodes placed in the standard Lead II configuration. The EEG signal was recorded from subdermal needle electrodes placed above the left and right frontal lobes of the brain.

The instantaneous blood flow and instantaneous differential blood pressure waveforms shown in Figure 15 were obtained from the femoral artery of a second mongrel dog. The instantaneous flow signals were recorded from an electromagnetic blood flowmeter.[2] The instantaneous differential pressure signals were obtained from pressure transducers[3] placed upstream and downstream along a section of the femoral artery. The flow and pressure signals shown in Figure 15c and 15d were recorded under a

---
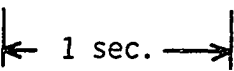
[1]Model 134, Wavetek, San Diego, California.

[2]Model BL-610, Biotronex Laboratory, Inc., Silver Spring, Maryland.

[3]Model P-23Dc, Statham Instruments, Inc., Oxnard, California.
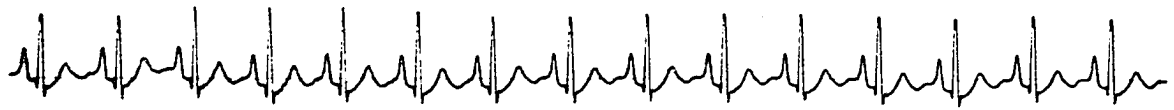
(a)

|← 1 sec. →|

(b)
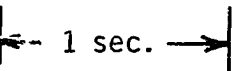
|← 1 sec. →|

Figure 14. Examples of signals analyzed.

(a) Electrocardiogram recorded from an anesthetized dog.
(b) Electroencephalogram recorded from the same experimental animal.

Figure 15. Examples of signals analyzed.

   (a) Normal instantaneous blood flow in the femoral artery of
        an anesthetized dog.
   (b) Normal instantaneous differential blood pressure along a
        section of the femoral artery from the same experimental
        animal.
   (c) Instantaneous blood flow in the femoral artery of the same
        experimental animal under a simulated stenotic condition.
   (d) Instantaneous differential blood pressure in the femoral
        artery of the same experimental animal recorded across the
        occluded plug.

(a) |← 1 sec. →|

(b) |← 1 sec. →|

(c) |← 1 sec. →|

(d) |← 1 sec. →|

simulated stenotic condition. A polycarbonate plug with a machined center diameter was placed in the femoral artery to reduce the cross-sectional area and simulate a 75 percent area occlusion.

Each of the signals shown in Figures 14 and 15 were initially recorded on a magnetic tape recorder[1] as time varying voltages of approximately 1.0 volt peak-to-peak maximum amplitude.

Data Input Format

Area modulation format

In this research, the primary method used to record signals on photographic film in area modulated format was to transcribe these signals onto area modulated motion picture sound track.[2] Biological signals (ECG and EEG) and low frequency (0.5 Hz to 50 Hz) sinusoidal signals were initially recorded on magnetic tape. The signals were then recorded onto 16 mm sound track film at 128 times their initial recording rate. By recording at this increased rate, these low frequency signals were then compatible with the frequency band pass characteristics of the sound track recording system. The velocity of the photographic film in this sound track recording system was 18.3 centimeters per second. Thus one centimeter of sound track film contained 7 seconds of real time data, and initial signal frequencies in the range of 0.5 Hz to 50 Hz were represented on the area modulated transparency by spatial frequencies in the range of 3.5 to 35 cycles/millimeter.

---

[1]Model FR-1300, Ampex Corp., Redwood City, California.

[2]Courtesy of the Film Production Unit, Iowa State University, Ames, Iowa.

A photographic print of a section of the ECG signal recorded on this area modulated format is shown in Figure 16.

Figure 16.   A photographic print of a section of the canine ECG signal recorded on 16 mm area modulated sound track.

A second technique for recording signals on photographic film in area modulated format was tested.   This method involved adding a constant amplitude 80 Hz sinusoidal voltage to the signal of interest and then electronically removing the negative half of this sum.   The resulting signal was then recorded on unlined chart paper using a rectilinear chart recorder.[1]   This procedure is illustrated in Figure 17 and the electronic circuit used to perform this operation is given in the Appendix.

The chart recorded paper speed was set at 2.5 centimeters/second, and at this paper speed the recording pen completely darkened the area below the signal.   The result was an area modulated record of the data.   A section of this chart recording was then photographed using a high contrast, black and white, 35 mm film.[2]   The developed negative was used as the

---

[1]Model R-411, Beckman Instruments, Inc., Schiller Park, Illinois.

[2]Type HC-135, Kodak High Contrast Copy Film, Eastman Kodak Company, Rochester, New York.   All high contrast film used in this research was this type.
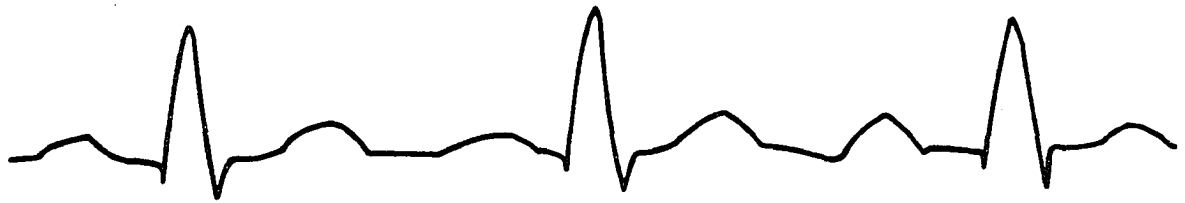
(a)
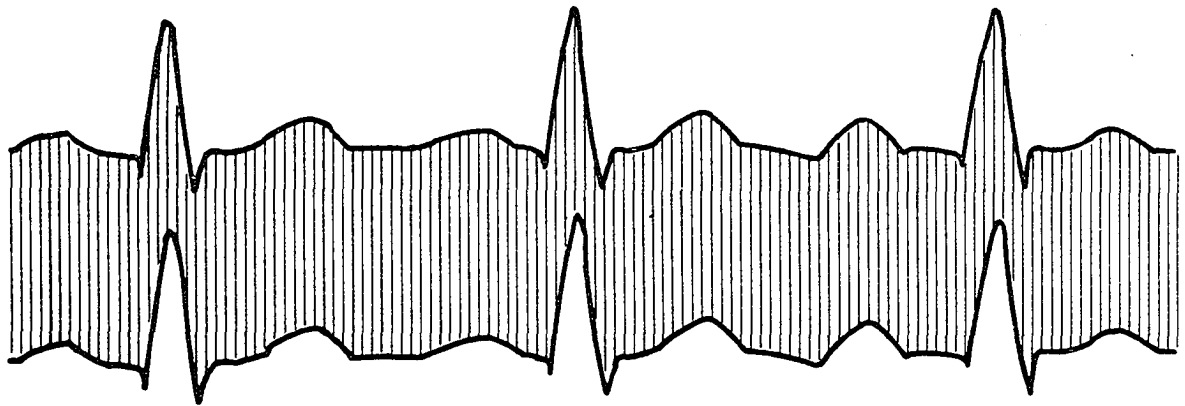
(b)
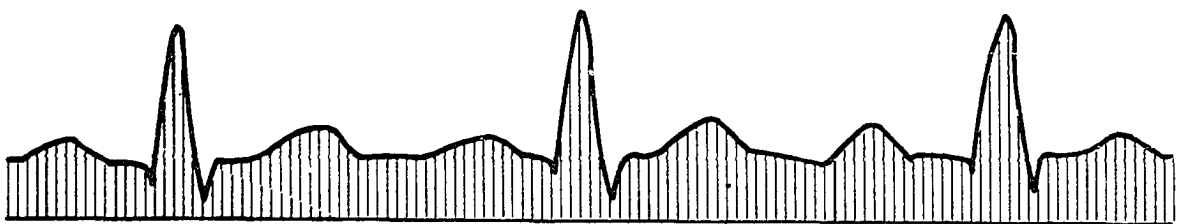
(c)

Figure 17. An illustration of the technique for obtaining an area modu-
lated signal on a strip chart recorder.

(a) The line tracing of the desired signal.
(b) The sum of the signal with a high frequency bias.
(c) The same as (b) but with the lower half clipped off.

input transparency to the optical system. A one centimeter length of this transparency corresponded to 5.3 seconds of real time data.

A photographic print of the canine ECG signal transparency produced by this technique is shown in Figure 18a.

An alternate method of producing an area modulated strip chart recording was investigated. This method involved hand darkening the area below the single line chart recording of the signal. A section of the hand darkened area modulated chart record of the canine ECG signal is given in Figure 18b. This chart record was photographed using high contrast black and white film, and the processed negative was used as the input area modulated transparency in the optical system.

Single line format

The single line data input format was implemented by recording the signals on unlined chart paper. A rectilinear chart recorder[1] was used with the paper speed set at 2.5 centimeters/second. A section of the chart recording was photographed using high contrast black and white film. The developed negative was used as the input transparency in the optical system.

Density modulation format

A system was developed to record a signal g(t) on 35 mm, high contrast, black and white photographic film in a density modulated format. This system employed a technique to intensity modulate an oscilloscope[2]

---

[1]Model R-411, Beckman Instruments, Inc., Schiller Park, Illinois.

[2]Type 561, Tektronix, Inc., Beaverton, Oregon.

Figure 18a. A photographic print of a transparency made by photographing an area modulated strip chart recording.

Figure 18b. An area modulated chart recording produced by hand darkening the area below the single line chart record of the signal.

beam by varying the writing rate of the oscilloscope beam. A rationale

for applying this technique was to produce a beam with intensity charac-

teristics inversely related to g(t) raised to a power c. Referring to the

previous discussion of density modulation, specifically the discussion

leading to Equation 1-63, it is evident that processing the exposed film

for the conditions that $\gamma c = 2$ will produce a transparency with amplitude

transmittance characteristics directly related to the input signal as re-

quired for accurate optical computations.

A block diagram of the technique used to intensity modulate the

oscilloscope beam is shown in Figure 19. The complete electronic circuit

diagram for each component section is given in the Appendix. The input

signal g(t) to this system was assumed to be a low frequency (below 60 Hz)

signal with a maximum amplitude of 1.0 volt peak-to-peak. A positive

constant bias voltage was added to g(t). The magnitude of this bias

voltage was chosen to insure that output signal from the electronic summer
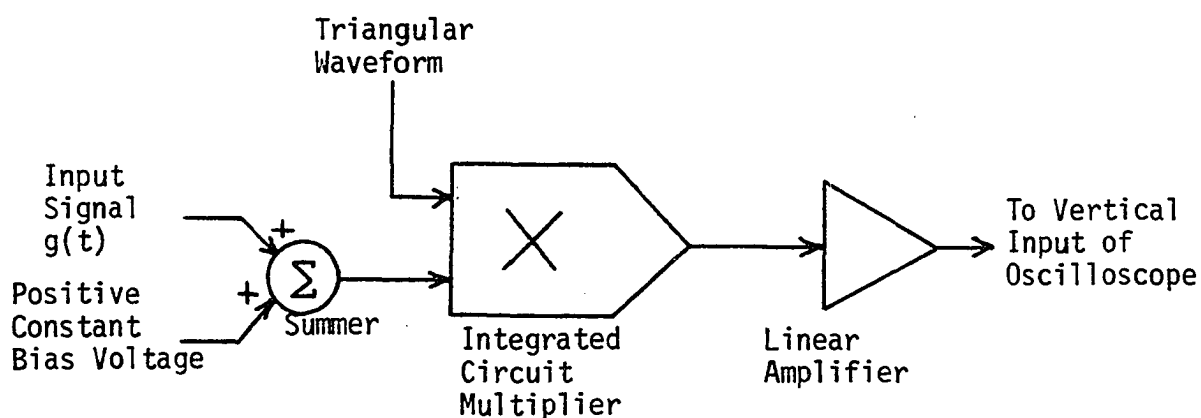
Figure 19. Block diagram of the technique used to intensity modulate an oscilloscope beam.

was positive even for negative values of g(t). This permitted recording
the negative as well as the positive portions of g(t). The output signal
from the summer was then used to amplitude modulate a 4 volt peak-to-peak
5 kHz triangular waveform. This modulated waveform was linearly amplified
and the output of the amplifier was connected to the vertical input[1] of
the oscilloscope. The initial values for the constant bias voltage and
the amplifier gain were set so that the minimum input waveform to the
oscilloscope was 1.0 volt peak-to-peak.

The graticule on the oscilloscope was removed and the cathode ray
tube[2] (CRT) was masked using opaque black tape to form a rectangular dis-
play area 9 cm long and 7 cm high. The vertical sensitivity of the oscil-
loscope was set at 0.1 volts/centimeter and the horizontal sweep rate was
set at 0.33 seconds/centimeter. At this vertical sensitivity and sweep
rate, a single vertical beam was linearly deflected across the CRT. The
beam width was approximately 0.75 mm and the beam height was directly re-
lated to the input signal g(t) plus the constant bias voltage. However,
since the CRT was masked in the vertical dimension, the beam height ap-
peared to be constant and only the intensity varied as a function of g(t)
because of the changing beam writing rate. The beam writing rate in-
creased as the amplitude of g(t) increased and thus the beam intensity
decreased. Conversely, as g(t) decreased, the beam writing rate also de-
creased and the beam intensity increased. Thus, as the beam was linearly

---

[1]Type 3A72 Amplifier Unit, Tektronix, Inc., Beaverton, Oregon.

[2]The oscilloscope used in this research contained a type P-2 phosphor
cathode ray tube.

deflected across the CRT, the intensity at any instant along the vertical beam was constant and inversely related to g(t) at that instant.

The intensity characteristics of this beam as a function of g(t) were assumed to be

$$I = K/[B+g(t)]^c \qquad (1-71)$$

where K, B, and the exponent c are constants. The form for this equation was chosen because it was a good approximation to the physical system, and also because of the computational requirement of having a power relationship between the beam intensity and g(t). It is recalled that a power relationship is required so that the film processed for the conditions $\gamma c = 2$ would produce a transparency with amplitude transmittance directly related to the signal of interest.

It was experimentally determined from horizontally static beam intensity measurements as a function of constant input signal voltages that the terms K, B, and c in Equation 1-71 were dependent upon the oscilloscope intensity level setting, the input bias voltage, and the amplifier gain. However, these static measurements were not an accurate representation of the dynamic horizontal sweep situation. The slight intensity halo around the oscilloscope beam and the phosphor decay time could not be included in these static measurements. Thus, the exact values for the terms K, B, and c could not be predicted. The static measurements did, however, indicate the parameters controlling the exponent c. The magnitude of c was dependent upon the oscilloscope intensity level setting and the amplifier gain. In particular, c was directly related to the oscilloscope intensity level setting and inversely related to the amplifier gain. This information, combined with a knowledge of the parameters controlling the

film gamma, was then used in a trial and error procedure to match the beam intensity characteristics of this particular CRT to the film processing. The rationale for this procedure was to negate the requirements of knowing the exact value of c and also gamma in producing the desired result that $\gamma c = 2$.

The criterion for this procedure was to accurately record a 1.0 volt peak-to-peak signal over the maximum film density limits within the linear region of the film density-log exposure characteristic curve. Recording the signal over the maximum film density limits insured that the optical signal to noise ratio was optimized. However, this implied producing a wide range of intensities from the CRT. The wide range in intensities then required increasing the amplifier gain and thus lowering the value of the exponent c. The requirement that $\gamma c = 2$ then necessitated a higher film gamma. Inasmuch as gamma can not be increased above a certain value, it was decided to maximize gamma and correspondingly adjust the value of c by changing the oscilloscope intensity level setting and the amplifier gain until the 1.0 volt peak-to-peak signal was accurately represented on film.

The input test signal used in this trial and error procedure was a 10 Hz 1.0 volt peak-to-peak sinusoidal voltage. A sinusoidal signal was chosen as the test signal because information concerning the signal amplitude and the harmonic distortion in the signal is readily obtainable from the frequency spectrum of this signal.

The input bias voltage was set at 580 mv. A single lens reflex camera[1] was attached to the oscilloscope at a distance of 45 cm from the CRT. The oscilloscope time base generator[2] was equipped with a single sweep mode, thus permitting the camera shutter to be held open while a single linear sweep of the beam was recorded on film. With a relative lens aperture setting of $f/2.8$, single linear sweeps of the sinusoidal signal were recorded for one amplifier gain setting and various oscilloscope intensity level settings. The exposed film was then processed using the following procedure.

1) The exposed film was developed in a high contrast developer[3] for 8 minutes at 68°F, with agitation at 30 second intervals.

2) The film was placed in a stop bath[4] solution for 30 seconds at 68°F to neutralize the action of the developer.

3) The film was placed in a fixer[5] solution for 2 minutes at 68°F.

4) The film was washed in water for 20 minutes at 68°F to remove residual chemicals remaining in the emulsion.

5) The surface water was removed using a photographic squeegee, and the processed film was then dried by evaporation.

---

[1]Model F, f:1.9 50 mm lens, Miranda Camera Company, LTD., Tokyo, Japan.

[2]Type 2B67, Tektronix, Inc., Beaverton, Oregon.

[3]Kodak D-19 Developer, Eastman Kodak Company, Rochester, New York.

[4]Kodak Indicator Stop Bath, Eastman Kodak Company, Rochester, New York.

[5]Kodak Rapid Fixer with Hardener, Eastman Kodak Company, Rochester, New York.

The film developing process was taken to completion by this technique and further increasing the developing time or the developer temperature had little effect on gamma. The value of gamma was at a maximum for this film ($\gamma \approx 3$).

The developed transparencies were then optically processed, and from the optically computed spectrum it was possible to measure the relative signal amplitude and the harmonic distortion in each transparency. The method used to compute harmonic distortion is given in a subsequent section on the experimental results. Using an iterative trial and error procedure, the amplifier gain and the oscilloscope intensity level setting were adjusted to produce the minimum harmonic distortion and the maximum amplitude in the signal record. The amplifier gain and the intensity level setting determined by this iterative procedure were used in recording all the density modulated signal transparencies. The final amplifier gain was such that a 1.08 volt input signal plus constant bias voltage produced a 14 volt peak-to-peak triangular waveform as the vertical input waveform to the oscilloscope.

Photographic prints of two density modulated signal transparencies are shown in Figure 20. A one centimeter length of these transparencies corresponded to 2 seconds of real time data.
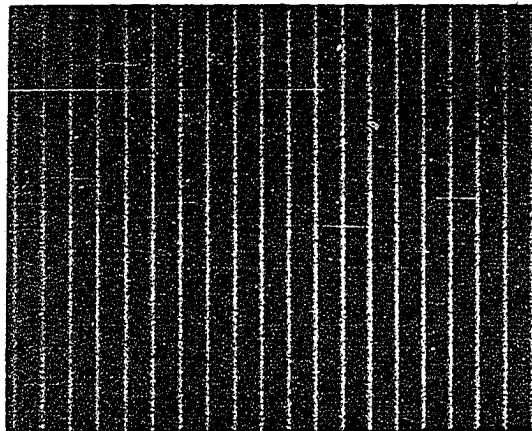
(a)
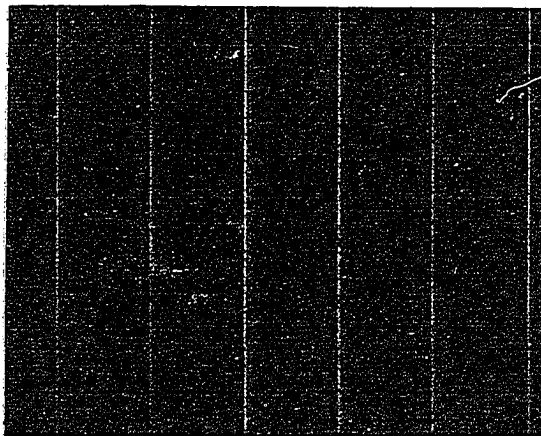
(b)

Figure 20. Photographic prints of density modulated transparencies.

(a) A 1.0 volt peak-to-peak 10 Hz sinusoidal signal.
(b) A section of the canine ECG signal.

EXPERIMENTAL RESULTS AND DISCUSSIONS

Area Modulation Format

Motion picture sound track method

The system used in optically processing signals recorded on 16 mm sound track film is shown in Figure 13. The distance, b, from the input plane to the frequency plane was 80 cm.

A series of sinusoidal voltages was recorded on sound track film to determine a transfer function for this area modulated method. This series contained one minute segments of sinusoidal voltages in the amplitude range of 0.15 volt peak-to-peak to 1.0 volt peak-to-peak and in the frequency range of 2 Hz to 50 Hz. The sound track film transparency was placed in the input plane of the optical system and 2 cm sections of this transparency were optically processed. The length of each section processed corresponded to 14 seconds of real time data.

The detection system described in a previous section was used to obtain x-y plots of the relative intensity distribution along the x_f-axis in the frequency plane. These plots were made in the vicinity of the fundamental frequency component for each sinusoidal signal. Figure 21 shows two overlapping plots of the relative intensity versus distance in the frequency plane for the fundamental frequency component of a 10 Hz 0.6 volt peak-to-peak sinusoidal signal. Each profile was computed from a different 14 second segment of this signal. The variation in the intensity peaks for these two profiles was primarily the result of nonuniform recording speeds in the magnetic tape recorder and/or the sound track
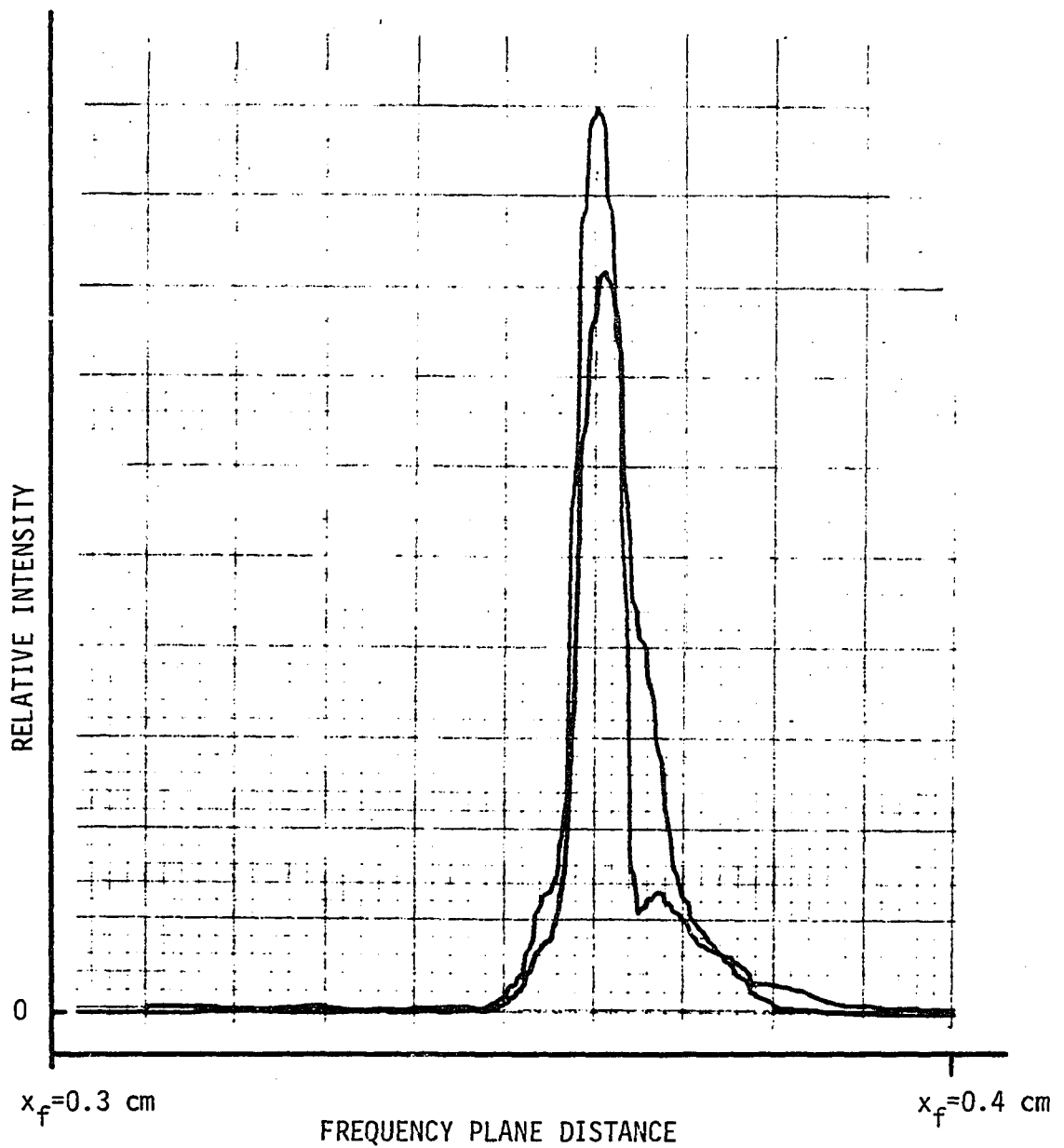
Figure 21. Two overlapping profiles of the relative intensity versus distance in the frequency plane for the fundamental frequency component of a 10 Hz 0.6 volt peak-to-peak sinusoidal signal. This signal was recorded on 16 mm area modulated sound track film, and each profile was computed from a different 14 second segment of this signal.

recording system, or random phase variations in the input film trans-
parency. These phase variations could be reduced by the use of a liquid
gate.

To determine a transfer function for this area modulated method, the
area beneath each x-y plot was measured using a planar planimeter. This
area is directly related to the relative light intensity of the fundamen-
tal frequency component. The relative light intensity is in turn directly
related to the square of the amplitude of the recorded signal. The com-
puted areas were grouped according to the peak-to-peak signal amplitudes
they represented. The areas for the signals in each group were then nor-
malized to the area of the 25 Hz signal within that group. The average
normalized area at each signal frequency was then determined and these
results are shown in Figure 22. The vertical axis of this graph repre-
sents the average of the normalized areas and has been designated as the
normalized intensity inasmuch as the areas are directly related to the
light intensity. This graph represents a type of transfer function for
the sound track area modulated method.

The graph shown in Figure 23 is a similarly computed transfer func-
tion. This graph was made by first computing the square root of the area
beneath the plot. These computed values are directly related to the
relative light amplitude and thus are directly related to the signal
amplitude. The vertical axis of this graph is the average of the normal-
ized square root of the area and has been designated as normalized ampli-
tude for brevity.

The shape of the transfer function for this area modulated method is
primarily the result of the characteristics of the sound track recording

Figure 22. A transfer function for the 16 mm area modulated sound track
method computed on a relative light intensity basis as de-
scribed in the text.

Figure 23. A transfer function for the 16 mm area modulated sound track
method computed on a relative light amplitude basis as de-
scribed in the text.

NORMALIZED AMPLITUDE

NORMALIZED INTENSITY

FREQUENCY (Hz)

FREQUENCY (Hz)

78
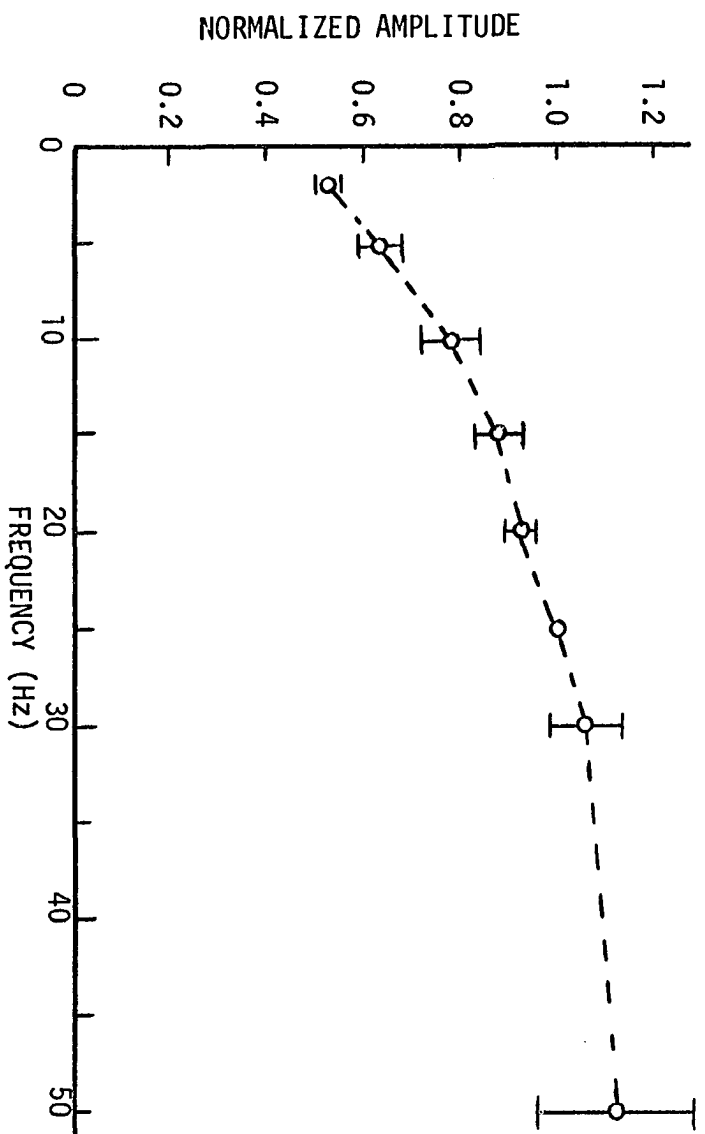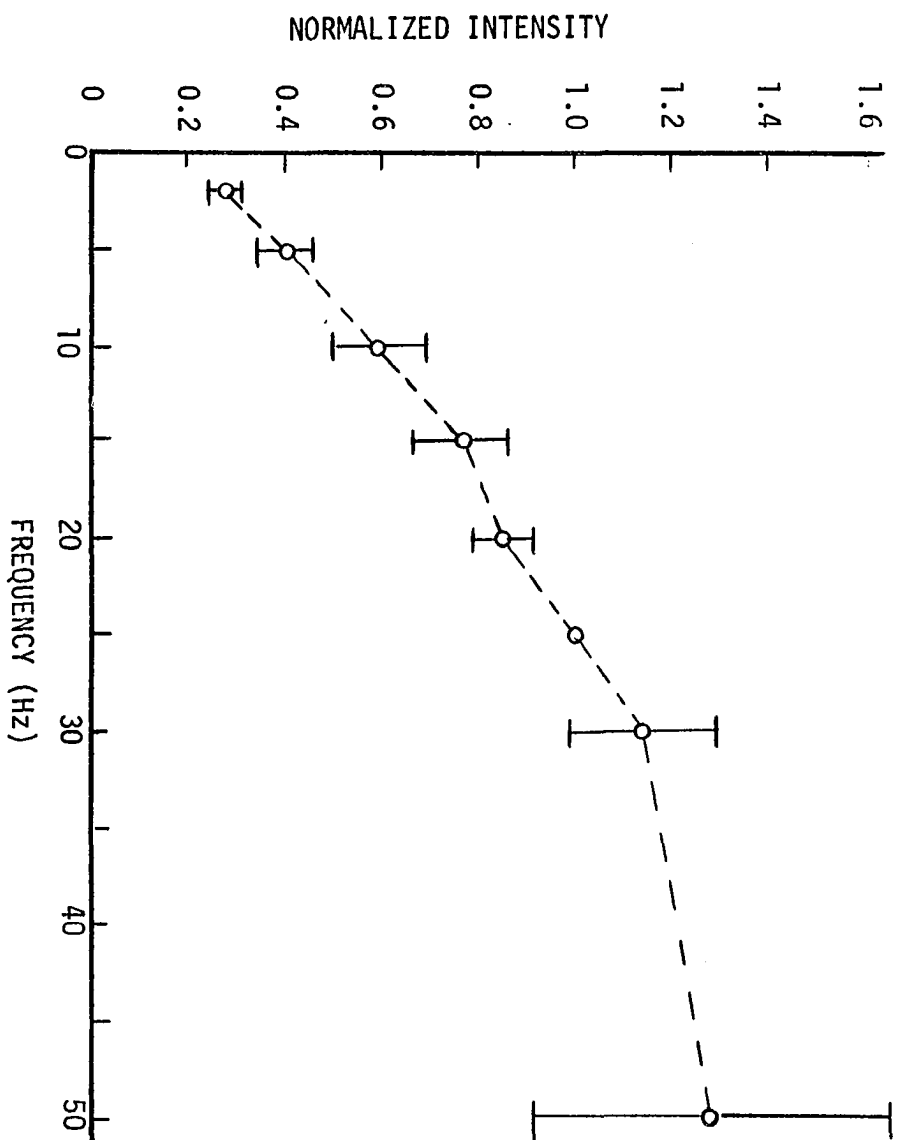
system. Low frequency signals are attenuated in this system to increase the clarity of the optically reproduced sound.

The harmonic distortion produced by this recording method was determined from the transcribed sinusoidal signals. The procedure used to determine harmonic distortion involved measuring the relative light intensity at the fundamental frequency component and at the harmonic frequency components for each particular sinusoidal signal. The intensity measurements were made using a 0.5 mm diameter single plastic fiber optic cable and a silicon photovoltaic light sensor.[1] The terminals of this light sensor were connected across a 3.4 kΩ load resistor. The voltage generated by the light sensor is directly related to the light intensity intercepted by the fiber optic cable. This voltage was linearly amplified and the magnitude of the amplified voltage indicated a relative measure of the light intensity. The harmonic distortion was then defined as

$$\text{Harmonic Distortion} = \frac{\left[\sum_n I_n^2\right]^{1/2}}{I_F} \qquad (1\text{-}72)$$

for n = 2,3,4,...

where I_n is the relative light intensity produced by the n-th harmonic frequency component, and I_F is the relative light intensity produced by the fundamental frequency component.

A graph of the percent harmonic distortion as a function of frequency for the 0.8 volt peak-to-peak sinusoidal signals is given in Figure 24. Also, a graph of the percent harmonic distortion as a function of input signal amplitude for the 25 Hz sinusoidal signals is given in Figure 25.

---

[1]Type LS-222, Texas Instruments, Inc., Dallas, Texas.

Figure 24. Percent harmonic distortion as a function of frequency for
0.8 volt peak-to-peak sinusoidal signals recorded on 16 mm
area modulated sound track film.

Figure 25. Percent harmonic distortion as a function of input signal
amplitude for 25 Hz sinusoidal signals recorded on 16 mm
area modulated sound track film.

PERCENT HARMONIC DISTORTION

PERCENT HARMONIC DISTORTION

FREQUENCY (Hz)

INPUT SIGNAL AMPLITUDE (peak-to-peak voltage)

81
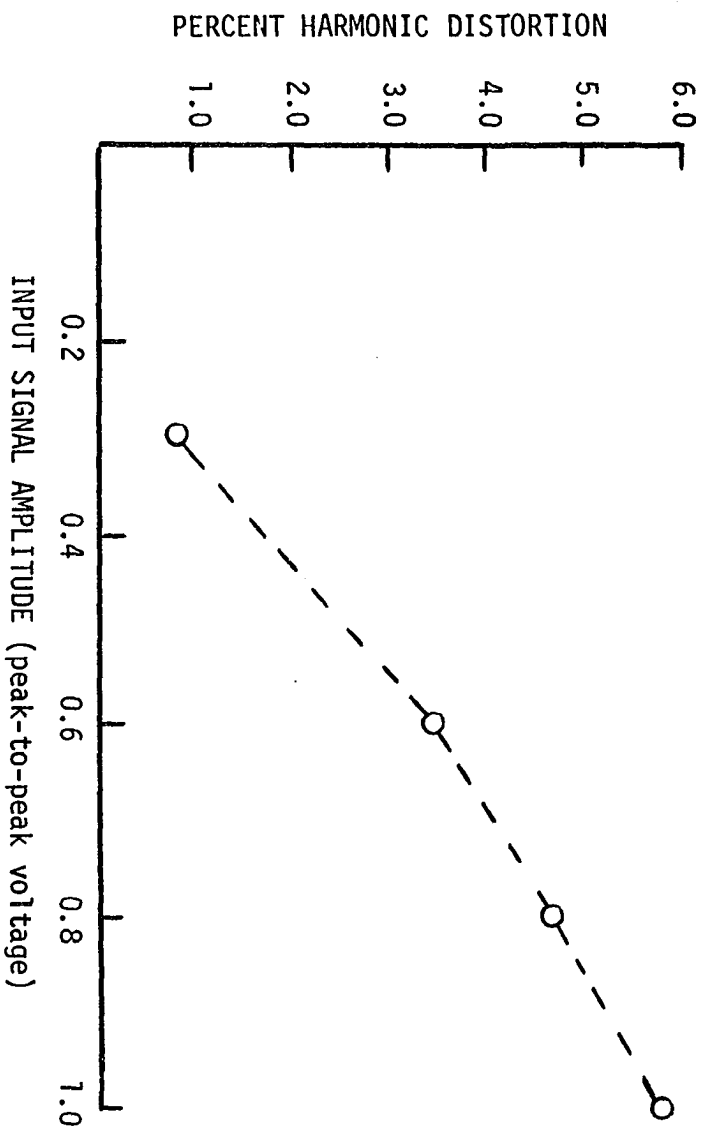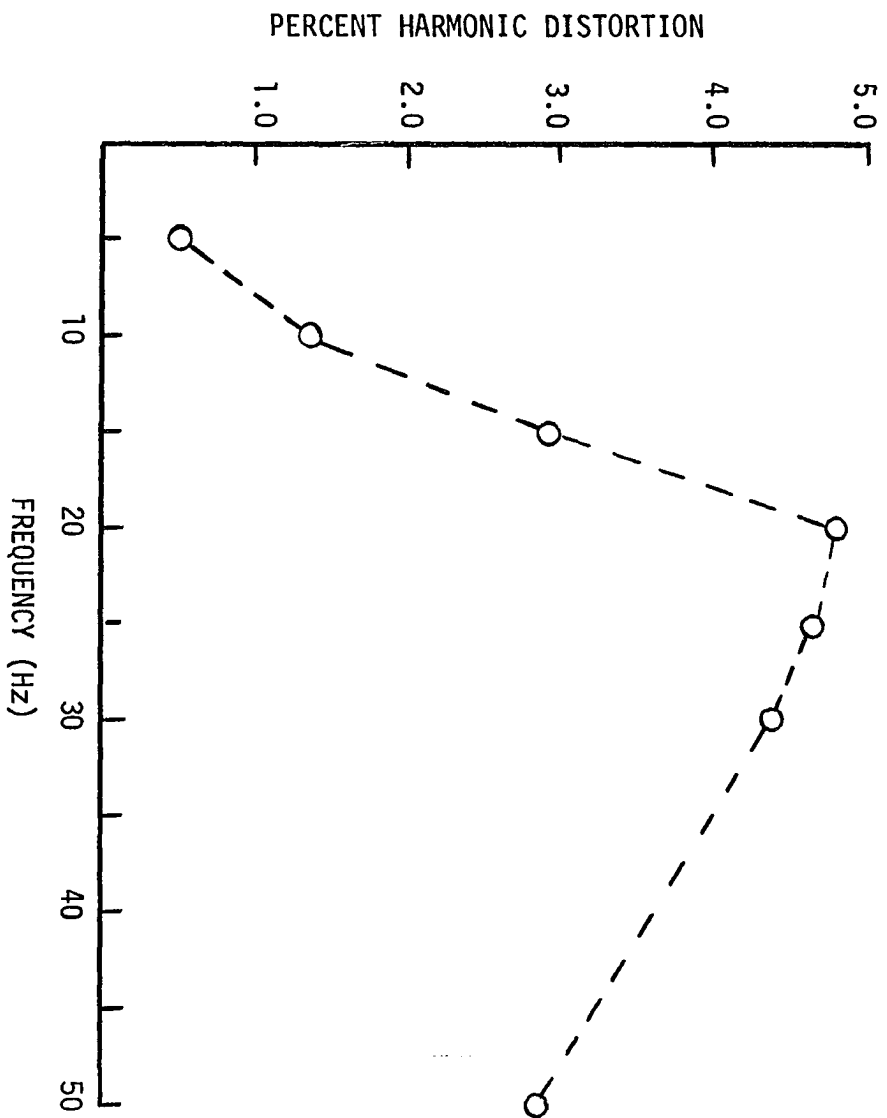
The harmonic distortion of signals recorded on sound track film was principally the result of the film exposure and development process. The peaks of the recorded signals were partially distorted by a photographic effect called halation. This is caused by the spreading or reflection of light in the photographic film itself. The recorded image is also spread somewhat, due to the development process. Unexposed silver halide crystals in proximity to highly exposed crystals are also developed.

A photograph of the intensity distribution in the frequency plane for a 25 Hz 0.8 volt peak-to-peak sinusoidal signal is shown in Figure 26a. Note the complexity of the off-axis pattern in this distribution. However, also note that essentially only one component exists along the x_f-axis ($y_f = 0$ axis) as predicted by Equation 1-48 for a sinusoidal case. The energy density spectrum plot[1] for this sinusoidal signal is shown in Figure 26b. This spectral profile was produced by moving the 80 micron diameter single fiber optic along the x_f-axis and recording on the x-y recorder the intercepted light intensity as a function of position x_f. For convenience, two horizontal scales have been indicated on this plot. One scale indicates the distance x_f in the frequency plane, while the second scale is the representative frequency in Hz. This frequency scale was computed by the relationship

$$f_R = f_x/7 = x_f/7\lambda b \qquad (1\text{-}73)$$

---

[1] The energy density spectrum plots will be denoted as spectral profiles for brevity in the remaining sections of this dissertation.
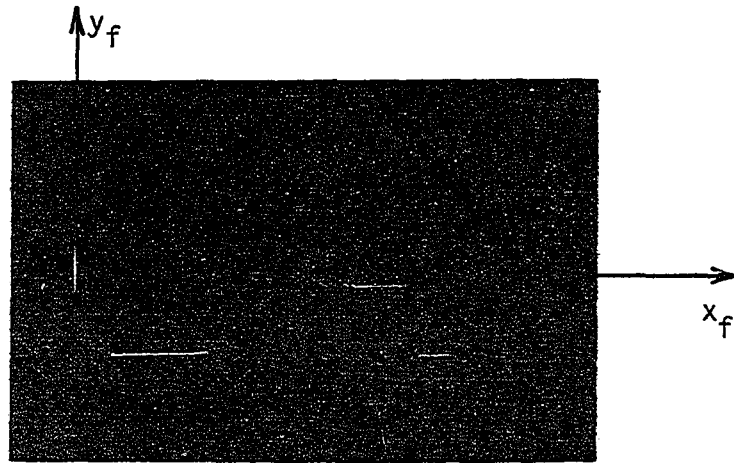
Figure 26a. Photograph of the intensity distribution in the frequency plane for a 14 second segment of a 25 Hz 0.8 volt peak-to-peak sinusoidal signal recorded on 16 mm area modulated sound track film.
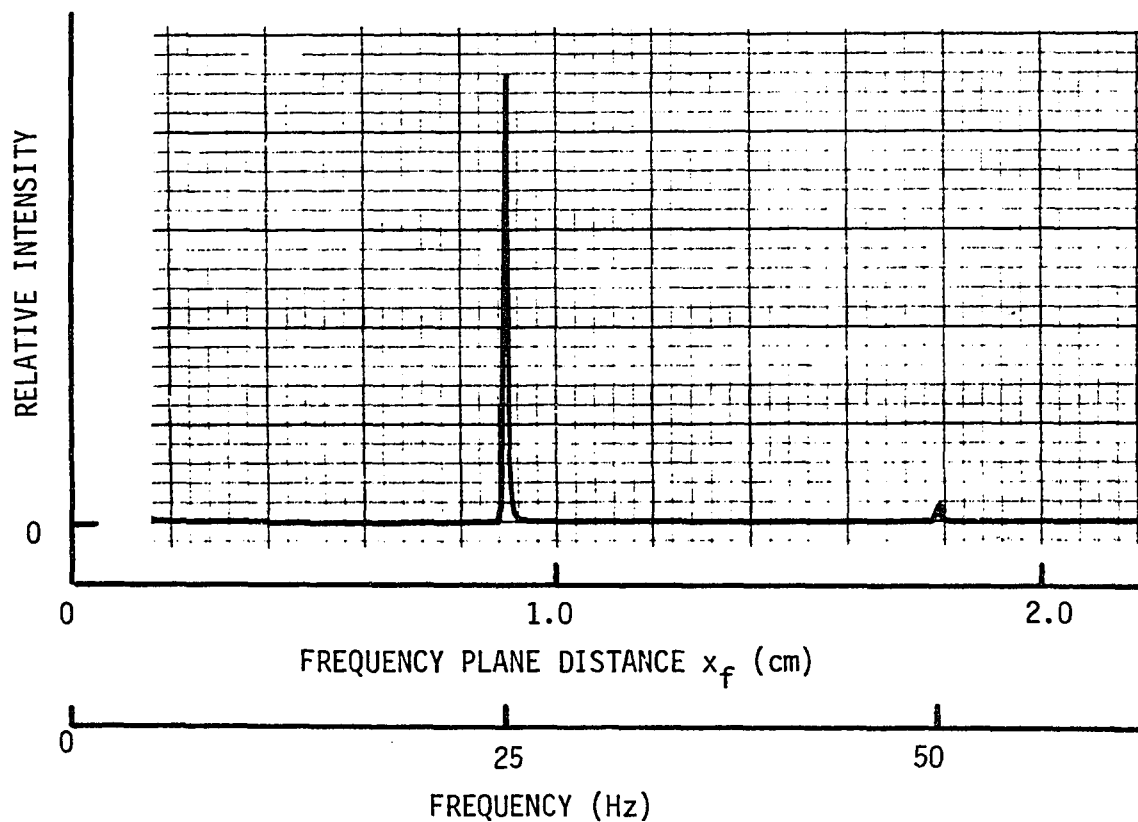

Figure 26b. The optically computed spectral profile for this 25 Hz 0.8 volt peak-to-peak sinusoidal signal.

where:

f_R = input signal frequency (Hz)

f_x = spatial frequency of the input signal represented on area modulated sound track film (cycles/cm)

x_f = distance along the x_f-axis in the frequency plane (cm)

λ = wavelength of illuminating light = $0.6328 \ 10^{-4}$ cm

b = distance between input plane and frequency plane = 80 cm

The spectral profile for a 7 second segment of the canine ECG signal is shown in Figure 27. Inasmuch as this signal was approximately periodic over the transformed interval, the spectral profile is essentially a line spectrum. The nearly discrete spectral peaks in this profile indicate the presence of nearly discrete frequency components within the signal. These frequency components are harmonics of the fundamental frequency which was equal to the heart rate of approximately 180 beats/minute or 3 beats/second. The envelope connecting the spectral peaks contains frequency information related to the shape of a single ECG pulse.

To demonstrate the power and versatility in applying optical processing to the analysis of long data records, a type of spectrogram was obtained for the ECG data record. This result is shown in Figure 28. Spectral profiles for consecutive 17.5 second segments of the ECG data record were obtained by advancing the input transparency in discrete 2.5 cm increments and then recording the spectral profile for each of these 2.5 cm sections. The typical spectrogram, however, is an intensity record as a function of time. Since intensity variations are difficult to quantitatively evaluate, Figure 28 represents one way of presenting spectro-
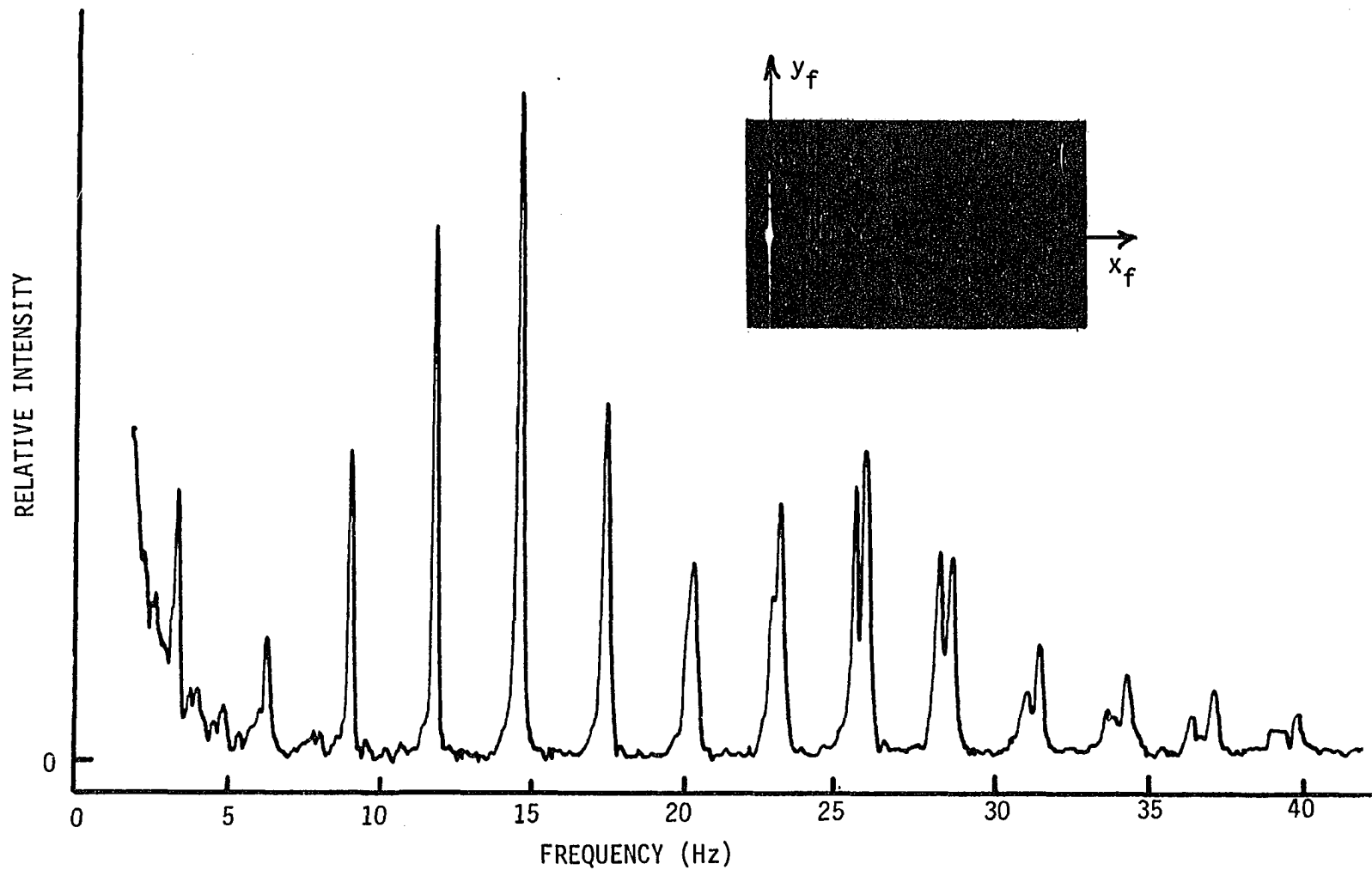
Figure 27. Optically computed spectral profile for a 7 second segment of the ECG signal recorded on 16 mm area modulated sound track film. The insert is a photograph of the intensity distribution in the frequency plane for this ECG signal.
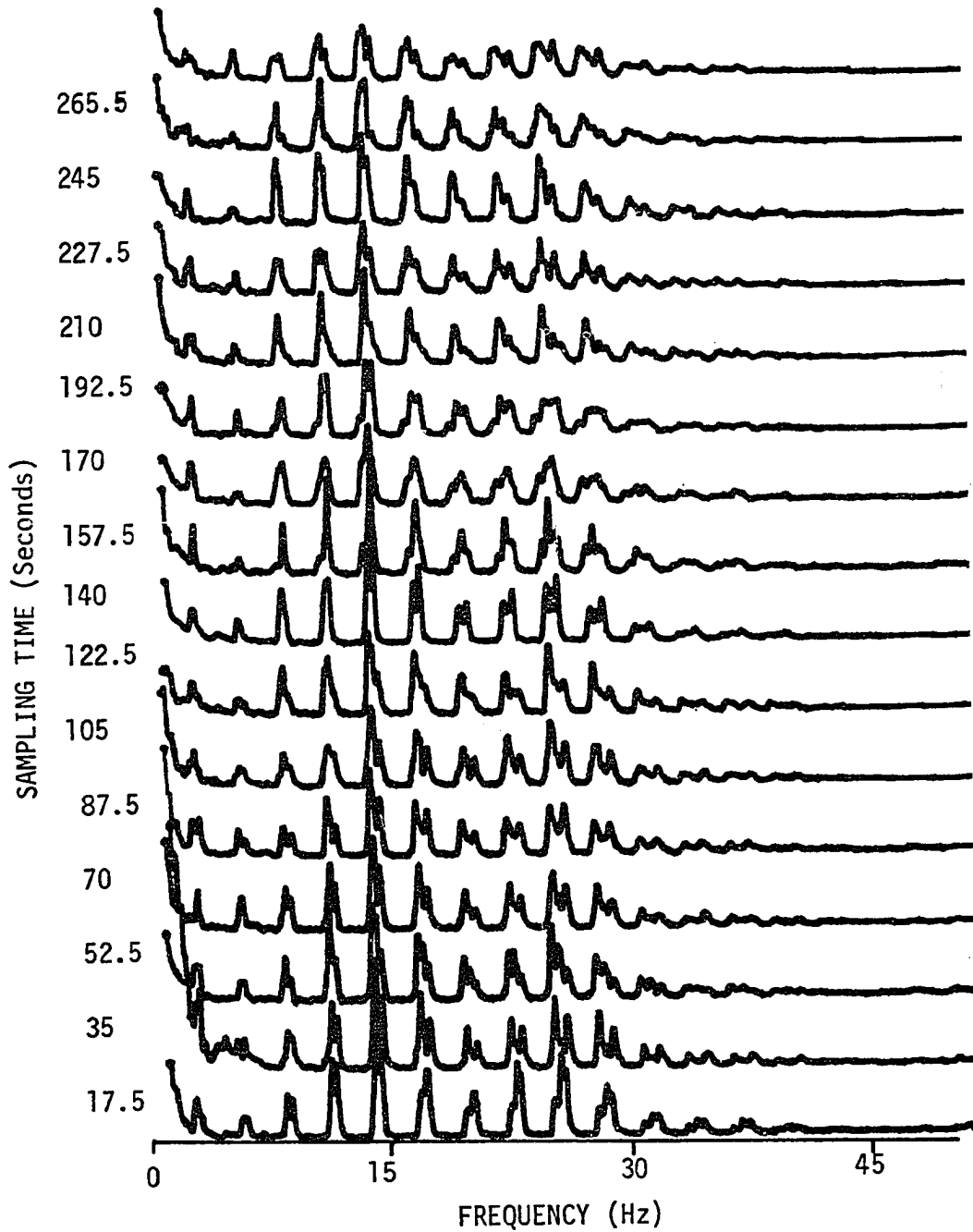
Figure 28. Optically computed spectral profiles for 280 seconds of the canine ECG data with each profile corresponding to 17.5 seconds of real time data.

gram data in a form that is of greater value in applications where the detection of small amplitude and shape changes is desired.

It should be noted that spectral analysis of ECG signals is not usually made because the time domain description adequately depicts prevalent information about the electrical activity of the heart. However, the ECG data record, specifically the section of this signal analyzed in Figure 27, was used to compare the various optical data input formats. The ECG signal is a sufficiently complicated waveform that a spectral profile of this signal is nontrivial, and since this signal was nearly periodic, small discrepancies in not processing exactly the same segment of the data record will not adversely effect the validity of this comparison.

The spectral profile shown in Figure 29a was computed from a section of the canine EEG signal. An expanded plot of this spectral profile is given in Figure 29b. The EEG signal is primarily used for characterizing the continuous electrical activity of the brain. The clinical use of this signal resides in the detection of physiological abnormalities such as epilepsy or to localize brain tumors. The EEG siqnal, unlike the ECG signal, is nonperiodic and random, and although normal EEG signals consist of many different frequencies, usually one frequency band predominates. This frequency band varies greatly with different behavioral states. Thus the value of a spectral profile for a section of the EEG signal lies specifically in characterizing the frequency distribution of the signal energy. From the plots shown in Figures 29a and 29b, it is evident that a majority of the EEG energy is contained within the frequency band below 5 Hz. This
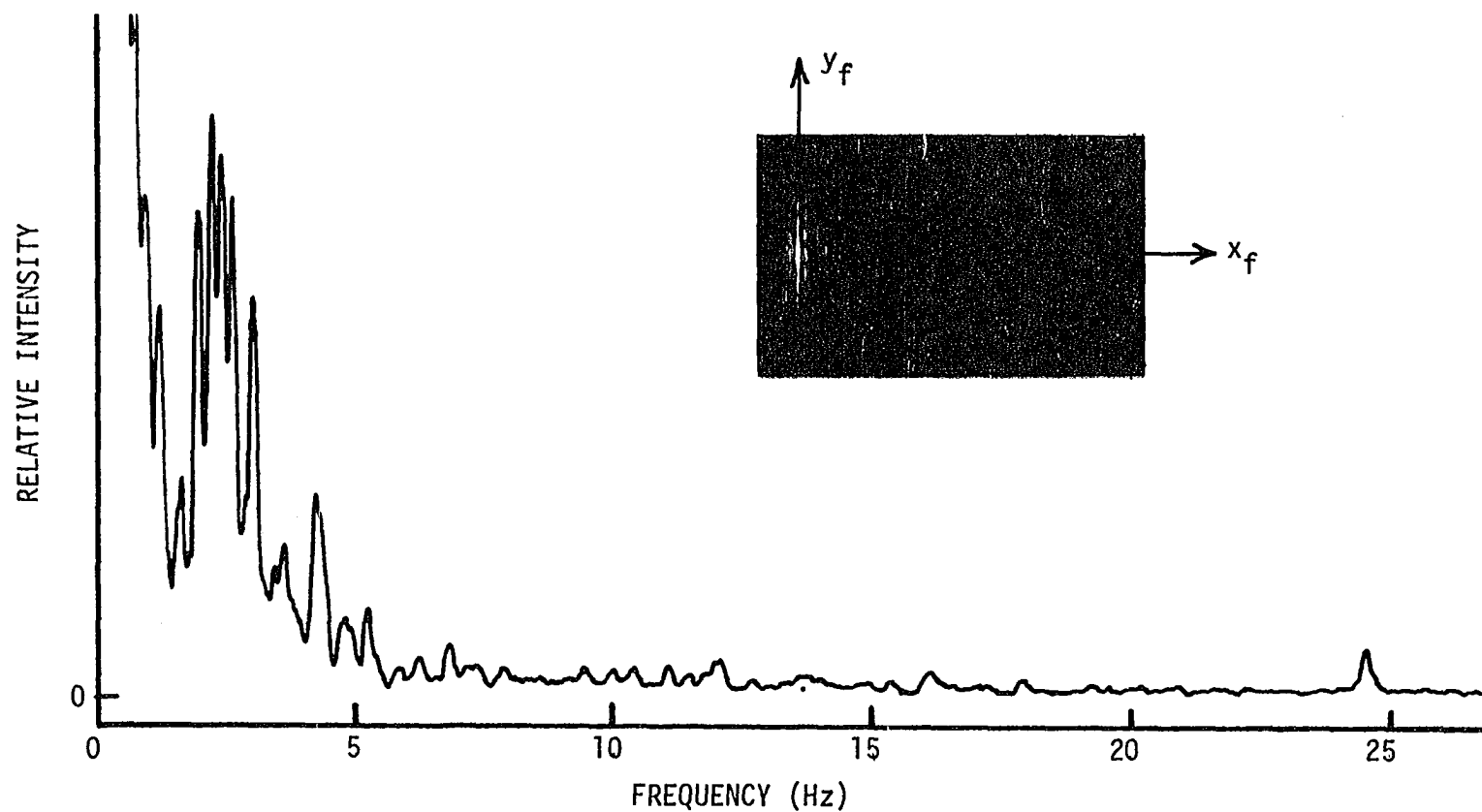
Figure 29a. Optically computed spectral profile for 14 seconds of the EEG signal recorded on 16 mm area modulated sound track film. The insert is a photograph of the intensity distribution in the frequency plane for this EEG signal.
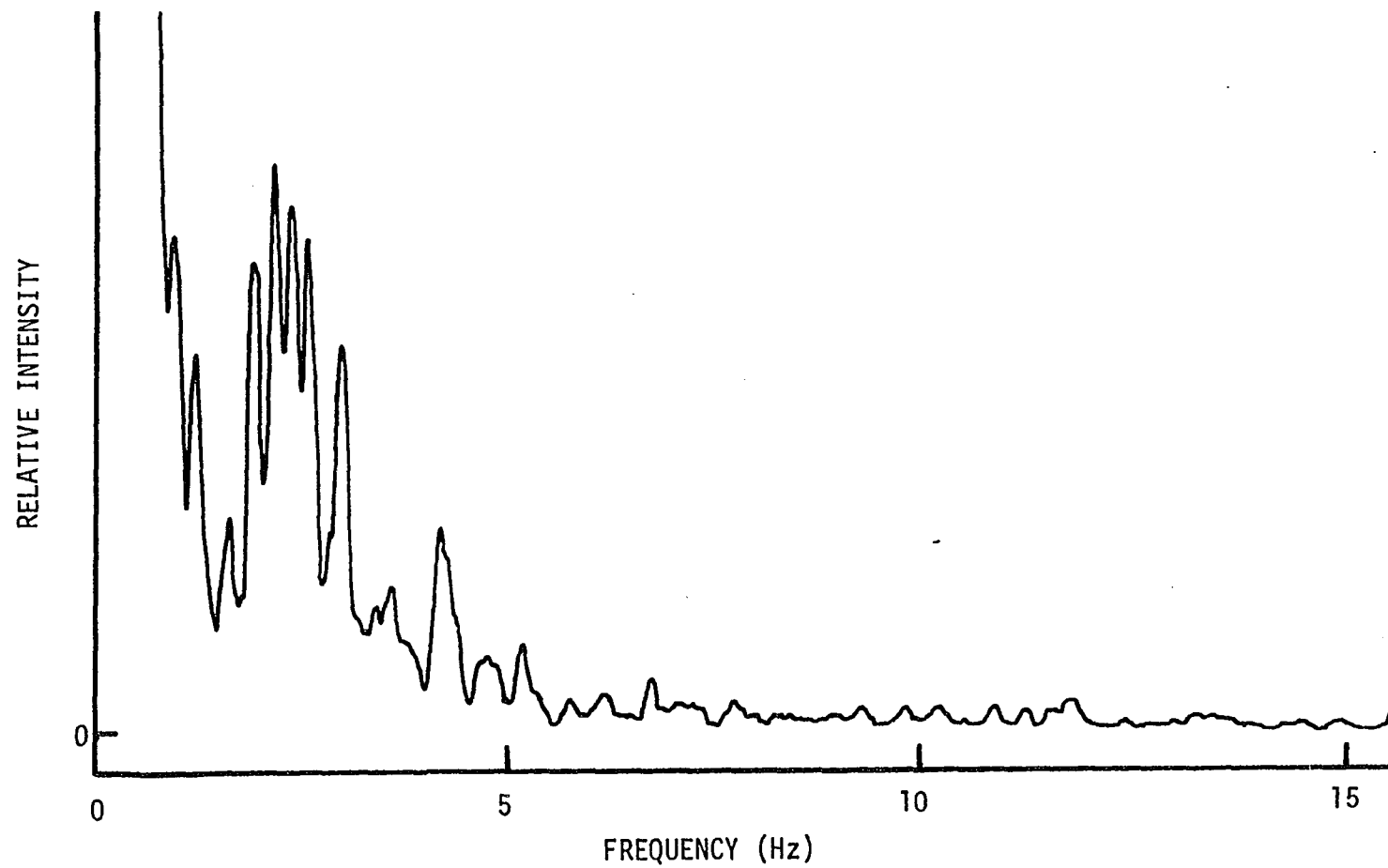
Figure 29b. Expanded plot of the spectral profile given in Figure 29a.

indicates delta brain wave activity which occurs principally during deep sleep. It is recalled that this EEG signal was recorded from an anesthetized experimental animal.

Chart recorder methods

The optical configuration used to demonstrate the chart recorder area modulation techniques is shown in Figure 13. The distance, b, from the input plane to the frequency plane was 80 cm.

Figure 30a shows a photograph of the intensity distribution in the frequency plane produced by the transparency of a 15 Hz 0.8 volt peak-to-peak sinusoidal signal photographed from an area modulated strip chart record. This area modulated record was produced by the recording pen darkening the area below the single line strip chart record. Figure 30b shows the spectral profile for an 8 second segment of this sinusoidal signal.

An ECG spectral profile produced by this method is shown in Figure 31. The section of signal analyzed in this spectral profile is from approximately the same section of the ECG data record analyzed in Figure 27. It can be seen in comparing these two spectral profiles that the higher frequency components were attenuated by the chart recorder area modulation method, whereas they were accentuated by the 16 mm sound track recording system. This loss in high frequency information was produced by the thickness of the chart recorder pen.

Figure 32 shows the spectral profile for a slightly different section of the ECG signal. The transparency used in producing this profile was made by photographing the hand darkened area below a single line chart
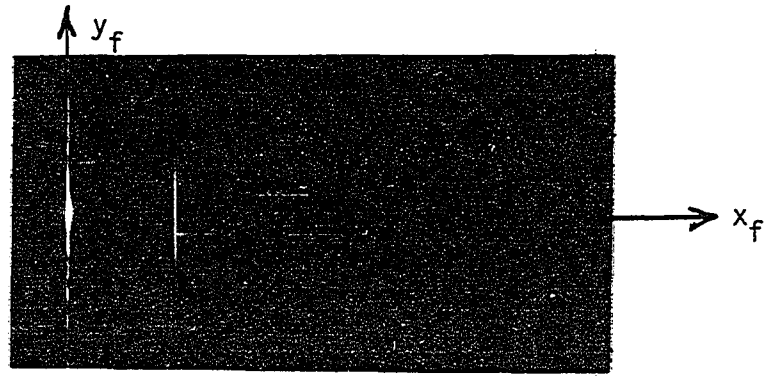
Figure 30a. Photograph of the intensity distribution in the frequency plane produced by a 15 Hz 0.8 volt peak-to-peak sinusoidal signal recorded from an area modulated strip chart record.
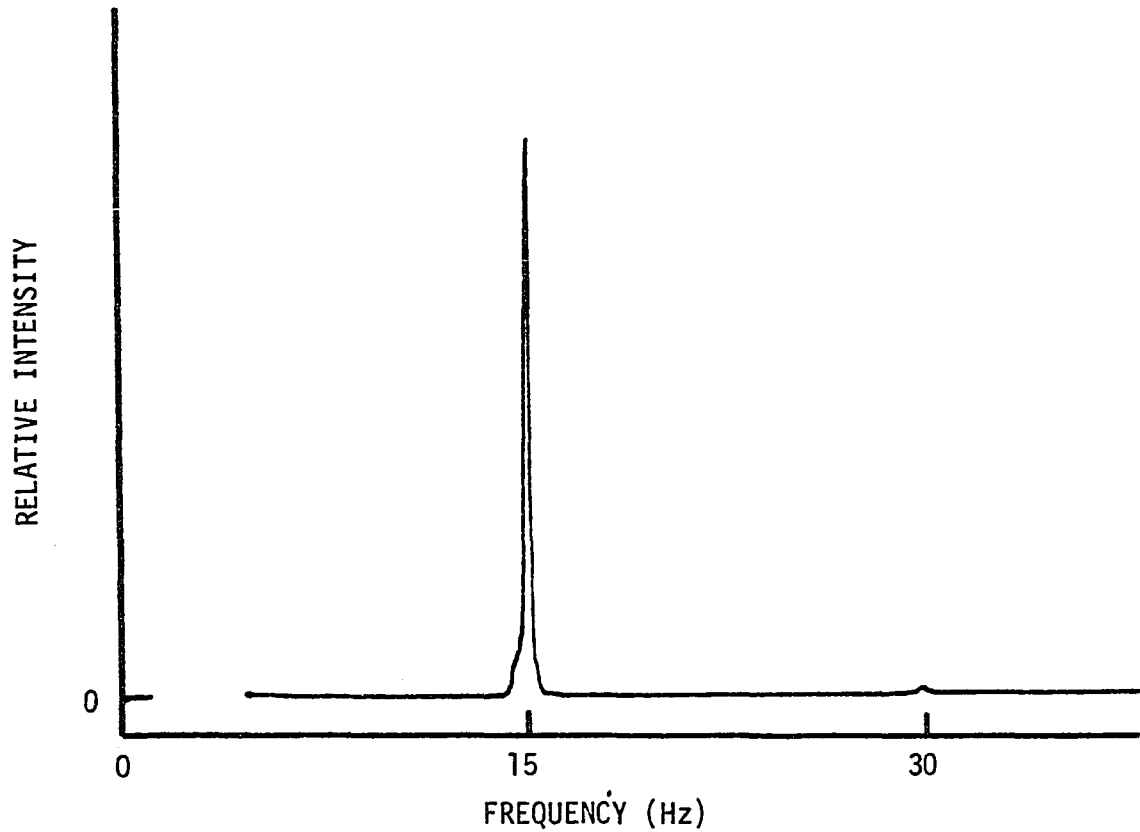

Figure 30b. The optically computed spectral profile for 8 seconds of this 15 Hz 0.8 volt peak-to-peak sinusoidal signal.
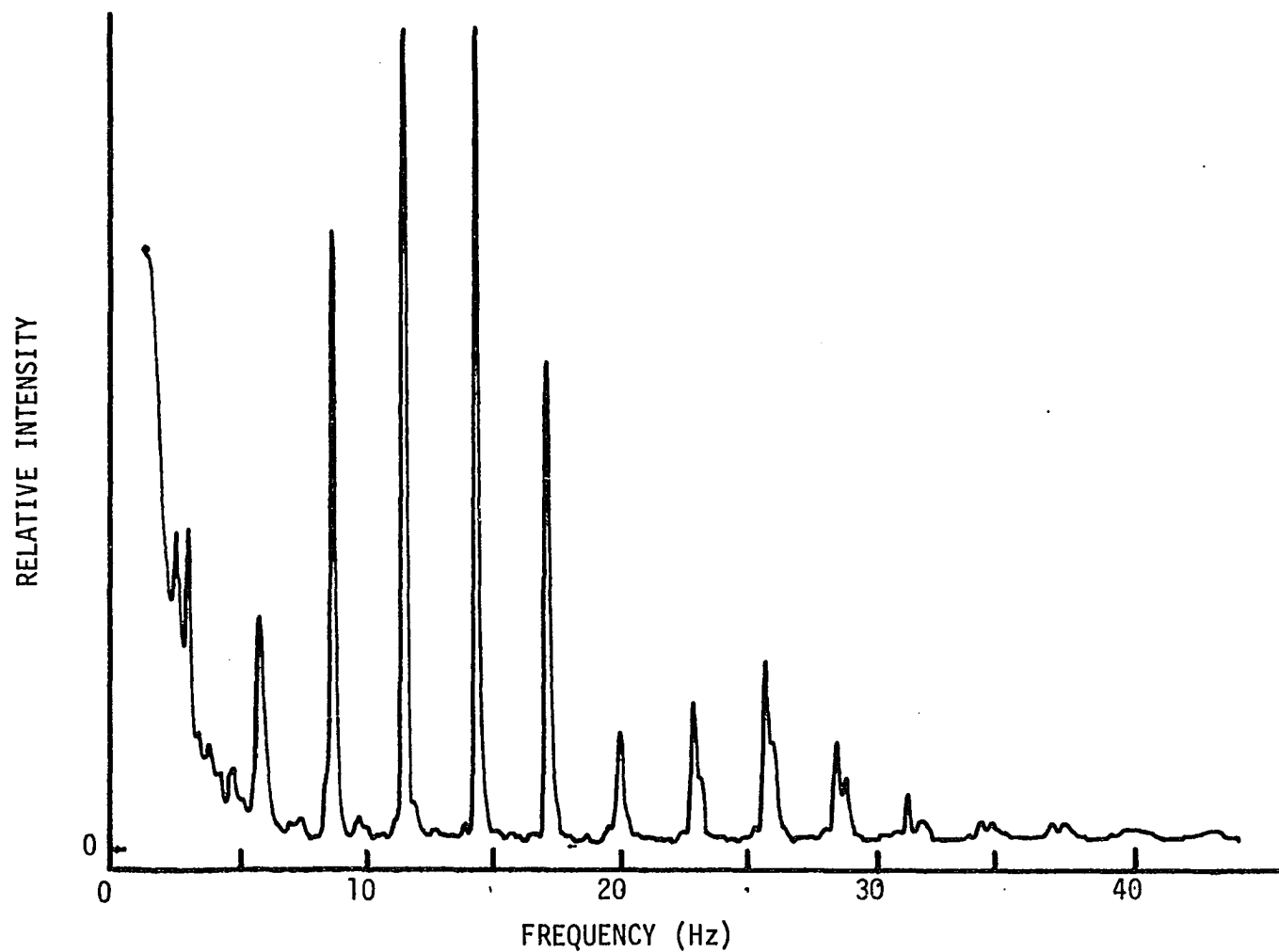
Figure 31. The optically computed spectral profile of an 8 second segment of the ECG signal transparency produced by photographing an area modulated strip chart record.
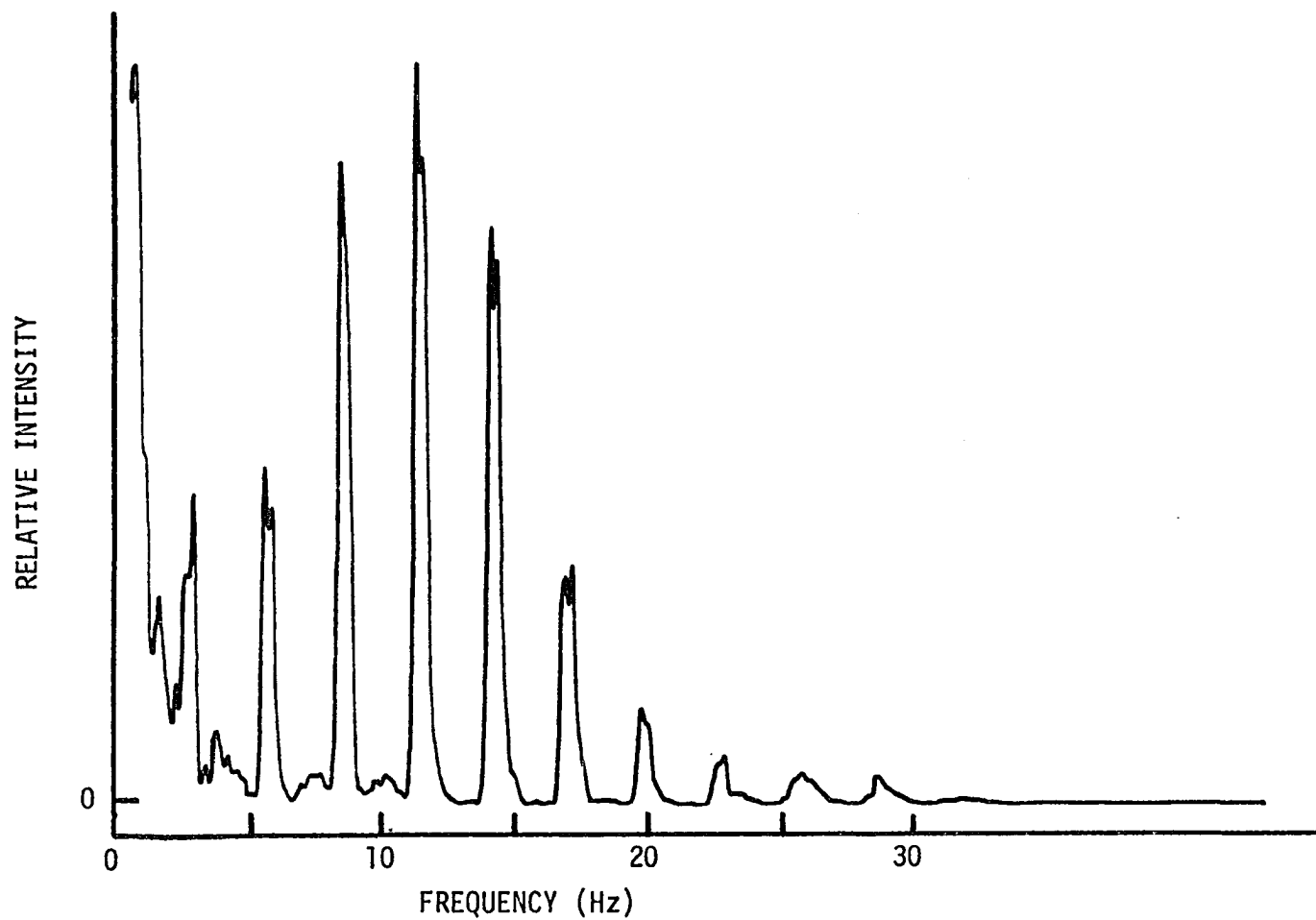
Figure 32. The optically computed spectral profile of an area modulated strip chart ECG recording achieved by hand darkening the area below a strip chart line tracing.

record of this data. It is evident from this spectral profile in comparison to the profiles shown in Figures 27 and 31 that the higher frequency components were greatly attenuated by the chart recording pen thickness and by this hand darkening technique.

Single Line Format

The optical configuration used to demonstrate the single line format is shown in Figure 13. The distance b was 80 cm.

Figure 33a shows a photograph of the intensity distribution produced by a transparency of a 15 Hz 0.8 volt peak-to-peak sinusoidal signal photographed from a single line strip chart record. The spectral profile for an 8 second segment of this signal is shown in Figure 33b. This profile was produced by moving the fiber optic cable parallel to the x_f-axis at a distance of 0.5 mm above this axis.[1] It is evident from this spectral profile and also from the photograph of the intensity distribution that the optically computed spectrum contains significant frequency components that were not present in the original time domain signal. This result does not agree with the result predicted by Equation 1-52. Furthermore, Equation 1-52 predicts a zero distribution along the $f_y = 0$ ($y_f = 0$) axis for $x_f \neq 0$, but from the photograph of this distribution shown in Figure 33a, it is evident that this was not the case.

A second example of an optically computed spectral profile for this data input format is shown in Figure 34. This profile was made by moving

---

[1] A distance of 0.5 mm in the frequency plane corresponded to a temporal frequency of approximately 1.9 Hz.
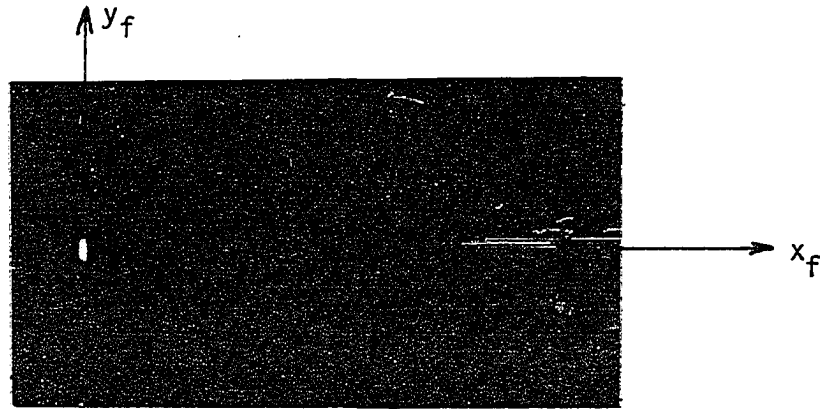
Figure 33a. Photograph of the intensity distribution in the frequency plane produced from a transparency of a 15 Hz 0.8 volt peak-to-peak sinusoidal signal photographed from a single line strip chart record.
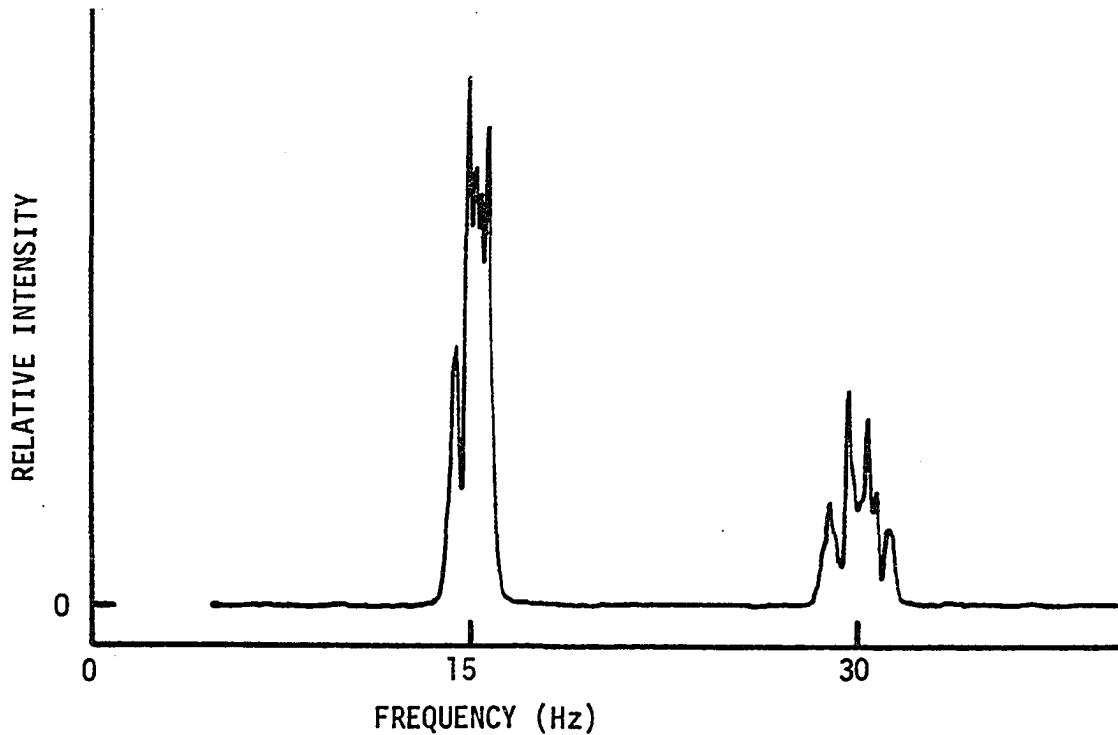

Figure 33b. The optically computed spectral profile for 8 seconds of this 15 Hz 0.8 volt peak-to-peak sinusoidal signal.
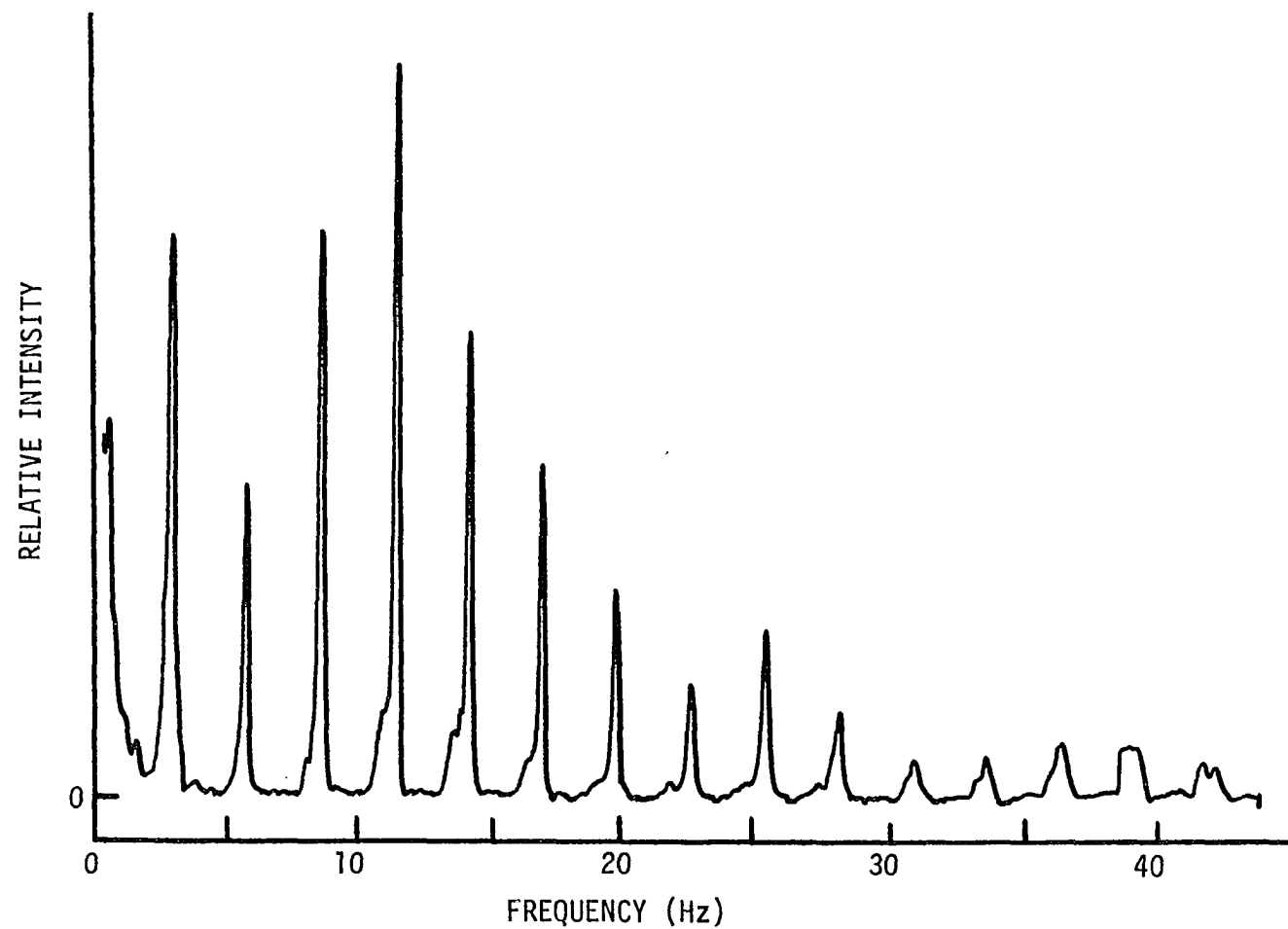
Figure 34. The optically computed spectral profile from a strip chart line tracing of an 8 second segment of the ECG signal.

the fiber optic cable parallel to the x_f-axis at a distance of 0.5 mm

above this axis. The segment of the ECG signal analyzed in this spectral

profile is from approximately the same section of the ECG signal record as

analyzed in Figures 27 and 31. Inasmuch as the ECG signal contains many

harmonic frequency terms, the error introduced by this input format is not

as evident from the ECG spectral profile as from the spectral profile for

the sinusoidal signal.

With these results, it can be stated that the assumption of a con-

stant vertical line thickness for this single line chart record is in-

valid. As a second approximation, the vertical line thickness is more

likely related to the slope of the line plus a constant term. However, a

further mathematical development using this approximation was considered

to be unnecessary inasmuch as the optically computed results were inaccu-

rate.

Density Modulation Format

The optical configuration used to process density modulated signal

transparencies is shown in Figure 13. The distance, b, from the input

plane to the frequency plane was 136 cm.

The transfer function for the density modulation format was deter-

mined as follows. Six film strips[1] containing density representations of

---

[1] In an effort to reflect slight changes that may have existed in the
film emulsion characteristics, the photographic processing chemicals,
and/or the intensity modulating system performance, these six film strips
were exposed and photographically processed at various intervals during
the recording of other density modulated signal transparencies.

sinusoidal signals[1] in the frequency range of 5 Hz to 60 Hz were used to compute this transfer function. Each of these film strips contained three separate exposures for each signal frequency. Four of the film strips contained density modulated records of 1.0 volt peak-to-peak sinusoidal signals, while the other two contained density modulated records of 0.8 volt peak-to-peak sinusoidal signals. These density modulated transparencies on each film strip were optically processed for recorded signal amplitude information. The 0.5 mm diameter single plastic fiber optic cable and the silicon photovoltaic light sensor previously described, were used to measure the relative light intensity along the x_f-axis for the fundamental frequency component of each signal. The relative light intensity measured for each of the signals on each film strip were grouped according to signal frequency and to the position relationship that signal held on that film strip. That is, whether the intensity measurement was recorded for the first, second, or third exposure at that particular frequency. The relative intensity measurements for the first frame exposures at each frequency were normalized to the first frame 10 Hz relative intensity measurement. The relative intensity measurements for the second and third frame exposures at each frequency were, respectively, normalized to the second and third frame 10 Hz relative intensity measurements. This normalizing procedure was repeated for the relative intensity measurements from each film strip. The average over the six film strips for these normalized intensity measurements at each signal frequency was computed,

---

[1]The constant bias voltage was set at 580 mv for all sinusoidal input voltages.

and these results are shown in Figure 35. The graph shown in Figure 36 is the transfer function for this density modulation format computed on a relative light amplitude basis. The relative light amplitude was determined by computing the square root of the relative light intensity measurements.

The shape of the transfer function for this data input format was a direct result of the CRT beam thickness in conjunction with the horizontal sweep rate used in recording the signals. The higher frequency signals were attenuated at this sweep rate because of the beam thickness. To extend the bandwidth of this recording technique, the sweep rate could have been increased. However, by increasing the sweep rate, the recorded information per unit film length would have decreased. Since the major frequency component for the signals being optically processed were below 50 Hz, the sweep rate used to record these signals produced adequate bandwidth characteristics for demonstrating this data input format.

Sinusoidal signals were recorded on film to determine the harmonic distortion produced by this recording format. Individual exposures were made for various amplitudes (0.2 to 1.0 volt peak-to-peak) and frequencies (5 Hz to 60 Hz). The relative light intensity at the fundamental and the harmonic frequency components were measured using the 0.5 mm diameter fiber optic cable and the silicon photovoltaic light sensor. The harmonic distortion was then computed by Equation 1.72.

A graph of the percent harmonic distortion as a function of frequency for the 1.0 volt peak-to-peak sinusoidal signals is shown in Figure 37. A graph of the percent harmonic distortion as a function of input signal amplitude for 10 Hz sinusoidal signals is shown in Figure 38. The

Figure 35. A transfer function for the density modulation format computed on a relative light intensity basis as described in the text.

Figure 36. A transfer function of the density modulation format computed on a relative light amplitude basis.
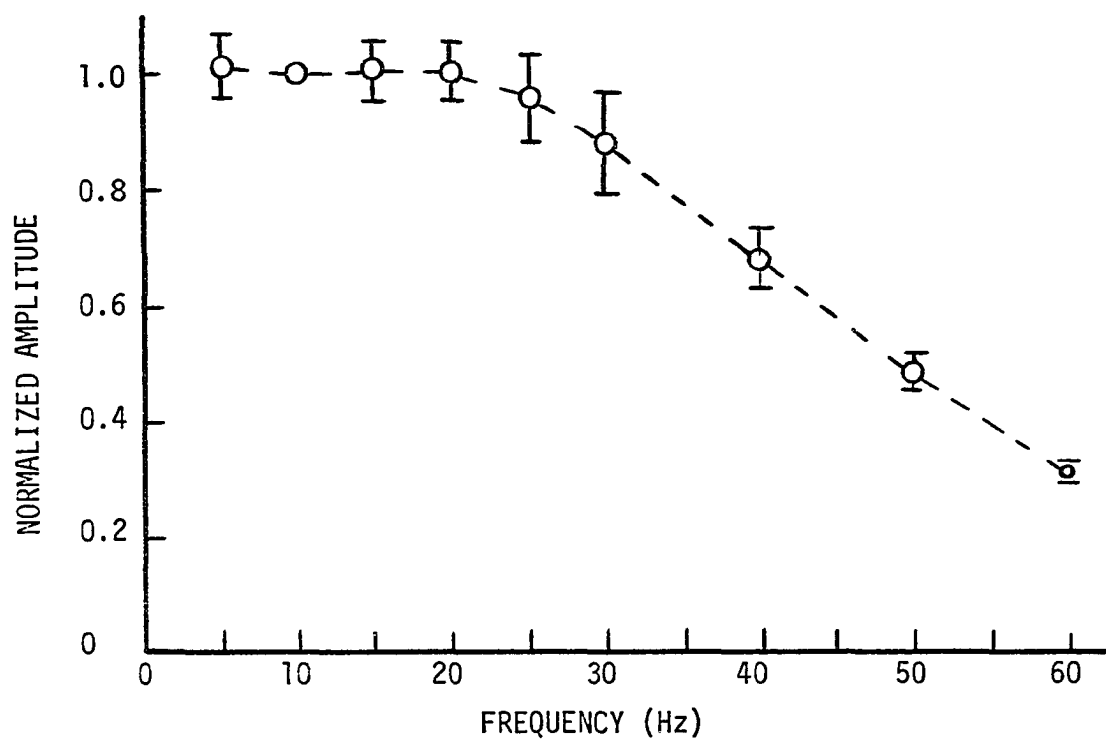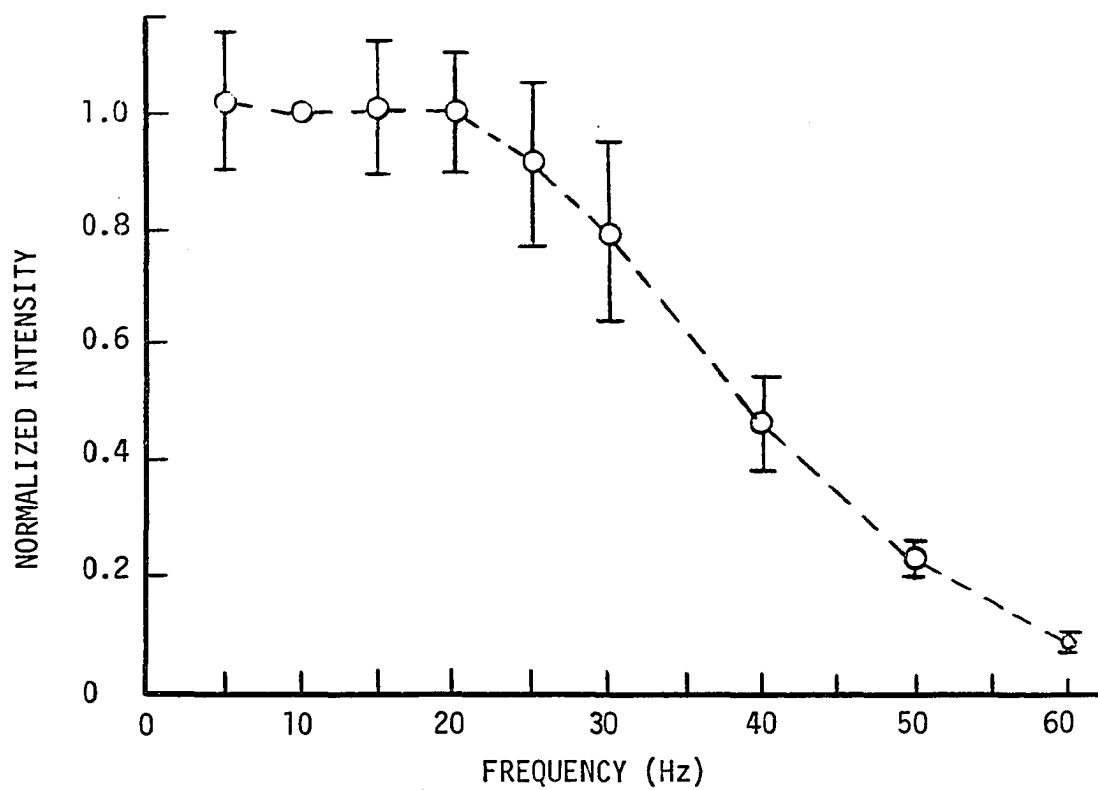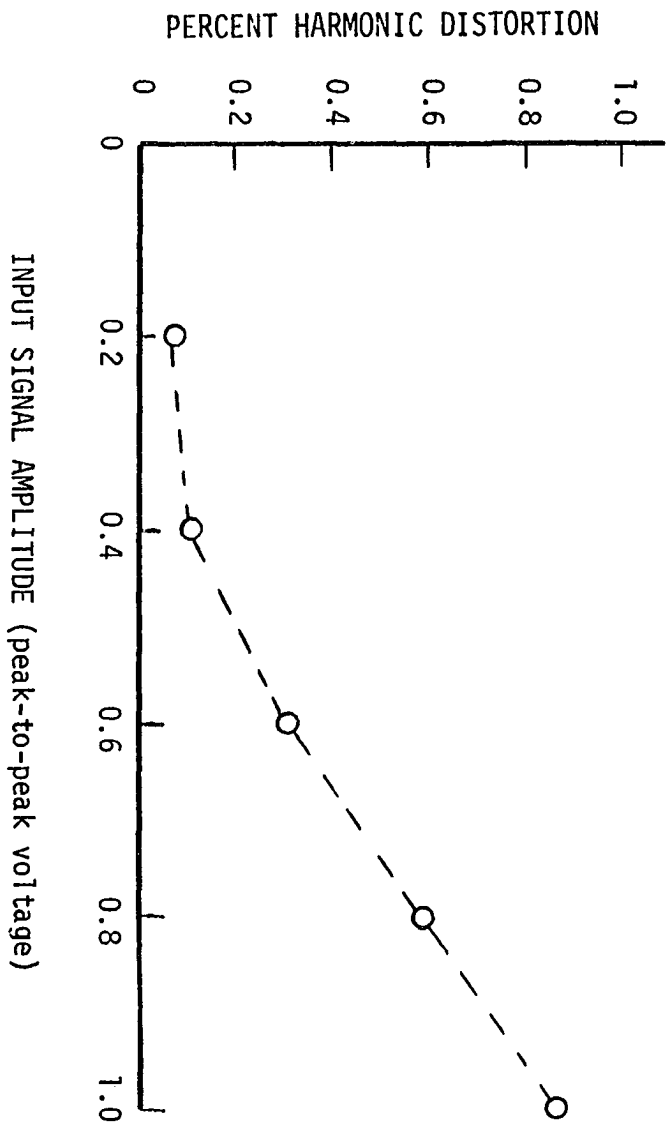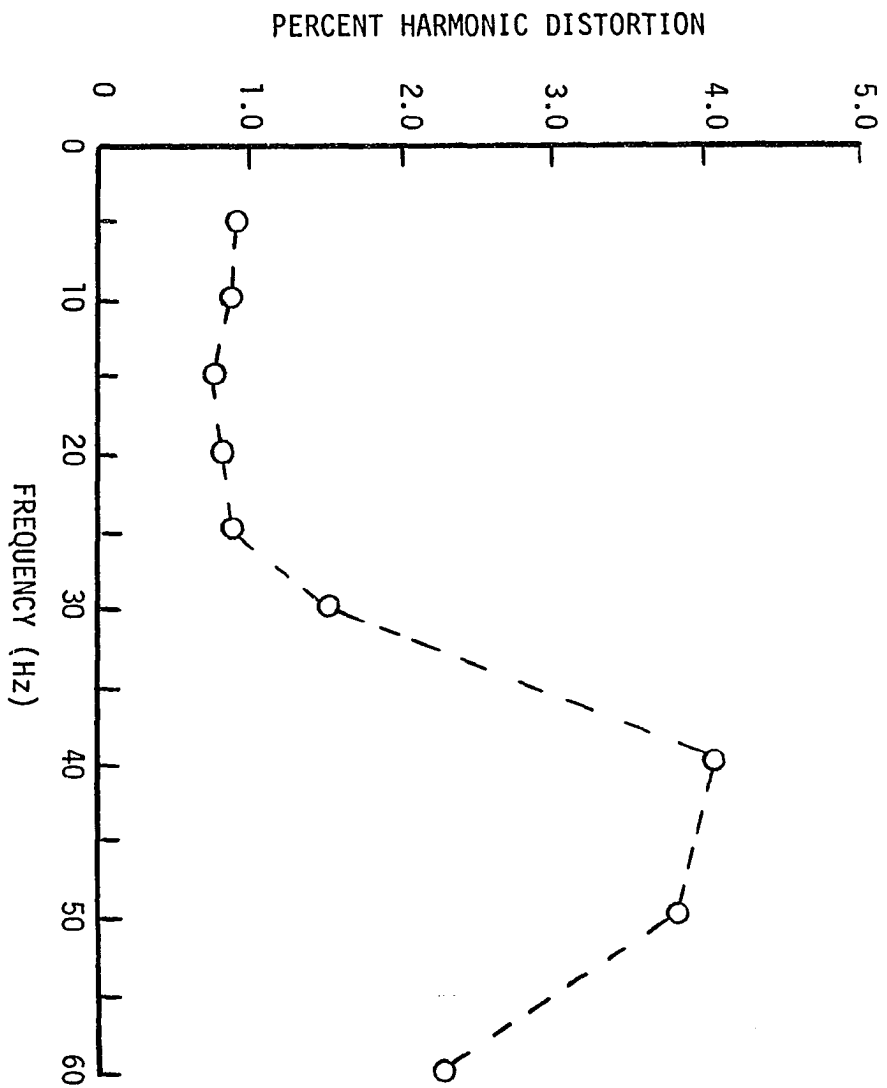
Figure 37. Percent harmonic distortion as a function of frequency for 1.0 volt peak-to-peak sinusoidal signals recorded on density modulated film transparencies.

Figure 38. Percent harmonic distortion as a function of input signal amplitude for 10 Hz sinusoidalsignals recorded on density modulated film transparencies.

increasing harmonic distortion for the higher frequency signals was due primarily to inaccurate recording of these signals as a result of the CRT beam width.

The linearity of this density modulation format was determined by recording individual exposures of various amplitude (0.2 to 1.0 volt peak-to-peak) 10 Hz sinusoidal signals on three separate film strips. The relative light intensity for the fundamental frequency component of each signal was measured, and from these measurements the relative light amplitude was computed. The computed relative light amplitude for the 1.0 volt peak-to-peak sinusoidal signal from each film strip was normalized to 1.0. Then, using the normalizing coefficient found for each film strip, the relative light amplitude measurements for the 0.2 to 0.8 volt peak-to-peak signals for each film strip were normalized. The results of this linearity test are plotted in Figure 39.

A photograph of the intensity distribution in the frequency plane for a 10 Hz 1.0 volt peak-to-peak sinusoidal signal is shown in Figure 40. It is evident from this photograph that the distribution exists predominantly along the x_f-axis. The density modulated transparency used to produce this intensity distribution was rectangular. However, only a circular 1 cm diameter area of this transparency was optically processed. Thus the distribution in the frequency plane is the spectral distribution of the recorded signal convolved with spectral distribution of a circular aperture function. It is recalled from a previous discussion that the intensity spectral distribution of a circular aperture (Figure 6a) is an Airy
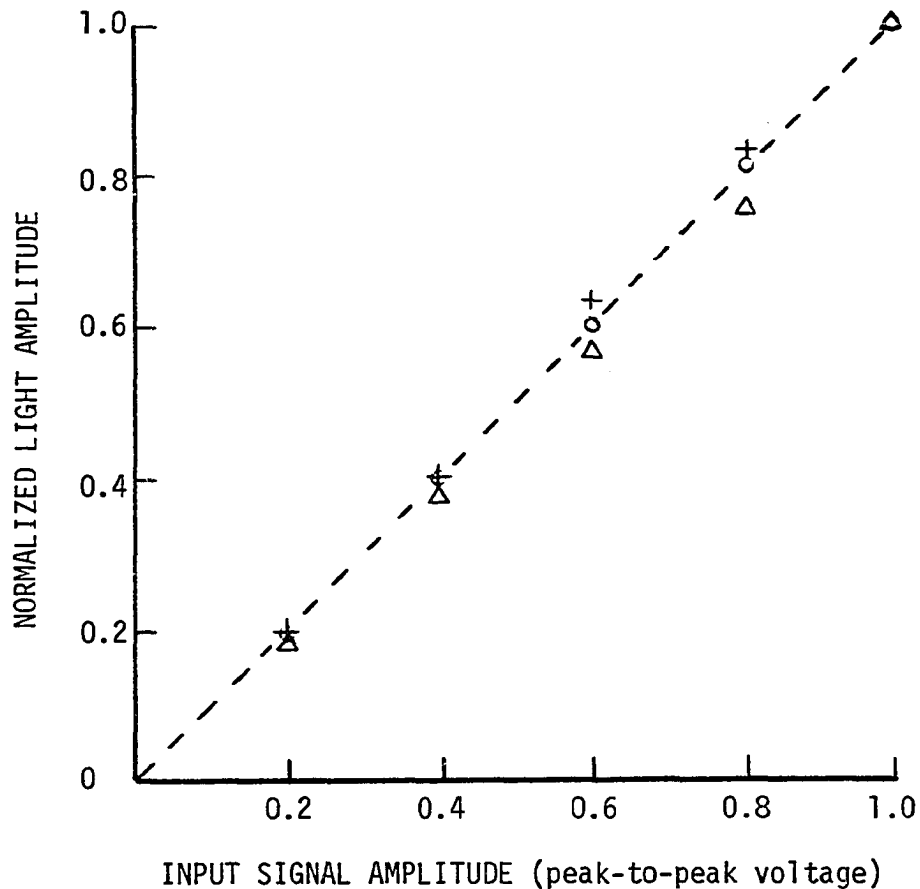
Figure 39. Linearity plot for the density modulation format using three separate film strips as described in the text.

pattern (Figure 6b). Thus around each discrete spectral point[1] in this intensity distribution of Figure 40 is an Airy pattern distribution. The deviation from being a perfectly circular Airy pattern was due to the random phase variations in the input transparency. These phase variations could be reduced by the use of a liquid gate.

---

[1]The spectral points shown in this photograph appear larger on film than they actually were because of the photograph effect of halation.
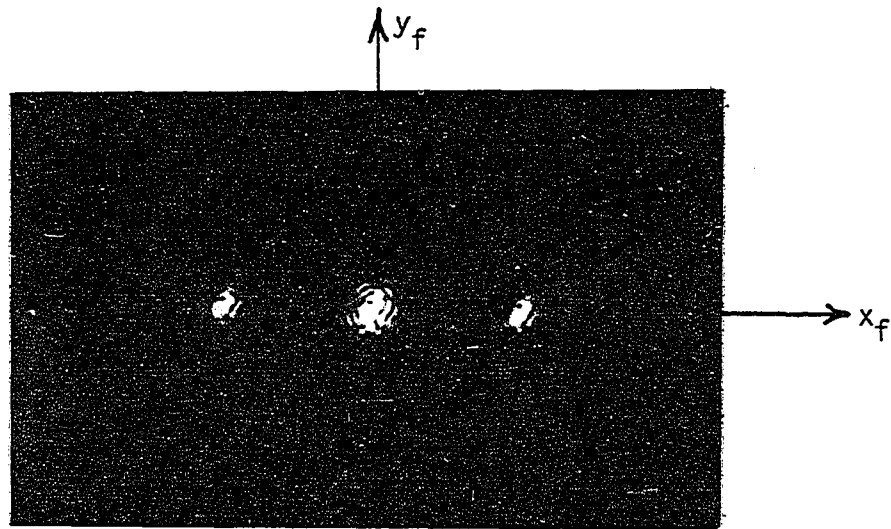
Figure 40. Photograph of the intensity distribution in the frequency
plane produced by a 2 second segment of a 10 Hz 1.0 volt
peak-to-peak sinusoidal signal recorded on a density modu-
lated transparency.

The spectral profile for this 10 Hz 1.0 volt peak-to-peak sinusoidal

signal is shown in Figure 41. This plot was produced by moving the 80

micron diameter fiber optic cable along the x_f-axis and recording the inter-

cepted light intensity as a function of distance. The frequency scale on

this profile was determined by locating both the zero frequency spectral

point and 60 Hz spectral point. This 60 Hz spectral point was produced by

the inherent 60 Hz intensity modulation of the CRT beam that was unavoid-

ably but conveniently also recorded on the density modulated transparency.

The spectral profile and intensity distribution for a 15 Hz 1.0 volt

peak-to-peak sinusoidal signal are shown in Figure 42. It is seen from

this spectral profile, in comparison to the spectral profiles shown in

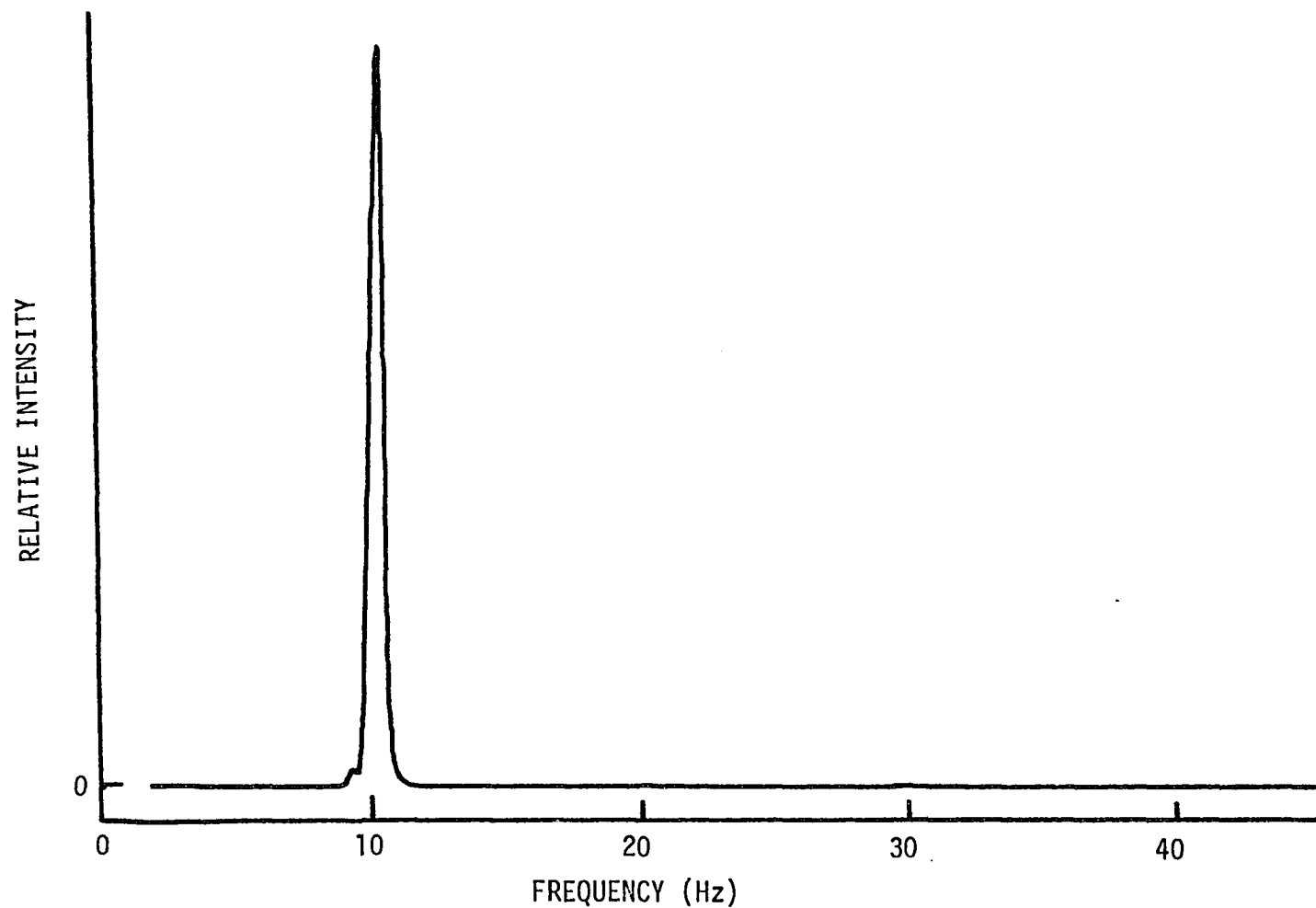Figures 26b, 30b, and 33b, that there was less harmonic distortion intro-

Figure 41. The optically computed spectral profile for a 2 second segment of a 10 Hz 1.0 volt peak-to-peak sinusoidal signal recorded on a density modulated transparency.
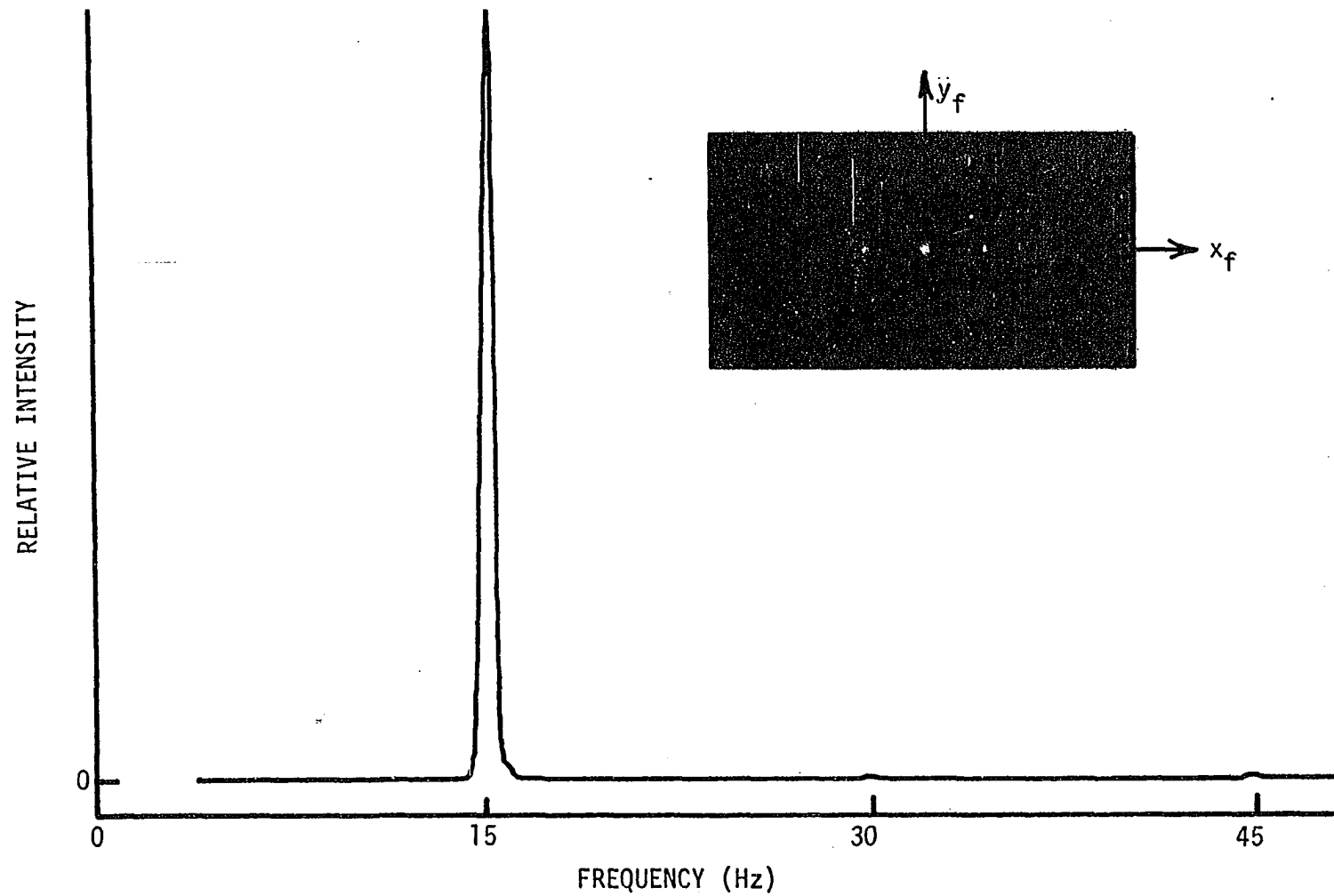
Figure 42. The optically computed spectral profile for a 2 second segment of a 15 Hz 1.0 volt peak-to-peak sinusoidal signal recorded on a density modulated transparency. The insert is a photograph of the intensity distribution in the frequency plane produced by this transparency.

duced by the density modulation format than by the other data input formats previously demonstrated.

The spectral profile for a 2 second segment of a 5 Hz 0.5 volt peak-to-peak periodic square wave signal is shown in Figure 43. It is evident that there are only odd harmonic frequency terms present in this spectral profile. This result is substantiated by the Fourier series representation of a periodic square wave signal.

An ECG spectral profile produced from this data input format is given in Figure 44. The section of signal analyzed in this spectral profile is from approximately the same section of the ECG data record as that analyzed in Figures 27, 31, and 34. However, the length of the ECG signal analyzed in Figure 44 corresponded to 2 seconds of real time data. When considering this short sample length, this spectral profile result compares favorably with those shown in Figures 27 and 31. The spectral profiles shown in Figure 45 were produced from three separate transparencies of the ECG signal recorded from approximately the same section of the data record as that used in producing the spectral profile of Figure 44. The similarity of these spectral profiles indicates that the shape of the ECG signal was not changing within this approximate 2 second time interval.

A spectral profile for 4 seconds of the EEG signal is shown in Figure 46. This EEG signal was transcribed onto the density modulated transparency at twice its real time rate. This was accomplished by playing back the magnetic tape recording of the signal at twice the recorded rate. The rationale for this procedure was to transcribe more information per unit film length and to physically expand the size of the optically
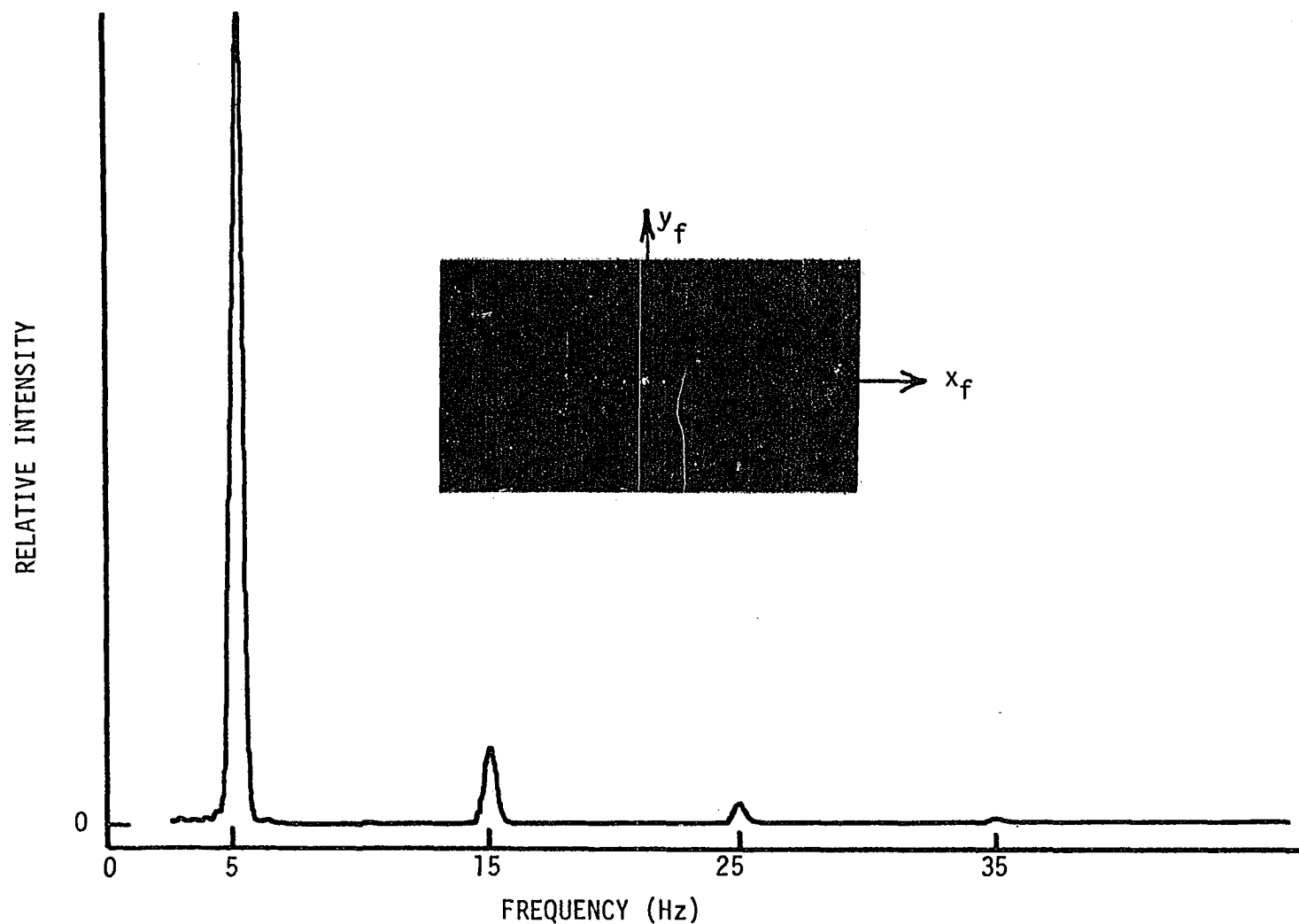
Figure 43. The optically computed spectral profile for a 2 second segment of a 5 Hz 0.5 volt peak-to-peak periodic square wave signal recorded on a density modulated transparency. The insert is a photograph of the intensity distribution in the frequency plane produced by this transparency.
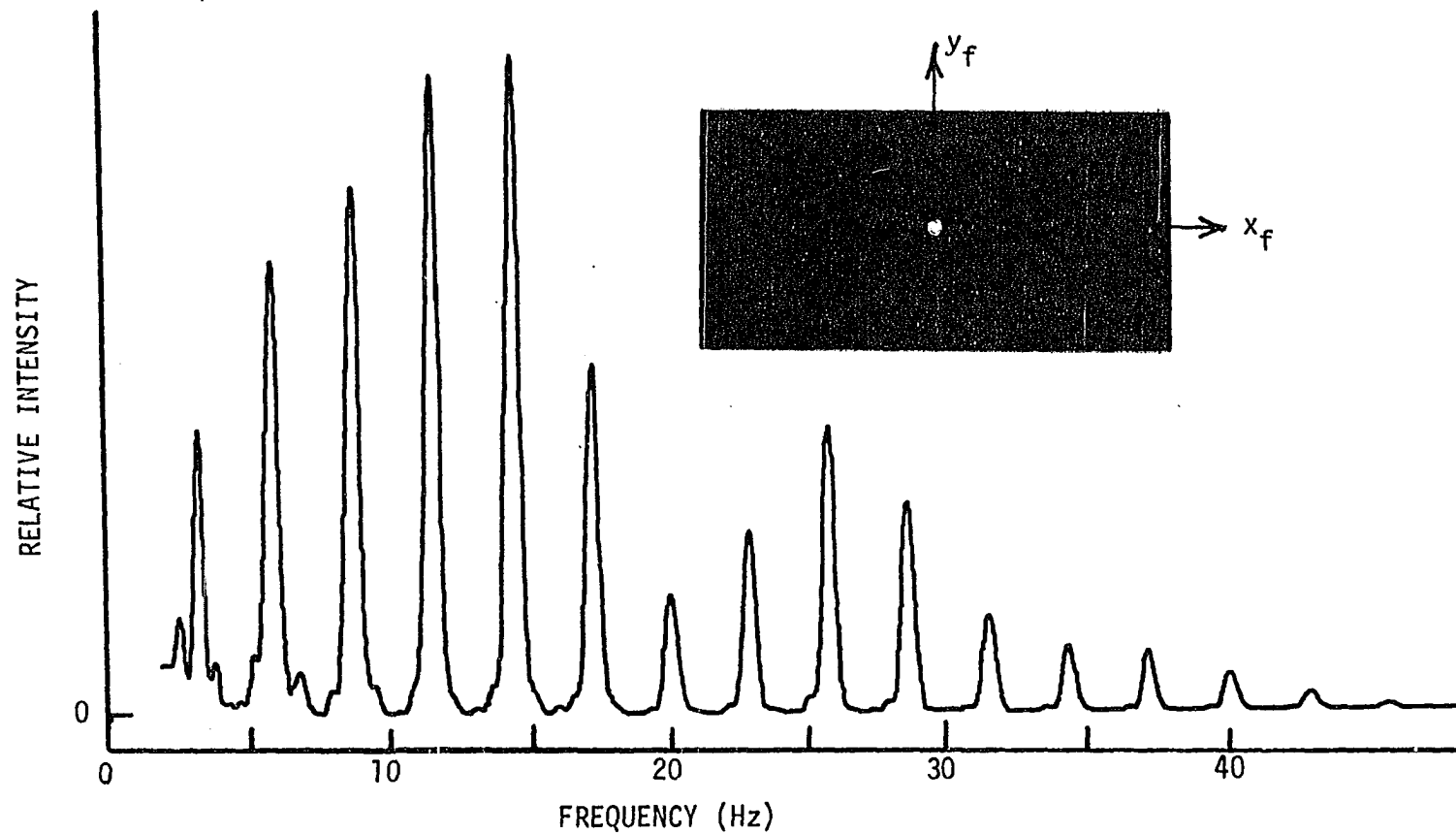
Figure 44.   The optically computed spectral profile for a 2 second segment of the ECG signal recorded on a density modulated transparency. The insert is a photograph of the intensity distribution in the frequency plane produced by this transparency.
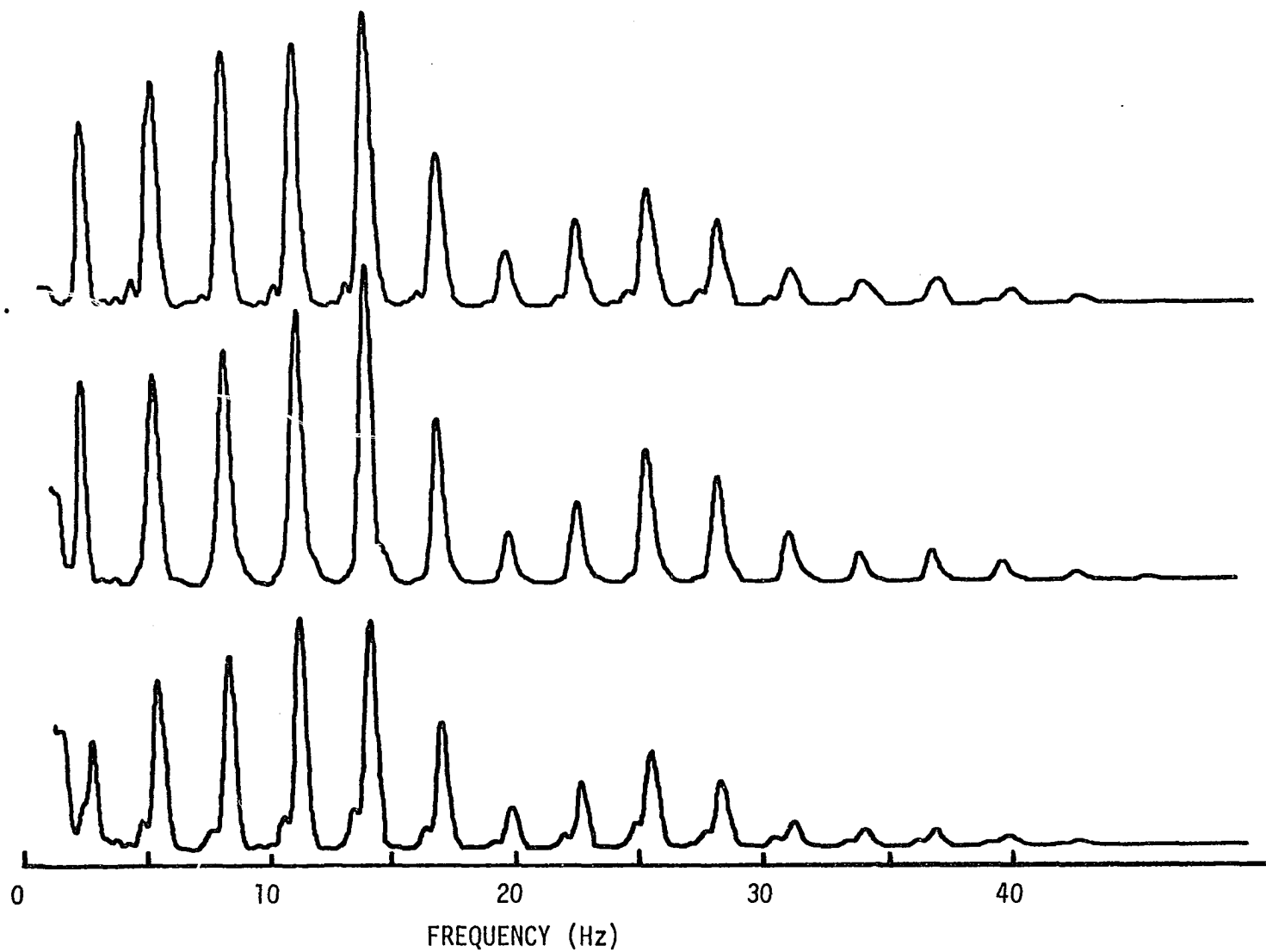
FREQUENCY (Hz)

Figure 45. The optically computed spectral profiles for 2 second segments of the ECG signal recorded on separate density modulated transparencies.
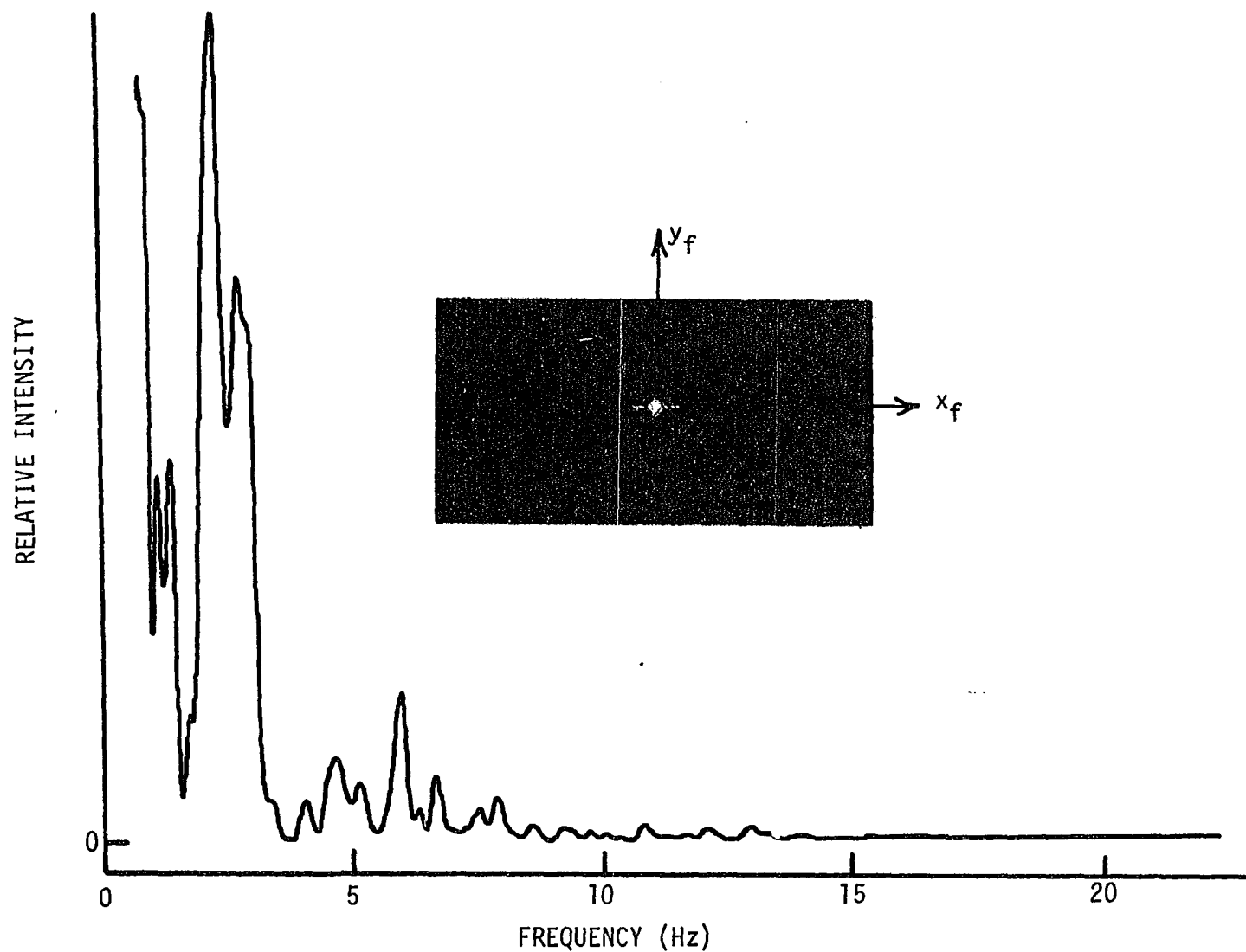
Figure 46. The optically computed spectral profile for a 4 second segment of the EEG signal recorded on a density modulated transparency. The insert is a photograph of the intensity distribution in the frequency plane produced by this transparency.

computed spectrum without increasing the distance, b, from the input plane to the frequency plane.

Figures 47 and 48 show, respectively, the spectral profiles for the normal instantaneous blood flow and instantaneous differential blood pressure waveforms. The spectral profiles for the instantaneous blood flow and instantaneous differential blood pressure waveforms recorded under the simulated stenotic condition are shown, respectively, in Figures 49 and 50. Each of these waveforms was also transcribed onto density modulated transparencies at twice the real time rate. Comparing the spectral profiles for the normal waveforms to the spectral profiles of the simulated stenosis waveforms, it is evident that an area occlusion alters the instantaneous flow and differential pressure waveforms by attenuating the higher frequency components.

Digital Computer Results

For the purpose of comparison and verification of the optically computed results, the spectral profile for a section of the ECG signal record was determined by a digital computer.[1] The section of signal analyzed by this computer was approximately the same as that analyzed optically in Figures 27, 31, and 44. Six seconds of this ECG signal were sampled at a rate of 256 samples/second. The spectral profiles for three separate blocks of 512 data points each were calculated using a discrete Fourier transform algorithm.[2] Figure 51 shows a plot of the sum of these three

---

[1]LINC-8, Digital Equipment Corp., Maynard, Massachusetts.

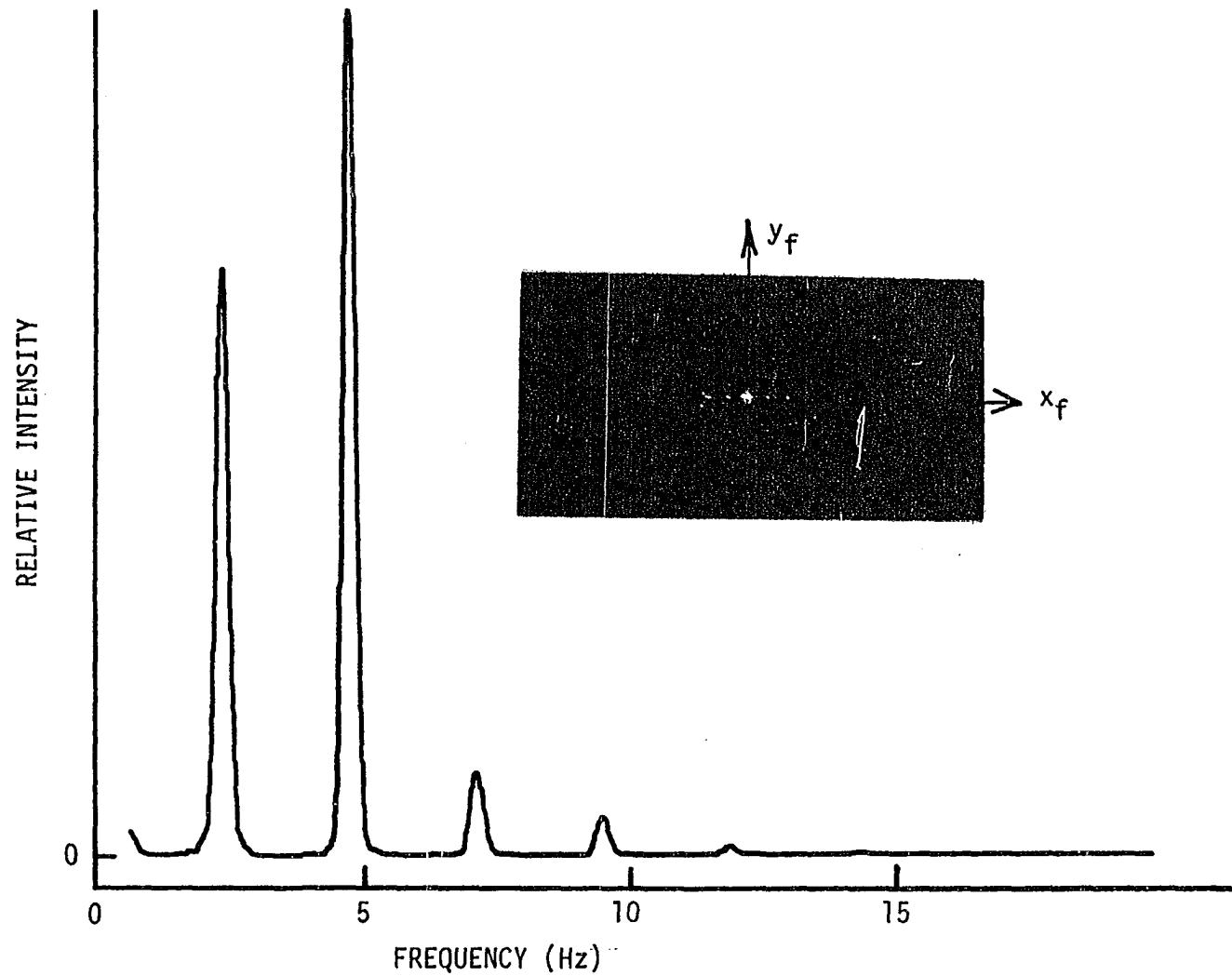[2]This program was supplied by the manufacturers of the computer.

Figure 47. The optically computed spectral profile for a 4 second segment of the normal instantaneous blood flow waveform recorded on a density modulated transparency. The insert is a photograph of the intensity distribution in the frequency plane produced by this transparency.
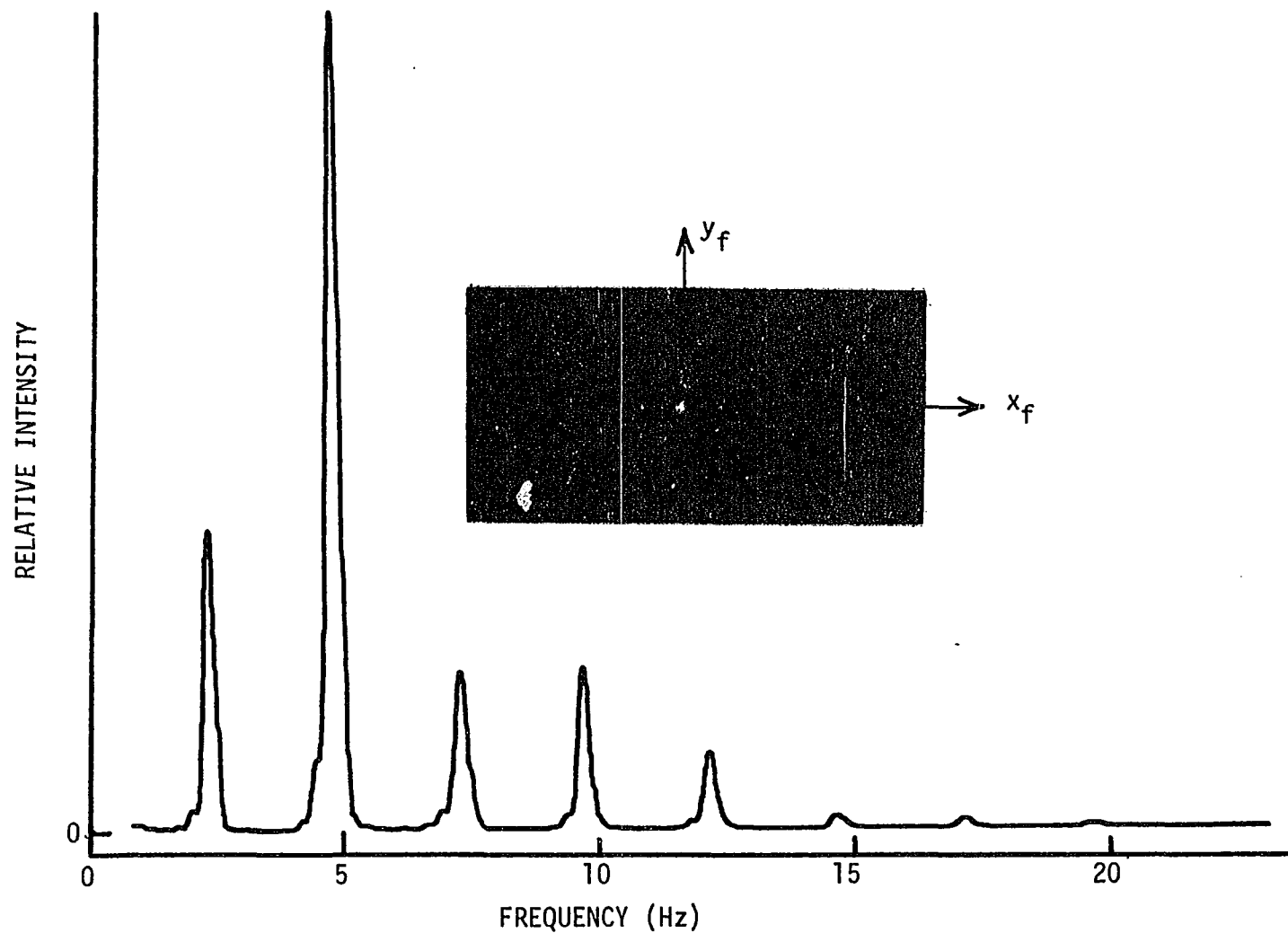
Figure 48. The optically computed spectral profile for a 4 second segment of the normal instantaneous differential blood pressure waveform recorded on a density modulated transparency. The insert is a photograph of the intensity distribution in the frequency plane produced by this transparency.
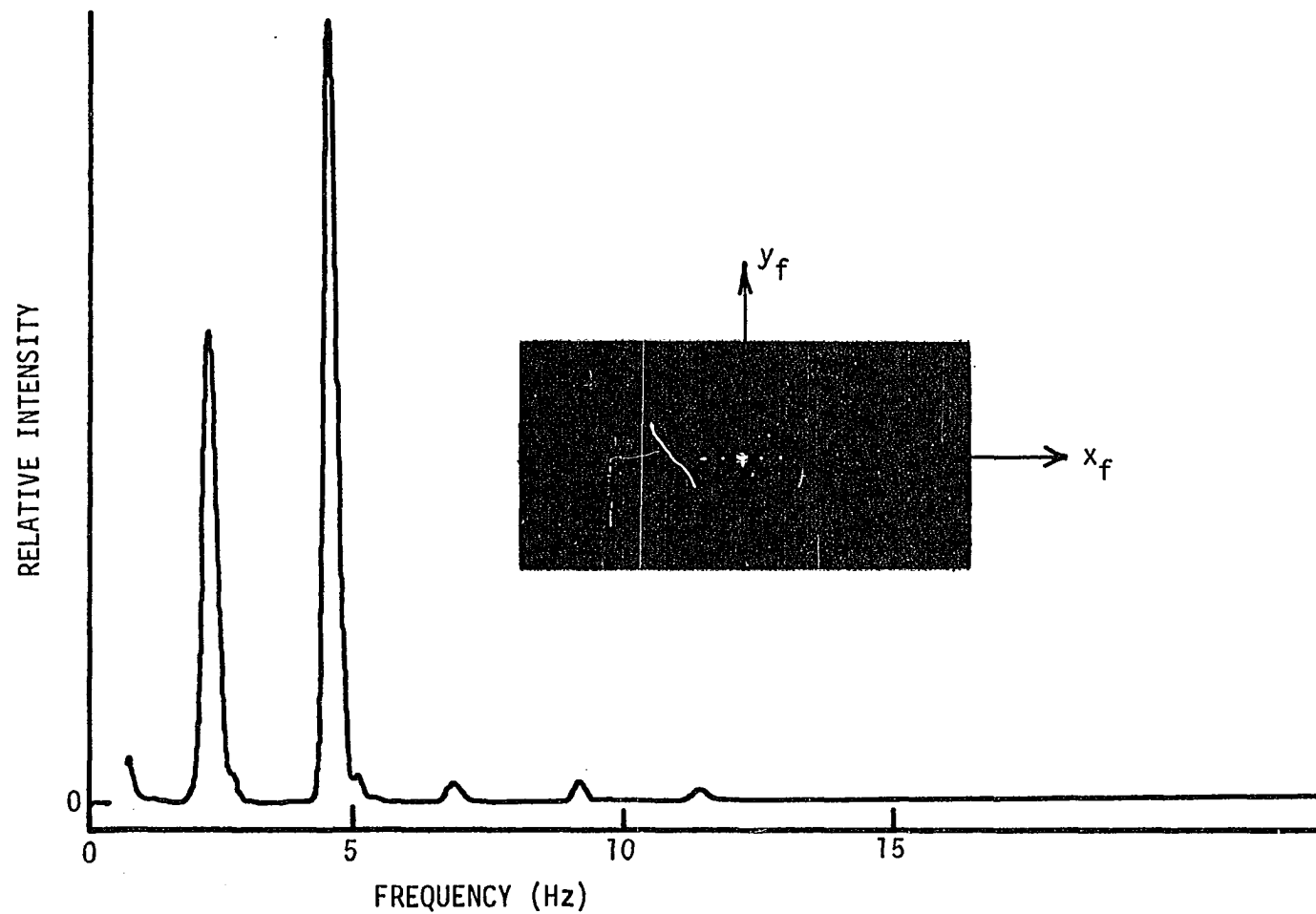
Figure 49.   The optically computed spectral profile for a 4 second segment of the instantaneous blood flow waveform for the simulated stenotic condition recorded on a density modulated transparency.   The insert is a photograph of the intensity distribution in the frequency plane produced by this transparency.

RELATIVE INTENSITY

FREQUENCY (Hz)

0   5   10   15   20

y_f

x_f

Figure 50.   The optically computed spectral profile for a 4 second segment of the instantaneous differential blood pressure waveform for the simulated stenotic conditions recorded on a density modulated transparency. The insert is a photograph of the intensity distribution in the frequency plane produced by this transparency.
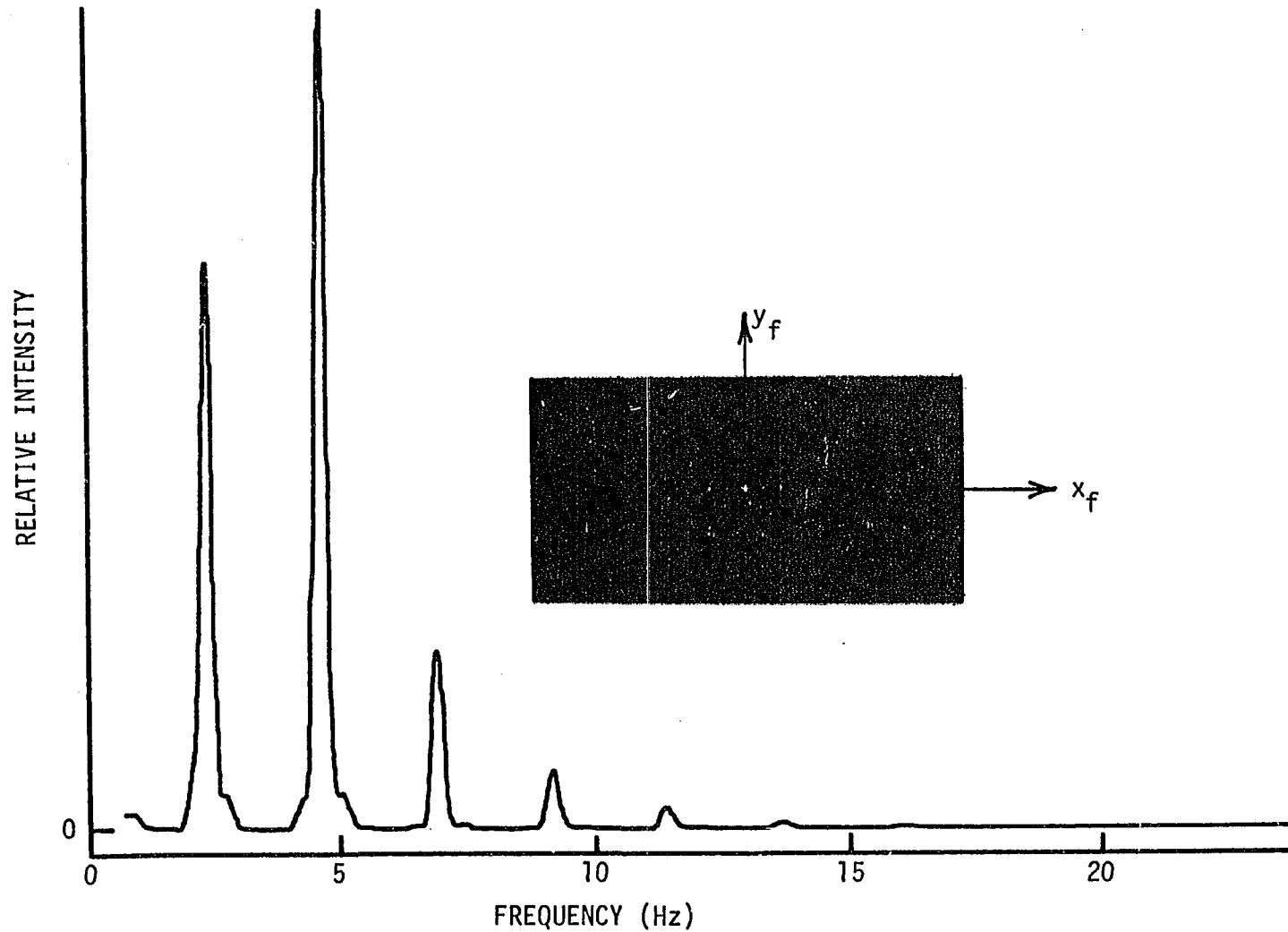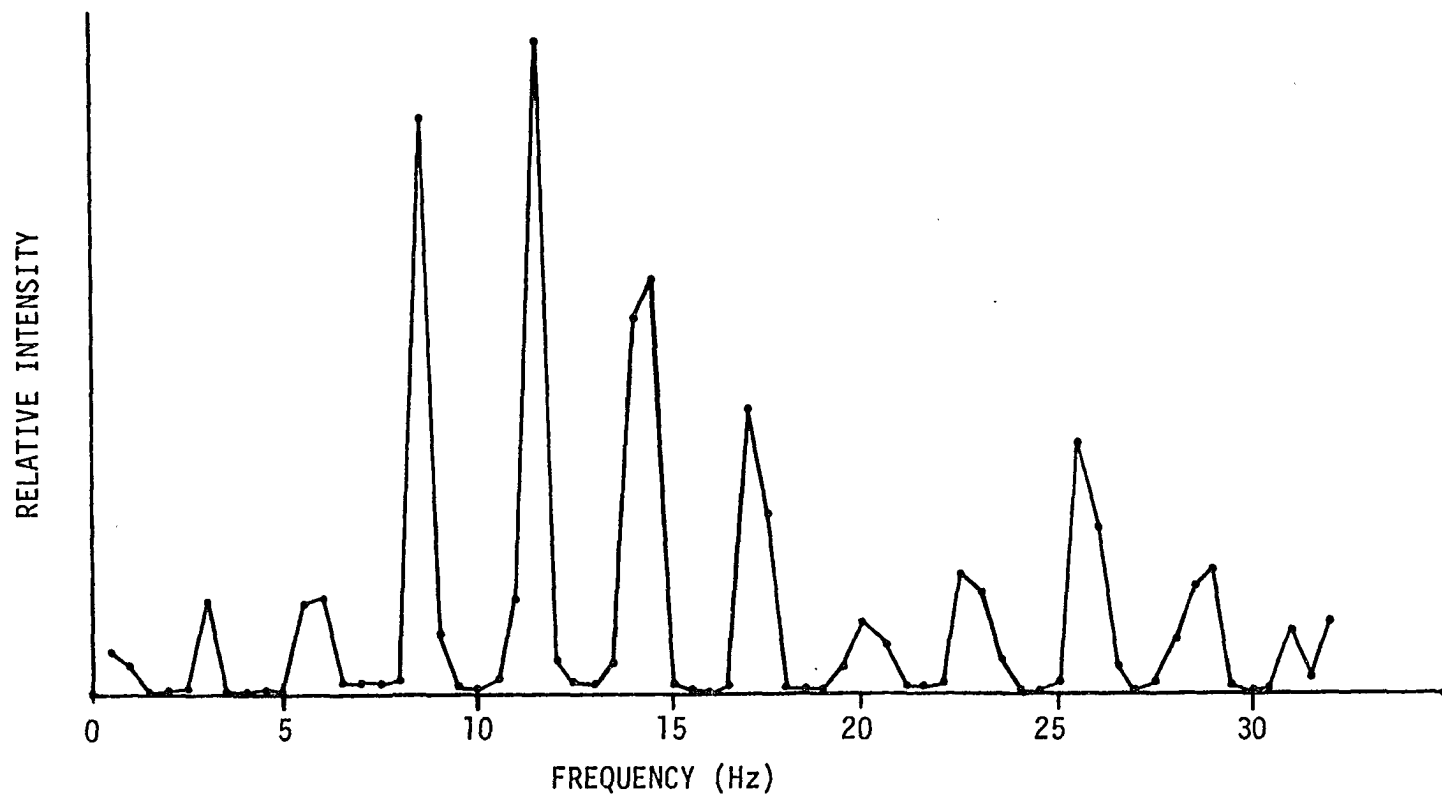
Figure 51. The computer calculated spectral profile for a 6 second segment of the ECG signal. This plot is the sum of the spectral profiles for three sequential two-second intervals sampled at a rate of 256 samples/second.

spectral profiles. It is evident, by comparing Figure 51 to Figures 27, 31, and 44, that the optically computed spectral profiles for the area modulation and density modulation formats compare favorably with this result.

CONCLUSIONS AND RECOMMENDATIONS

The mathematical analysis developed above and the experimental veri-
fications presented indicate coherent optical processing techniques can be
used to spectrally analyze real one-dimensional biological signals. Opti-
cal processing techniques do provide high resolution continuous spectral
information for low frequency signals, and such results can be produced
with an inexpensive and relatively simple optical system. Once the signal
has been recorded on film in a proper input format, almost instantaneous
accurate quantitative spectral information can be obtained for any section
of the signal record.

The major data input formats investigated in this research were area
modulation and density modulation. The area modulation format was pri-
marily demonstrated by recording signals onto 16 mm motion picture sound
track film. This recording method illustrated a technique to easily
transcribe and then optically analyze a long continuous signal record.
The photographically processed 16 mm transparency can be used to analyze a
segment of the signal record, or if analysis of the entire signal record
is desired, then contiguous sequential segments of this record can be
optically processed as was illustrated in Figure 28.

The sound track recording method used in this research does, however,
have some disadvantageous features that may warrant construction of an
alternate area modulation recording system for long continuous signal
records. It should be feasible to build a recording system that would
enable direct recording of low frequency signals, and thus eliminate the
procedure of first recording the signal on magnetic tape and then tran-

scribing onto film at a higher rate. Also, the signals could be tran-
scribed onto a finer grain film in an effort to reduce the harmonic distor-
tion in area modulation recording. Finally, this recording system should
have an equalized (flat) transfer function over the frequency bandwidth of
interest to allow convenient quantitative interpretation of the optically
computed results.

The area modulation methods using the strip chart recorder were pre-
sented in this research primarily for demonstrating alternate techniques
to area modulate a signal. These methods have distinct advantages in that
sophisticated recording equipment is not required, and also a visually
readable chart record is provided along with the ability to optically
process segments of this record. In addition, the hand darkening method
allows optically computed spectral analysis of existing chart records.
Normally such records are inaccessible to automated analysis unless curve
following devices are used to transform them into analog or digital elec-
trical signals. Biological records in particular exist in great quanti-
ties in such a relatively inconvenient form. Thus, considering these ad-
vantages, further research should be done on these methods to determine
techniques to increase the accuracy of the optically computed results. It
appears that using a finer recording pen, increasing the chart paper
speed, and increasing the signal amplitude may improve the high frequency
characteristics of this recording method. Also, photographing the area
modulated strip chart record with a Polaroid positive/negative type film[1]

---

[1]Such as Type 55 or Type 105, Polaroid Corp., Cambridge,
Massachusetts.

would reduce the film processing time, and thus make this an attractive technique to process segments of a signal record.

The single line input format investigated in this research did not yield accurate results because the vertical line thickness of the chart record was not constant. However, by developing a recording pen with characteristics better approximating this requirement, this recording format does appear to have the possibility of producing results that may be sufficiently accurate to be useful in some processing situations.

Each of the area modulation recording techniques and the single line input format, discussed above, share the common advantage of insensitivity to film exposure and processing since only a binary transmittance is required. In contrast to the transparencies obtained by these recording methods, density modulated transparencies are much more difficult to produce because of critical film exposure and processing requirements. However, this effort has its rewards in that reduced harmonic distortion in the signal transparencies can be realized, and more importantly an approximate one-dimensional optical Fourier transform can be produced. This latter characteristic will be extensively applied in a processing technique to be developed in Part II of this dissertation.

The primary reason for using an intensity modulated CRT beam to produce density modulated transparencies was because of its availability. This technique produced adequate results, however, a more sophisticated film density modulating system should be built. Using an alternate intensity modulated light source that is more easily characterized and controlled would permit more accurate matching to the film exposure-density

characteristics. This would further reduce the harmonic distortion of this recording format. A much thinner light source would extend the recorded spatial frequency capability which would then enlarge the optically computed spectrum and thus increase the resolution in the frequency plane. A continuous density modulated signal record could be produced if the light source is held stationary and a constant velocity film transport system, similar to that used with 16 mm movie film, is developed.

Some changes in the detector system are also recommended. A smaller diameter fiber optic cable will increase the detector resolution. An alternate method to increase resolution would be to expand the size of the optically computed spectrum by increasing the distance, b, from the input plane to the frequency plane. However, this procedure would also decrease the intensity of the light distribution in the frequency plane. Linear and logarithmic potentiometers could be mechanically coupled to the micro-manipulator to permit convenient generation of a voltage either directly or logarithmically related to the detector position. This would allow plotting of the spectral profiles on either a linear or log frequency basis. A logarithmic amplifier could be built to permit plotting of the relative light intensity in decibles (dB). The combination of log frequency and dB would thus generate a commonly used plotting format. Finally, the entire optical processing system could be automated to sequentially move the input transparency and the output plot to produce spectrogram plots similar to that shown in Figure 28.

It should be noted that the phase variation in the input transparencies did not present a great problem in optically processing these transparencies. Accurate spectral results were obtained for the purposes

of this dissertation without resorting to a liquid gate to remove these phase variations. However, a liquid gate should be used particularly if calibrated relative intensity measurements are required.

The major drawback in applying optical processing techniques to the analysis of one-dimensional signals is the employment of conventional photographic film to produce the input transparencies. This requirement prevents real-time optical analysis. However, this situation may change in the near future with the development of electro-optical input light modulators such as that described by Casasent [30]. At the present time such an on-line image forming light modulator is expensive, extremely bulky, and limited in resolution.

The development of new dry silver photographic films[1] may improve the applications of photographic film as the input recording medium. These films are high contrast and have high resolution, but more importantly employ a thermal development process. The exposed film is processed for 15 seconds at 260°F to produce a completed transparency. In the event that such films can be incorporated into optical processing systems, then such systems will find many applications where inexpensive, nearly real-time, analog spectral analysis of signals is desirable and of sufficient accuracy for the purpose at hand.

---

[1]Such as type 7859 or 7869, Minnesota Mining and Manufacturing Company, St. Paul, Minnesota.

PART II.   TWO-DIMENSIONAL ANALYSIS

INTRODUCTION

The inherent two-dimensional parallel processing capabilities of co-herent optical systems have led to many diverse applications of optical processing. A vast majority of these applications have been concerned with spatial frequency processing of two-dimensional data such as photo-graphs. The development, by Vander Lugt [20], of a holographic technique to produce complex spatial filters has enabled the mathematical operations of convolution and correlation to be applied in the analysis of two-dimen-sional data. The implementation of these filters has further diversified the applications of optical processing. However, the application of these optical techniques to the analysis of one-dimensional data has been quite limited even though many of the advantageous properties of optical compu-tation are also applicable to the processing of such data.

The research in Part I of this dissertation was concerned with in-vestigating the frequency processing capabilities of a coherent optical system by spectrally analyzing real one-dimensional signals. In this part of the dissertation, a technique is developed and demonstrated that will employ the two-dimensional parallel processing capabilities of an optical system to simultaneously process two separate one-dimensional signal records. This technique will enable instantaneous and simultaneous spec-tral analysis of the two signal records. Also, with the implementation of a simple narrow slit spatial filter in the frequency plane, the operations of convolution and correlation of the two signal records can easily be obtained. This technique will thus negate the requirement of holograph-ically recording the frequency spectrum of one signal record prior to

optically performing the convolution and correlation operations. Inasmuch as producing a holographic spatial filter of the Vander Lugt type is a nontrivial task that is often time consuming and requires special optical equipment such as a vibration free optical bench, the slit filter technique, therefore, affords a distinct advantage for optically processing one-dimensional data.

THEORETICAL AND PRACTICAL CONSIDERATIONS

Time Domain Relationships

In this section, only a special class of functions and some of their associated properties and relationships will be considered. It will be assumed that the one-dimensional function g(t) is real, nonrandom[1], and contains a finite number of discontinuities over the time interval $(-\infty,\infty)$. Furthermore, it will be assumed that the integral[2]

$$\int_{-\infty}^{\infty} \left| g(t) \right| \, dt \qquad (2\text{-}1)$$

is finite.

The Fourier transform of this real one-dimensional function is given by

$$F\left\{g(t)\right\} = \underline{G}(f) = \int_{-\infty}^{\infty} g(t) \, \exp[-j2\pi ft] \, dt \qquad (2\text{-}2)$$

---

[1]The inclusion of time-stationary random functions can be made by assuming g(t) is a finite length section of a time-stationary random function g'(t) such that

$$g(t) = \begin{cases} g'(t) & \text{for } |t| \leq T/2 \\ 0 & \text{otherwise} \end{cases}$$

where T is a finite time period.

[2]For a periodic function g(t) with period T_1, it is assumed that the integral

$$\int_{-T_1/2}^{T_1/2} \left| g(t) \right| \, dt$$

is finite.

where $\underline{G}(f)$ is in general a complex function of frequency f. Inasmuch as g(t) is a real function, then from Equation 2-2

$$\underline{G}^*(f) = \int_{-\infty}^{\infty} g(t) \exp[j2\pi ft] \, dt \qquad (2\text{-}3)$$

where $\underline{G}^*(f)$ is the complex conjugate of $\underline{G}(f)$. Comparing Equations 2-2 and 2-3, it is evident that

$$\underline{G}^*(f) = \underline{G}(-f) \qquad (2\text{-}4)$$

for a real function g(t).

Consider now the real function g(-t) which is the folded (inverted about the t = 0 axis) version of g(t). The Fourier transform of g(-t) is

$$F\left\{g(-t)\right\} = \int_{-\infty}^{\infty} g(-t) \exp[-j2\pi ft] \, dt \qquad (2\text{-}5)$$

Substituting $\xi = -t$ in this equation will result in

$$F\left\{g(-t)\right\} = \int_{-\infty}^{\infty} g(\xi) \exp[j2\pi f\xi] \, d\xi$$

$$= \underline{G}(-f) \qquad (2\text{-}6)$$

Combining this result with Equation 2-4, it can then be stated for a real function g(t) that

$$\underline{G}^*(f) = \underline{G}(-f) = F\left\{g(-t)\right\} \qquad (2\text{-}7)$$

Consider at this point two real one-dimensional functions $g_1(t)$ and $g_2(t)$ with Fourier transforms given, respectively, by

$$F\left\{g_1(t)\right\} = \underline{G}_1(f) \qquad (2\text{-}8)$$

and

$$F\left\{g_2(t)\right\} = \underline{G}_2(f) \qquad (2\text{-}9)$$

An important theorem in Fourier transform theory that is used extensively

in linear system analysis is the convolution integral. The convolution of

functions $g_1(t)$ and $g_2(t)$ in the time domain is defined as

$$\rho_{12}(\tau) = g_1(t) \ast g_2(t) = \int_{-\infty}^{\infty} g_1(t)\, g_2(\tau\text{-}t)\, dt$$

$$= F^{-1}\left\{\underline{G}_1(f)\,\underline{G}_2(f)\right\} \qquad (2\text{-}10)$$

where $g_1(t) \ast g_2(t)$ is the notation used to indicate the convolution opera-

tion[1], and $F^{-1}\{\ \}$ is the shorthand notation indicating the inverse

Fourier transform[2] operation. The function $g_2(\tau\text{-}t)$ is the folded and

displaced version of $g_2(t)$ where τ is the displacement or time shifting

variable. It is evident from Equation 2-10 that the convolution of two

functions in the time domain is equivalent to multiplication of their

---

[1]The convolution of two periodic functions, $g_1(t)$ and $g_2(t)$, with the
same period T_1 is defined as

$$\rho_{12}(\tau) = g_1(t) \ast g_2(t) = \frac{1}{T_1}\int_{-T_1/2}^{T_1/2} g_1(t)\, g_2(\tau\text{-}t)\, dt$$

The convolution of two time-stationary random functions, $g_1'(t)$ and $g_2'(t)$
is defined as

$$\rho_{12}(\tau) = g_1'(t) \ast g_2'(t) = \lim_{T\to\infty}\frac{1}{T}\int_{-T/2}^{T/2} g_1'(t)\, g_2'(\tau\text{-}t)\, dt$$

[2]If $\underline{G}(f)$ is the Fourier transform of $g(t)$, then the inverse Fourier
transform of $\underline{G}(f)$ written as $F^{-1}\left\{\underline{G}(f)\right\}$ is defined by

$$F^{-1}\left\{\underline{G}(f)\right\} = \int_{-\infty}^{\infty} \underline{G}(f)\, \exp[j2\pi ft]\, df = g(t)$$

respective spectra in the frequency domain.[1] Thus, the frequency spectrum of the convolution function $\rho_{12}(\tau)$ retains the frequency components that are common to both functions.

The convolution function $\rho_{21}(\tau)$ is given by

$$\rho_{21}(\tau) = g_2(t) * g_1(t) = \int_{-\infty}^{\infty} g_2(t)\, g_1(\tau-t)\, dt$$

$$= F^{-1}\left\{\underline{G}_2(f)\, \underline{G}_1(f)\right\} \qquad (2\text{-}11)$$

where the subscript $_{21}$ indicates that the convolution involves $g_2(t)$ and $g_1(t)$. The second subscript number refers to the fact that $g_1(t)$ is the folded and displaced function. It is evident, when comparing Equations 2-10 and 2-11, that

$$\rho_{12}(\tau) = \rho_{21}(\tau) \qquad (2\text{-}12)$$

Thus, the convolution of $g_1(t)$ and $g_2(t)$ does not depend upon which function is folded and displaced.

---

[1] A similar situation exists for the convolution of the frequency spectra of two functions in that this is equivalent to multiplications of the two functions in the time domain. That is,

$$\underline{G}_1(f) * \underline{G}_2(f) = F\left\{g_1(t)\, g_2(t)\right\}$$

The crosscorrelation relationship between these two real functions is defined as[1]

$$\psi_{12}(\tau) = \int_{\infty}^{\infty} g_1(t)\, g_2(t-\tau)\, dt$$

$$= F^{-1}\left\{ \underline{G}_1(f)\, \underline{G}_2^*(f) \right\} \qquad\qquad (2\text{-}13)$$

However, since $g_2(t)$ is a real function, then

$$\psi_{12}(\tau) = F^{-1}\left\{ \underline{G}_1(f)\, \underline{G}_2(-f) \right\} \qquad\qquad (2\text{-}14)$$

Thus, the crosscorrelation of $g_1(t)$ and $g_2(t)$ in the time domain is equivalent to multiplication of spectra of $g_1(t)$ and $g_2(-t)$ in the frequency domain. Therefore, the crosscorrelation function[2] $\psi_{12}(\tau)$ also retains the frequency components that are common to both functions.

---

[1]The crosscorrelation relationship between two periodic functions, $g_1(t)$ and $g_2(t)$, with the same period T_1 is defined as

$$\psi_{12}(\tau) = \frac{1}{T_1} \int_{-T_1/2}^{T_1/2} g_1(t)\, g_2(t-\tau)\, dt$$

The crosscorrelation relationship between two time-stationary random functions, $g_1'(t)$ and $g_2'(t)$, is defined as

$$\psi_{12}(\tau) = \lim_{T\to\infty} \int_{-T/2}^{T/2} g_1'(t)\, g_2'(t-\tau)\, dt$$

[2]If the two functions $g_1(t)$ and $g_2(t)$ are equal, then $\psi_{12}(\tau)$ is denoted by $\psi_{11}(\tau)$ and is called the autocorrelation function.

The crosscorrelation of $g_2(t)$ and $g_1(t)$ is

$$\psi_{21}(\tau) = \int_{-\infty}^{\infty} g_2(t) \, g_1(t-\tau) \, dt$$

$$= F^{-1}\left\{\underline{G}_2(f) \, \underline{G}_1^*(f)\right\} \qquad (2\text{-}15)$$

which is equal to

$$\psi_{21}(\tau) = F^{-1}\left\{\underline{G}_2(f) \, \underline{G}_1(-f)\right\} \qquad (2\text{-}16)$$

inasmuch as $g_1(t)$ is a real function. The subscript $_{21}$ indicates that the crosscorrelation involves $g_2(t)$ and $g_1(t)$ with the second subscript number referring to the fact that $g_1(t)$ is the displaced function. It can be shown from the definitions of $\psi_{12}(\tau)$ and $\psi_{21}(\tau)$ given, respectively, in Equations 2-13 and 2-15, that

$$\psi_{12}(\tau) = \psi_{21}(-\tau) \qquad (2\text{-}17)$$

This implies that a graphical plot of $\psi_{12}(\tau)$ is the same as $\psi_{21}(\tau)$ when it is folded about the vertical axis at $\tau = 0$.

There is a strong resemblance between the convolution integral, Equation 2-10, and the crosscorrelation integral, Equation 2-13. This similarity can be stated analytically by

$$\psi_{12}(\tau) = g_1(t) \ast g_2(-t) \qquad (2\text{-}18)$$

Thus, the crosscorrelation of $g_1(t)$ and $g_2(t)$ is the same as the convolution of $g_1(t)$ and $g_2(-t)$.

A summary of some important properties of the convolution and correlation operations for real functions $g_1(t)$ and $g_2(t)$ is given below:

1) $\rho_{12}(\tau) = \rho_{21}(\tau)$ \hspace{2cm} (2-19)

2) $\rho_{12}(\tau) = \rho_{12}(-\tau)$, if $g_1(t)$ and $g_2(t)$ are both even functions

$$(2\text{-}20)$$

3) $\psi_{12}(\tau) = \psi_{21}(-\tau)$ (2-21)

4) $\psi_{12}(\tau) = \rho_{12}(\tau)$, if $g_2(t)$ is an even function   (2-22)

5) $\psi_{21}(\tau) = \rho_{21}(\tau)$, if $g_1(t)$ is an even function   (2-23)

6) $\psi_{12}(\tau) = \psi_{12}(-\tau)$, if $g_1(t)$ and $g_2(t)$ are both even functions

       (2-24)

7) $\psi_{11}(\tau) = \psi_{11}(-\tau)$ (2-25)

For a more detailed discussion of convolution and correlation, the reader is referred to Lee [1] or Lathi [2].

Spatial Domain Development

In this section, the two-dimensional Fourier transform properties of a coherent optical system in conjunction with the foregoing concepts will be used in theoretically developing a technique to optically determine the convolution and the correlation functions for two one-dimensional signal records. This development will involve the optical system illustrated in Figure 52. The circular aperture with radius R_0 shown in this diagram is used to limit the dimensions of the input plane.

In the following analysis, it will be assumed that two real one-dimensional signals $g_1(t)$ and $g_2(t)$ with zero average values are transcribed at the same writing rate onto separate optical transparencies in the previously discussed density modulation format.[1] The amplitude transmittance of the first transparency is

$$t_1(x,y) = [B_1 + g_1(x)] \, rect(x/L_x) \, rect(y/L_y) \qquad (2-26)$$

---

[1] Since only finite length sections of $g_1(t)$ and $g_2(t)$ can be transcribed onto film, then in this development $g_1(t)$ and $g_2(t)$ may be time stationary random functions.
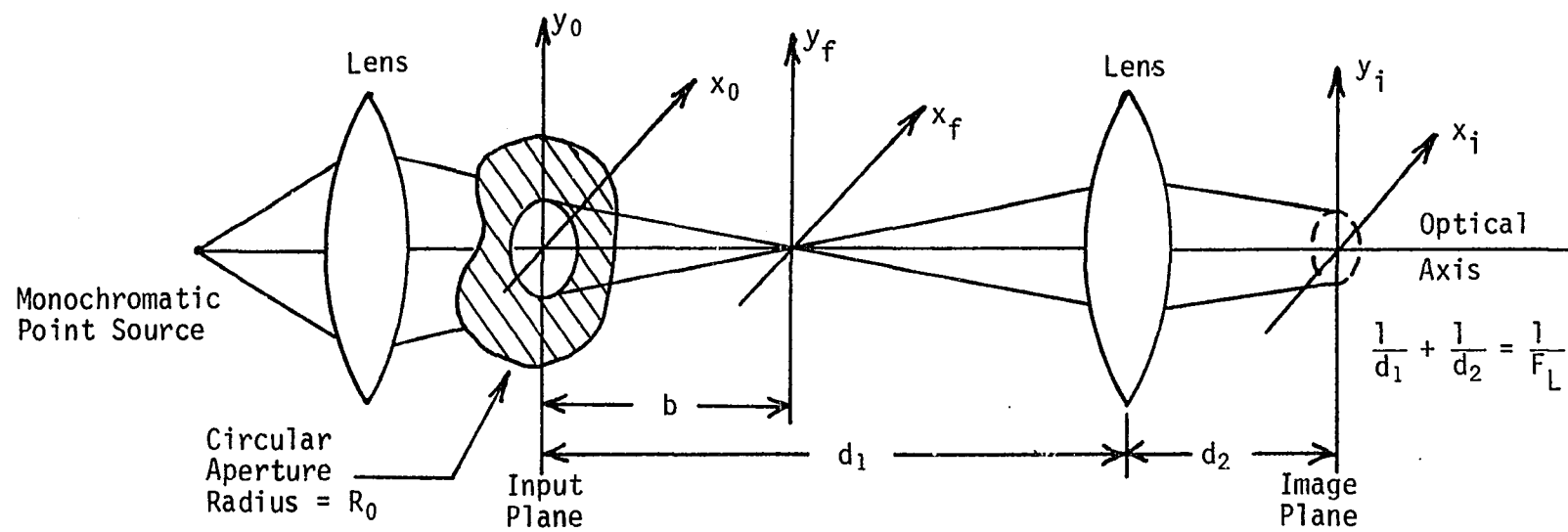
Figure 52. Optical configurations used to convolve and correlate two one-dimensional signal records.

where B_1 is a positive constant bias term and the distances L_x and L_y are, respectively, the length of the signal record in the x-direction and the width of the transparency in the y-direction. Similarly, the amplitude transmittance of the second transparency is

$$t_2(x,y) = [B_2 + g_2(x)] \, \text{rect}(x/L_x) \, \text{rect}(y/L_y) \tag{2-27}$$

If these two transparencies are optically cascaded, then the amplitude transmittance of this combination will be

$$t(x,y) = t_1(x,y) t_2(x,y) \tag{2-28}$$

However, if the second transparency is oriented along the positive y-axis such that the transmittance function $t_2(x,y)$ is now written as[1] $t_2(y,x)$, then $t(x,y)$ is given by

$$t(x,y) = t_1(x,y) t_2(y,x) \tag{2-29}$$

Placing these cascaded transparencies in the input plane of the optical system, causes the amplitude transmittance directly behind the input plane to be

$$t_0(x_0,y_0) = t(x_0,y_0) \, \text{circ}(r_0/R_0)$$
$$= t_1(x_0,y_0) t_2(y_0,x_0) \, \text{circ}(r_0/R_0) \tag{2-30}$$

where $\text{circ}(r_0/R_0)$ is a circular aperture function of radius R_0 defined as

$$\text{circ}(r_0/R_0) = \begin{cases} 1 & \text{for } r_0 = [x_0{}^2 + y_0{}^2]^{\frac{1}{2}} \leq R_0 \\ 0 & \text{otherwise} \end{cases} \tag{2-31}$$

If the radius R_0 is less than $L_x/2$ and $L_y/2$, then the transmittance function $t_0(x_0,y_0)$ is given by

---

[1] Since there is symmetry in the y-axis dimension of $t_2(x,y)$, thus $t_2(y,-x) = t_2(y,x)$.

$$t_0(x_0,y_0) = [B_1+g_1(x_0)] [B_2+g_2(y_0)] \ circ(r_0/R_0) \qquad (2\text{-}32)$$

which is

$$t_0(x_0,y_0) = [B_1B_2+B_2g_1(x_0)+B_1g_2(y_0)+g_1(x_0)g_2(y_0)] \ circ(r_0/R_0) \quad (2\text{-}33)$$

The complex light amplitude distribution in the frequency plane is, from Equation 1-21, given by

$$\underline{U}_f(x_f,y_f) = \underline{K} \ exp \left[\frac{j\pi}{\lambda b} (x_f{}^2 + y_f{}^2)\right] F \left\{t_0(x_0,y_0)\right\}$$

$$f_x = x_f/\lambda b \ , \quad f_y = y_f/\lambda b \qquad (2\text{-}34)$$

Assuming that R_0 is large, the two-dimensional Fourier transform of the circular aperture function[1] can be approximated by

$$F \left\{circ(r_0/R_0)\right\} \approx \delta(f_x,f_y) \qquad (2\text{-}35)$$

where $\delta(f_x,f_y)$ is a two-dimensional impulse function.[2]

---

[1] The Fourier transform of the circular aperture function is

$$F \left\{circ(r_0/R_0)\right\} = R_0 \frac{J_1[2\pi R_0(f_x{}^2+f_y{}^2)^{\frac{1}{2}}]}{(f_x{}^2+f_y{}^2)^{\frac{1}{2}}}$$

where J_1 is a Bessel function of the first kind, order one.

[2] The two-dimensional impulse function $\delta(f_x,f_y)$ is defined as

$$\delta(f_x,f_y) = \begin{cases} \infty & \text{for } f_x = f_y = 0 \\ 0 & \text{otherwise} \end{cases}$$

with the additional property that

$$\int_{-\varepsilon}^{\varepsilon} \delta(f_x,f_y)df_x df_y = 1 \quad \text{for any } \varepsilon > 0.$$

The Fourier transform of $t_0(x_0, y_0)$ can then be approximated as[1]

$$F\left\{t_0(x_0, y_0)\right\} = [B_1 B_2 \delta(f_x, f_y) + B_2 \underline{G}_1(f_x) \delta(f_y)$$

$$+ B_1 \underline{G}_2(f_y) \delta(f_x) + \underline{G}_1(f_x) \underline{G}_2(f_y)] * \delta(f_x, f_y)$$

$$= B_1 B_2 \delta(f_x, f_y) + B_2 \underline{G}_1(f_x) \delta(f_y)$$

$$+ B_1 \underline{G}_2(f_y) \delta(f_x) + \underline{G}_1(f_x) \underline{G}_2(f_y) \qquad (2\text{-}36)$$

Inasmuch as the complex light amplitude distribution in the frequency plane is directly related to $F\left\{t_0(x_0, y_0)\right\}$, it would be instructive at this point to consider the significance of each term in Equation 2-36. The first term represents the bias or zero frequency term that exists at the origin of the frequency plane. The second term is proportional to the frequency spectrum of $g_1(x_0)$ and exists along the f_x-axis (x_f-axis). Similarly, the third term is proportional to the frequency spectrum of $g_2(y_0)$ and exists along the f_y-axis (y_f-axis). The fourth term represents the distribution of off-axis terms which is dependent upon the product of the frequency spectrums of $g_1(x_0)$ and $g_2(y_0)$. Thus, the distribution in the frequency plane contains spectral information about each individual signal, and the product of the frequency spectrums for these signals.

Consider placing in the frequency plane a spatial filter with amplitude transmittance characteristics $H\left(\dfrac{x_f}{\lambda b}, \dfrac{y_f}{\lambda b}\right)$. The light amplitude distribution immediately behind the spatial filter is, from Equation 1-40, given by

---

[1]The effect of the circular aperture function on the intensity distribution in the frequency plane is to produce a resolution limiting Airy pattern distribution around each discrete spectral point. The radius of the central maximum of the Airy pattern is 1.22 $\lambda b/2R_0$.

$$\underline{U}_f(x_f,y_f) = \underline{K} \exp\left[\frac{j\pi}{\lambda b}(x_f{}^2 + y_f{}^2)\right] H\left(\frac{x_f}{\lambda b}, \frac{y_f}{\lambda b}\right) F\left\{t_0(x_0,y_0)\right\}$$

$$f_x = x_f/\lambda b \;, \quad f_y = y_f/\lambda b \tag{2-37}$$

This is equivalent to having in the input plane an object transparency with amplitude transmittance characteristics $t_0'(x_0,y_0)$ such that

$$F\left\{t_0'(x_0,y_0)\right\} = H(f_x,f_y) F\left\{t_0(x_0,y_0)\right\} \tag{2-38}$$

which can also be written as

$$t_0'(x_0,y_0) = F^{-1}\left\{H(f_x,f_y) F\left\{t_0(x_0,y_0)\right\}\right\} \tag{2-39}$$

where $F^{-1}\{\ \}$ is the shorthand notation for the two-dimensional inverse Fourier transform.[1] Thus, $t_0'(x_0,y_0)$ represents the spatially filtered version of the transmittance function $t_0(x_0,y_0)$. Then, from Equation 1-42, the distribution in the image plane is a spatially inverted magnified image of t_0', and is given by

$$\underline{U}_i(x_i,y_i) = -\frac{d_1}{d_2} \exp\left[\frac{j2\pi}{\lambda}(d_1 + d_2)\right]$$

$$\exp\left[\frac{j\pi}{\lambda d_2}\left(1 + \frac{d_1}{d_2} - \frac{d_1{}^2}{bd_2}\right)(x_i{}^2 + y_i{}^2)\right]$$

$$t_0'\left(-\frac{d_1}{d_2}x_i, -\frac{d_1}{d_2}y_i\right) \tag{2-40}$$

providing that $H(f_x,f_y)$ does not produce any significant diffraction effects.

---

[1] If $\underline{T}_0'(f_x,f_y)$ is the Fourier transform of $t_0'(x_0,y_0)$, then the inverse Fourier transform of $\underline{T}_0'(f_x,f_y)$ written as $F^{-1}\left\{\underline{T}_0'(f_x,f_y)\right\}$ is defined as

$$F^{-1}\left\{T_0'(f_x,f_y)\right\} = \int\int_{-\infty}^{\infty} T_0'(f_x,f_y) \exp[j2\pi(f_x x_0 + f_y y_0)]\, df_x df_y$$

$$= t_0'(x_0,y_0)$$

Assume at this point, the spatial filter is a narrow rectangular aperture of length L and width W as shown in Figure 53. If this spatial
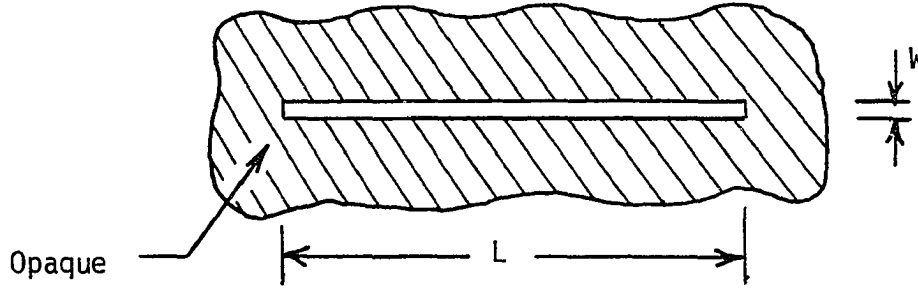

Figure 53. A narrow rectangular spatial filter.

filter is oriented symmetrically about the origin and along the f_x-axis (x_f-axis) in the frequency plane, then the amplitude transmittance of this filter can be written as

$$H(f_x, f_y) = \text{rect}(f_x/L') \ \text{rect}(f_y/W') \tag{2-41}$$

where

$$L' = L/\lambda b \tag{2-42}$$

and

$$W' = W/\lambda b \tag{2-43}$$

Thus, from Equation 2-39, $t_0'(x_0, y_0)$ is given by

$$
\begin{aligned}
t_0'(x_0, y_0) &= F^{-1}\left\{ \text{rect}(f_x/L') \ \text{rect}(f_y/W') \ F\left\{ t_0(x_0, y_0) \right\} \right\} \\
&\approx F^{-1}\left\{ \text{rect}(f_x/L') \ \text{rect}(f_y/W') \ [B_1 B_2 \delta(f_x, f_y) \right. \\
&\quad + B_2 \underline{G}_1(f_x)\delta(f_y) + B_1 \underline{G}_2(f_y)\delta(f_x) \\
&\quad \left. + \underline{G}_1(f_x)\underline{G}_2(f_y)] \right\}
\end{aligned}
\tag{2-44}
$$

Assuming that $L/2$ is larger than the spatial distribution of $\underline{G}_1(f_x)$, and W is small such that the spatial filter permits passage of only the f_x-axis distribution then Equation 2-44 can be written as

$$t_0'(x_0,y_0) = F^{-1}\left\{B_1 B_2 \delta(f_x,f_y) + B_2 \underline{G}_1(f_x)\delta(f_y)\right\} \qquad (2\text{-}45)$$

This reduces to

$$t_0'(x_0,y_0) = B_1 B_2 + B_2 g_1(x_0) = B_2[B_1 + g_1(x_0)] \qquad (2\text{-}46)$$

Thus, the spatially filtered version of $t_0(x_0,y_0)$ is proportional to the original x_0-axis input signal $B_1 + g_1(x_0)$. The distribution $\underline{U}_i(x_i,y_i)$ in the image plane is proportional to an inverted magnified version of this input signal. However, this result does not contain the finite limits on the signal length because the radius R_0 of the circular aperture was assumed to be large. It would be difficult to reinsert these limits into an exact two-dimensional representation for $t_0'(x_0,y_0)$ and also for $\underline{U}_i(x_i,y_i)$ since the form of these two-dimensional distributions are dependent upon the width W of the spatial filter in relation to the low frequency spatial components of $\underline{G}_2(f_y)$ and to the aperture radius[1] R_0. This difficulty can be obviated by evaluating t_0' just along the x_0-axis $(y_0 = 0)$. In this case, $t_0'(x_0,0)$ is given by

$$t_0'(x_0,0) = B_2[B_1 + g_1(x_0)]\ \text{rect}(x_0/2R_0) \qquad (2\text{-}47)$$

---

[1] For example, if $\underline{G}_2(f_y)$ does not contain spatial frequency components f_y below $W/2\lambda b$, and if $R_0 > 1.22\ b\lambda/W$, then

$$t_0'(x_0,y_0) = B_2[B_1 + g_1(x_0)]\ \text{circ}(r_0/R_0)$$

However, for other sets of conditions that do not fall within the limits of resolution, the exact two-dimensional form for t_0' would be much more difficult to predict.

Then the distribution in the image plane along the x_i-axis ($y_i = 0$) is

$$\underline{U}_i(x_i,0) = - \frac{B_2 d_1}{d_2} \exp\left[\frac{j2\pi}{\lambda}(d_1 + d_2)\right]$$

$$\exp\left[\frac{j\pi}{\lambda d_2}(1 + \frac{d_1}{d_2} - \frac{d_1^2}{bd_2})(x_i^2)\right]\left[B_1 + g_1(- \frac{d_1}{d_2}x_i)\right]$$

$$\text{rect}(-d_1 x_i/2d_1 R_0) \tag{2-48}$$

and this is proportional to the spatially inverted and magnified x_0-axis input signal.

Assume the spatial filter is oriented symmetrically about the origin and along the f_y-axis (y_f-axis) in the frequency plane. The amplitude transmittance is now given by

$$H(f_x,f_y) = \text{rect}(f_x/W')\,\text{rect}(f_y/L') \tag{2-49}$$

and Equation 2-44 is written as

$$t_0'(x_0,y_0) = F^{-1}\left\{\text{rect}(f_x/W')\,\text{rect}(f_y/L')\,F\left\{t_0(x_0,y_0)\right\}\right\}$$

$$= F^{-1}\left\{\text{rect}(f_x/W')\,\text{rect}(f_y/L')\,[B_1 B_2 \delta(f_x,f_y)\right.$$

$$+ B_2\underline{G}_1(f_x)\delta(f_y) + B_1\underline{G}_2(f_y)\delta(f_x)$$

$$\left.+ \underline{G}_1(f_x)\,\underline{G}_2(f_y)]\right\} \tag{2-50}$$

Assuming again that $L'/2$ is large and W' is small, then Equation 2-50 reduces to

$$t_0'(x_0,y_0) = F^{-1}\left\{B_1 B_2 \delta(f_x,f_y) + B_1\underline{G}_2(f_y)\delta(f_x)\right\} \tag{2-51}$$

which is

$$t_0'(x_0,y_0) = B_1 B_2 + B_1 g_2(y_0) \tag{2-52}$$

Along the y_0-axis ($x_0 = 0$), t_0' is given by

$$t'(0,y_0) = B_1[B_2 + g_2(y_0)]\,\text{rect}(y_0/2R_0) \tag{2-53}$$

and the distribution in the image plane along the y_i-axis ($x_i = 0$) is

$$\underline{U}_i(0,y_i) = - \frac{B_1 d_1}{d_2} \exp\left[\frac{j2\pi}{\lambda}(d_1+d_2)\right] \exp\left[\frac{j\pi}{\lambda d_2}(1 + \frac{d_1}{d_2} - \frac{d_1^2}{bd_2})(y_i^2)\right]$$

$$\left[B_2+g_2(-\frac{d_1}{d_2}y_i)\right] \text{rect}(-d_1 y_i/2 d_1 R_0) \qquad (2\text{-}54)$$

Thus, as expected, by placing the spatial filter along the f_y-axis, it is possible to recover the y-axis input signal. It should be noted that the image distributions $\underline{U}_i$ in Equations 2-48 and 2-54 each contain a quadratic phase term. However, this is of little consequence since the image is recorded as an intensity distribution, $\underline{U}_i \cdot \underline{U}_i^*$.

Consider now orienting the spatial filter symmetrically about the origin and at an angle θ from the positive f_x-axis as shown in Figure 54.
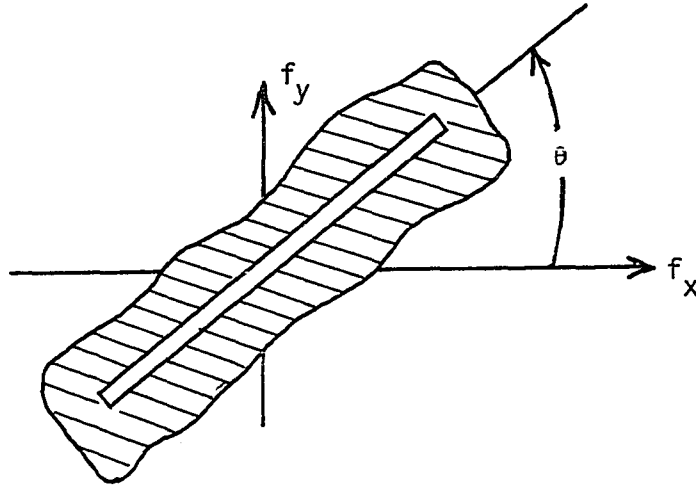
Figure 54. Orienting the spatial filter at the angle θ from the positive f_x-axis.

To reduce the complexity of the mathematical operations that follow, coordinate systems in the input, frequency, and image planes will be defined as follows:

$$x'_0 = x_0 \cos \theta + y_0 \sin \theta$$

$$y'_0 = -x_0 \sin \theta + y \cos \theta \qquad (2\text{-}55)$$

$$f'_x = f_x \cos \theta + f_y \sin \theta$$

$$f'_y = -f_x \sin \theta + f_y \cos \theta \qquad (2\text{-}56)$$

$$x'_i = x_i \cos \theta + x_i \sin \theta$$

$$y'_i = -x_i \sin \theta + y_i \cos \theta \qquad (2\text{-}57)$$

The amplitude transmittance of the spatial filter is then given by

$$H(f'_x, f'_y) = rect(f'_x/L') \ rect(f'_y/W') \qquad (2\text{-}58)$$

and Equation 2-44 can be written as

$$t'_0(x'_0, y'_0) = F^{-1}\left\{ rect(f'_x/L') \ rect(f'_y/W') \ F\left\{ t_0(x_0, y_0) \right\} \right\}$$

$$= F^{-1}\left\{ rect(f'_x/L') \ rect(f'_y/W') \ [B_1 B_2 \delta(f_x, f_y) \right.$$

$$+ B_2 \underline{G_1}(f_x)\delta(f_y) + B_1 \underline{G_2}(f_y)\delta(f_x)$$

$$\left. + \underline{G_1}(f_x) \ \underline{G_2}(f_y)] \right\} \qquad (2\text{-}59)$$

where:

$$f_x = f'_x \cos \theta - f'_y \sin \theta$$

$$f_y = f'_x \sin \theta + f'_y \cos \theta \qquad (2\text{-}60)$$

Assuming that L'/2 is large and W' is small, then Equation 2-59 reduces to

$$t'_0(x'_0, y'_0) = F^{-1}\left\{ rect(f'_y/W') \ [B_1 B_2 \delta(f'_x \cos \theta, f'_y \sin \theta) \right.$$

$$\left. + \underline{G_1}(f'_x \cos \theta) \ G_2(f'_x \sin \theta)] \right\} \qquad (2\text{-}61)$$

where assuming a small W' (W approximating the diameter of the central

maximum of the Airy pattern) eliminates the second and third terms in

Equation 2-59 and the f'_y variable in Equation 2-60. Under these assump-

tions and by applying the scaling property[1] of the Fourier transform, Equation 2-61 can be written as

$$t_0'(x_0',y_0') \simeq \frac{1}{|\cos \theta||\sin \theta|} [B_1B_2 + g_1(x_0'/\cos \theta) * g_2(x_0'/\sin \theta)] \qquad (2\text{-}62)$$

If the angle θ is positive and equal to $45°$, then the second term in Equation 2-62 is the convolution of $g_1(\sqrt{2}\, x_0')$ and $g_2(\sqrt{2}\, x_0')$. Thus, Equation 2-62 can be written as

$$t_0'(x_0',y_0') \simeq 2[B_1B_2 + g_1(\sqrt{2}\, x_0') * g_2(\sqrt{2}\, x_0')] \qquad (2\text{-}63)$$

Considering just the one-dimensional relationship $t_0'(x_0',0)$, then the finite limits on the signal length can be reinserted into this result and

$$t'(x',0) = 2[B_1B_2 + g_1(\sqrt{2}\, x_0') * g_2(\sqrt{2}\, x_0')]\, \text{rect}(x_0'/2R_0) \qquad (2\text{-}64)$$

Thus, the light amplitude distribution along the x_i'-axis ($y_i' = 0$) in the image plane is directly related to the convolution of g_1 and g_2 plus a constant term B_1B_2. This constant or zero frequency term can be optically filtered from the image distribution by placing a small opaque stop at the origin in the frequency plane. Therefore, the amplitude distribution in the image plane is directly related to the convolution of g_1 and g_2 spatially inverted (folded about the x_i'-axis) and magnified by a factor d_2/d_1.

Assume now that the angle θ is equal to $-45°$. This corresponds to positioning the spatial filter in the frequency plane as shown in Figure 55. Under these conditions, Equation 2-62 is given by

---

[1] If the Fourier transform of $g(t)$ is $\underline{G}(f)$, then the Fourier transform of $g(at)$ is $\frac{1}{|a|}\, \underline{G}(f/a)$.

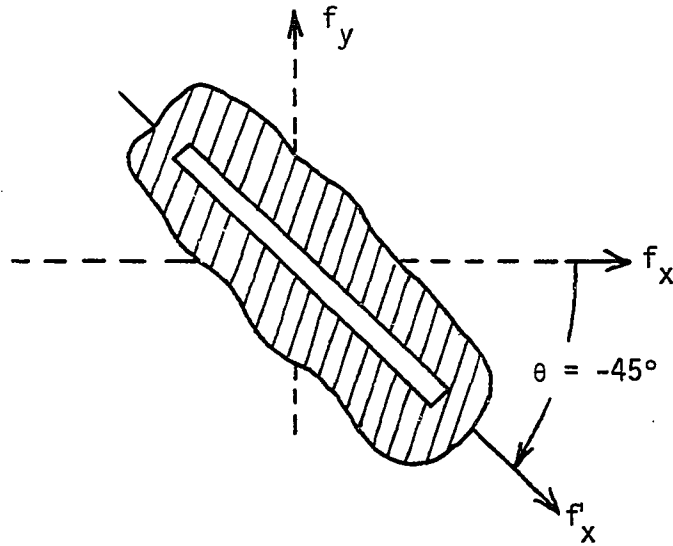Figure 55. Orienting the spatial filter at an angle θ = -45° from the positive f_x-axis.

$$t_0'(x_0',y_0') \simeq 2[B_1B_2 + g_1(\sqrt{2}\ x_0') * g_2(-\sqrt{2}\ x_0')] \qquad (2\text{-}65)$$

Considering for this case the one-dimensional relationship $t_0'(x_0',0)$, then the finite limits on the signal length can be reinserted into this result and

$$t'(x',0) = 2\ [B_1B_2 + g_1(\sqrt{2}\ x_0') * g_2(-\sqrt{2}\ x_0')]\ \text{rect}(x_0'/2R_0) \qquad (2\text{-}66)$$

Inasmuch as g_2 is a real function, the second term in this equation is the crosscorrelation of $g_1(\sqrt{2}\ x_0')$ and $g_2(\sqrt{2}\ x_0')$. The light amplitude distribution along the x_i'-axis (y_i' = 0) is directly related to the crosscorrelation of g_1 and g_2 plus a constant bias term B_1B_2.

Thus, by proper orientation of the narrow slit spatial filter, it is possible to optically determine the convolution and crosscorrelation functions for the real one-dimensional signals g_1 and g_2.

Another interesting result is possible for this optical processing technique. If the two signals $g_1(t)$ and $g_2(t)$ were initially transcribed at different writing rates, it is still possible to optically convolve and

correlate these signals by the appropriate choice of the angle θ. For example, assume that the signal $g_1(t)$ is transcribed at a writing rate α such that this signal is represented in the spatial domain by $g_1(x/\alpha)$. Also, assume that $g_2(t)$ is transcribed at a different writing rate β such that this signal is represented in the spatial domain by $g_2(x/\alpha)$. By choosing the angle θ of the spatial filter to be

$$\theta = \tan^{-1} \alpha/\beta \qquad (2\text{-}67)$$

then, if θ is positive the light amplitude distribution in the image plane along the corresponding x_i'-axis is related to the convolution of the two signals. If θ is negative, the distribution along the corresponding x_i'-axis is related to the crosscorrelation of the two signals.

In summarizing the above results, it is possible by this optical technique to simultaneously process two real one-dimensional signals. By recording the signals on separate density modulated transparencies and cascading the transparencies in a specific orientation in the input plane, then the distribution in the frequency plane contains spectral information about each individual signal and the product of the frequency spectrums for these signals. Spatially filtering this distribution using a narrow slit filter appropriately positioned in the frequency plane enables optical determination of the convolution or the correlation function for the two signals.

EXPERIMENTAL APPARATUS AND PROCEDURES

The optical system used in this part of the research is illustrated in Figure 56. The circular aperture (6 mm diameter) preceding the first lens was used to limit the area of the input plane to a circular region of approximately 1.0 cm in diameter.

The density modulated transparencies previously described in Part I of this dissertation were used as the input signal transparencies in this optical system. Single exposure transparencies were separately mounted in 35 mm slide holders.[1] Two such supported transparencies were optically cascaded and appropriately positioned in the input plane of the optical system.

The narrow slit spatial filter consisted of two double-edged razor blades separated by a distance of 0.26 mm. Each razor blade was sprayed with flat black paint to reduce surface reflections. The spatial filter was symmetrically positioned about the origin of the frequency plane and was oriented along a horizontal axis. The position of the spatial filter was held constant in the frequency plane while the input transparencies were appropriately oriented in the input plane to perform either the convolution or the correlation operation.[2] The distance, b, from the input plane to the frequency plane was 52.4 cm. At this distance and with the

---

[1] Kodak Ready-Mounts, Eastman Kodak Company, Rochester, New York.

[2] Thus, instead of rotating the spatial filter to the appropriate position in the frequency plane, the cascaded input transparencies were rotated in the input plane to the proper orientation to perform these operations.
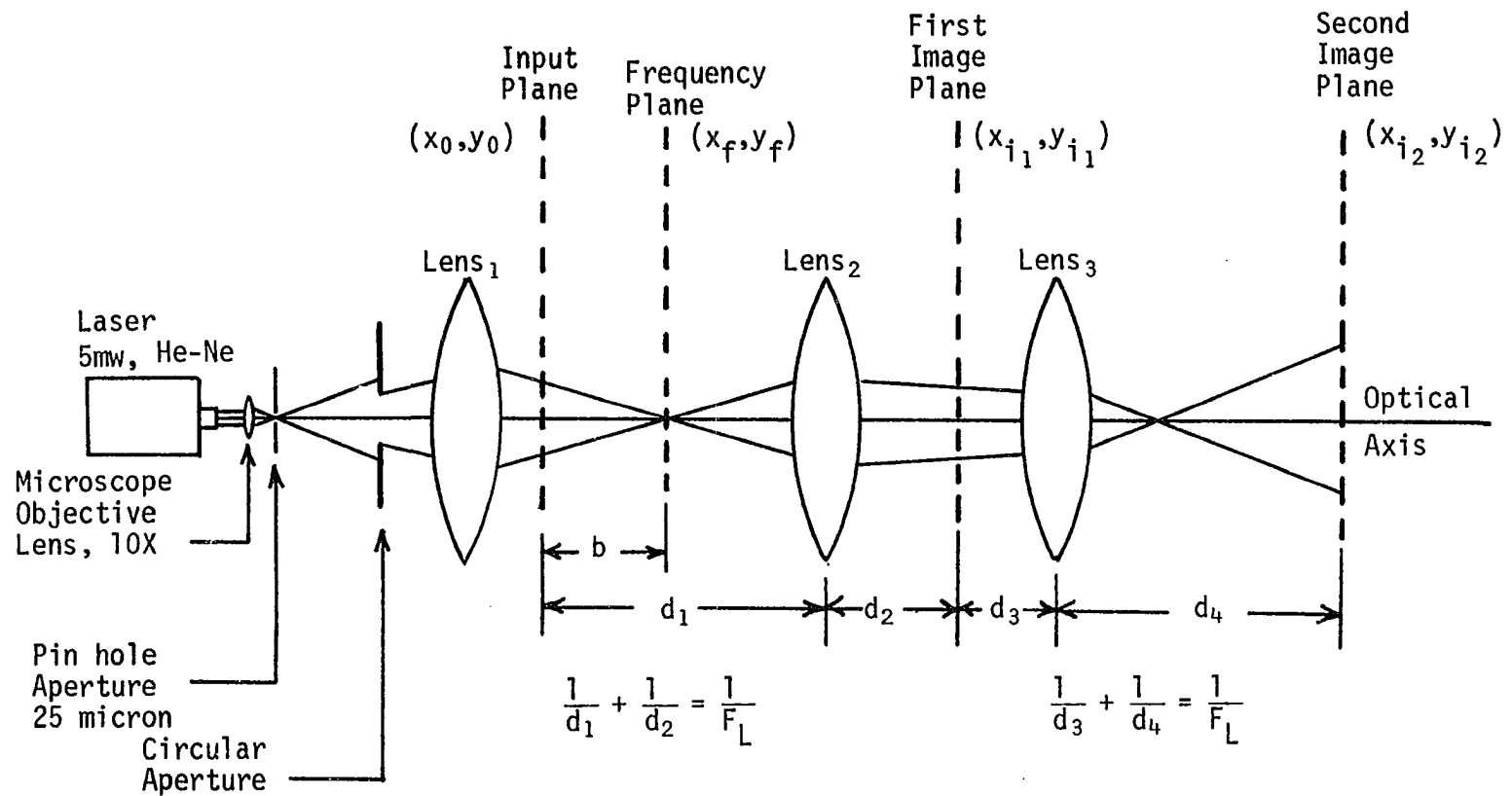
Input Plane

Frequency Plane

First Image Plane

Second Image Plane

(x_0, y_0)

(x_f, y_f)

(x_{i_1}, y_{i_1})

(x_{i_2}, y_{i_2})

$Lens_1$

$Lens_2$

$Lens_3$

Laser
5mw, He-Ne

Optical
Axis

Microscope
Objective
Lens, 10X

Pin hole
Aperture
25 micron

Circular
Aperture

b

d_1 d_2 d_3 d_4

$$\frac{1}{d_1} + \frac{1}{d_2} = \frac{1}{F_L}$$

$$\frac{1}{d_3} + \frac{1}{d_4} = \frac{1}{F_L}$$

Figure 56. Optical system used to simultaneously process two separate density modulated transparencies.

radius, R_0, of the input circular aperture equal to 0.5 cm, the diameter of the central maximum of the Airy pattern was equal to 0.082 mm. Thus, the spatial filter width (W = 0.26 mm) was approximately three times the Airy disk central diameter. For nearly maximum accuracy in computing the convolution and correlation functions, a slit width approximating the Airy disk central diameter is required. However, in practice, using nonprecision positioning equipment, a spatial filter with a slit width dimension slightly greater than ideal is much more easily positioned.

Three similar 52 mm diameter, 193 mm focal length coated achromatic lenses were used in the optical system. The third lens shown in Figure 56 was used to magnify the distribution, $\underline{U}_{i_1}(x_{i_1}, y_{i_1})$, in the first image plane. The distribution, $\underline{U}_{i_2}(x_{i_2}, y_{i_2})$, in the second image plane was thus a magnified (by a factor d_4/d_3) and a spatially inverted version of the distribution in the first image plane. Since the distribution in the first image plane was a magnified, inverted, spatially filtered version of the input plane distribution, the distribution in the second image plane was a magnified, noninverted spatially filtered version of the input plane distribution. The mathematical description of $\underline{U}_{i_2}(x_{i_2}, y_{i_2})$ is from Equations 1-36 and 1-42, given by

$$\underline{U}_{i_2}(x_{i_2}, y_{i_2}) = \frac{d_1 d_3}{d_2 d_4} \exp\left[\frac{j2\pi}{\lambda}(d_1 + d_2 + d_3 + d_4)\right]$$

$$\exp\left[\frac{j\pi}{\lambda d_4}(1 + \frac{d_3}{d_4})(x_{i_2}^2 + y_{i_2}^2)\right]$$

$$\exp\left[\frac{j\pi}{\lambda d_2}(1 + \frac{d_1}{d_2} - \frac{d_1^2}{bd_2})(\frac{d_3^2}{d_4^2})(x_{i_2}^2 + y_{i_2}^2)\right]$$

$$t_0'(\frac{d_1 d_3}{d_2 d_4} x_{i_2}, \frac{d_1 d_3}{d_2 d_4} y_{i_2}) \tag{2-68}$$

where t_0' is the spatially filtered version of the input transmittance function. The distances were:

$$d_1 = 74.8 \text{ cm}$$

$$d_2 = 26.1 \text{ cm}$$

$$d_3 = 24.4 \text{ cm}$$

$$d_4 = 96.0 \text{ cm}$$

Thus, the total magnification was

$$M = d_2 d_4 / d_1 d_3 = 1.37 \tag{2-69}$$

The detection system previously described in Part I was used to record the relative intensity versus distance along the x_{i_2}'-axis in the second image plane.

EXPERIMENTAL RESULTS AND DISCUSSIONS

Photographs of the intensity distribution in the frequency plane produced by various cascaded input signal transparencies are shown in Figure 57. It is evident from each photograph that the intensity distribution along the x_f or the x_f-axis is related, respectively, to the spectral distribution of the input signal transparency positioned along the corresponding axis, x_0 or y_0, in the input plane. It is also evident that the off-axis intensity distribution is related to the product of the spectral distributions. It is noted from Figure 57a that the off-axis distribution is located along the diagonal lines $x_f = y_f$ and $x_f = -y_f$ since the input signals were the same frequency.[1] Similar results are evident for the distribution shown in Figure 57b. The input signal transparencies used to produce the intensity distribution shown in Figure 57c did not contain any common nonzero frequency components. Thus, as should be expected, the distribution along the diagonal lines $x_f = y_f$ and $x_f = -y_f$, for $x_f \neq 0$, is zero.

The input transparencies used to produce the distributions shown in Figure 57d, 57e, and 57f contained records of signals with much more involved frequency spectra than the sinusoidal examples given in Figures 57a, 57b, and 57c. Thus, the off-axis distribution in each case is more

---

[1]The off-axis light amplitude distribution along the diagonal lines $x_f = y_f$ and $x_f = -y_f$ is related respectively to $\underline{G}_1(f_x) \underline{G}_2(f_x)$ and $\underline{G}_1(f_x) \underline{G}_2(-f_x)$. However, since photographic film responds to light intensity rather than light amplitude, the intensity distributions along these diagonal lines are equal as evident in the photographs.

Figure 57. Photographs of the intensity distributions in the frequency plane produced by various density modulated input signal transparencies.

(a) The x_0-axis and the y_0-axis input transparencies were records of a 15 Hz 1.0 volt peak-to-peak sinusoidal signal.

(b) The x_0-axis and the y_0-axis input transparencies were records of a 20 Hz 1.0 volt peak-to-peak sinusoidal signal.

(c) The x_0-axis input transparency was a record of a 10 Hz 1.0 volt peak-to-peak sinusoidal signal. The y_0-axis input transparency was a record of a 15 Hz 1.0 volt peak-to-peak sinusoidal signal.

(d) The x_0-axis and the y_0-axis input transparencies were records of the ECG signal.

(e) The x_0-axis input transparency was a record of the instantaneous differential blood pressure waveform for the simulated stenotic condition. The y_0-axis input transparency was a record of the instantaneous blood flow waveform for the simulated stenotic condition.

(f) The x_0-axis and the y_0-axis input transparencies were records of the EEG signal.

(a)

(b)

(c)

(d)

(e)

(f)
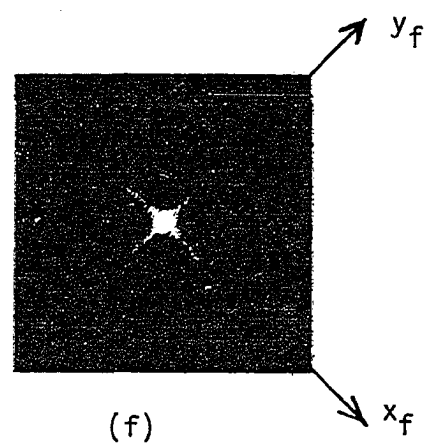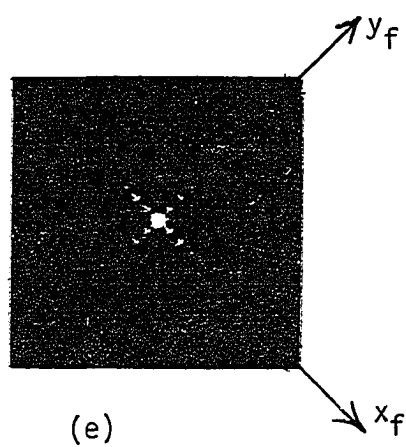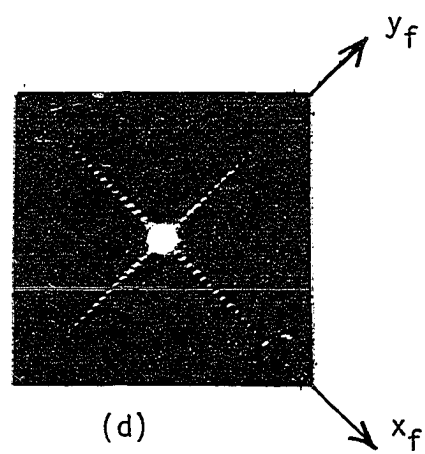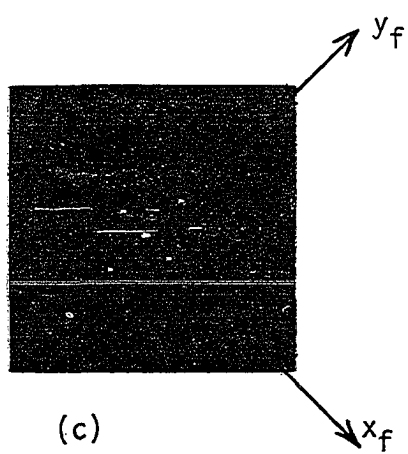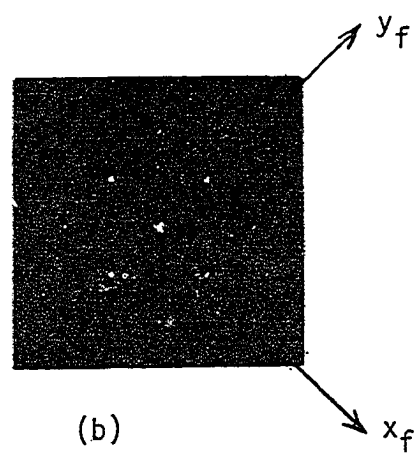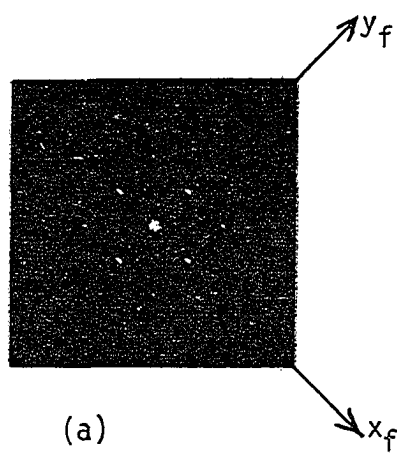
involved. However, for each of these examples, the off-axis distribution along the diagonal lines $x_f = y_f$ and $x_f = -y_f$ contains the frequency components common to both input signal transparencies. It is significant to note the relative intensity of the off-axis distributions as compared to the on-axis distributions. The off-axis distribution is much less intense as is evident from Figure 57d. This is due to the fact that the off-axis terms are proportional to $\left| \underline{G}_1(f_x) \; \underline{G}_2(f_y) \right|^2$ while the on-axis terms are proportional to $\left| B_2 \underline{G}_1(f_x) \right|^2$ or $\left| B_1 \underline{G}_2(f_y) \right|^2$ where B_1 and B_2 are constant bias terms that are, respectively, greater than the amplitudes of $g_1(x)$ and $g_2(y)$.

Photographs of the intensity distribution at various planes in the optical system are shown in Figure 58. The input signal transparencies used in this demonstration each contained records of a 10 Hz 1.0 volt peak-to-peak sinusoidal signal. A photograph of the intensity distribution in the frequency plane produced by these input transparencies is given in Figure 58a. The photograph given in Figure 58b shows the intensity distribution in the second image plane for the case where the spatial filter was removed from the frequency plane. Thus, this is the undistorted image of the input transparencies. The photograph given in Figure 58c shows the intensity distribution behind[1] the narrow slit spatial filter. The spatial filter orientation corresponded to an angle $\theta = 45°$ from the x_f-axis (f_x-axis). It is evident from the photograph that this distribution contains only the terms along the $x_f = y_f$ ($f_x = f_y$)

---

[1]The optical configuration shown in Figure 9 was used to photograph the distribution behind the spatial filter. The camera was placed in the second frequency plane.

Figure 58. Photographs of the intensity distribution at various points in the optical system produced by two input transparencies each containing records of a 10 Hz 1.0 volt peak-to-peak sinusoidal signal.

(a) Intensity distribution in the frequency plane.

(b) Intensity distribution in the second image plane without spatially filtering the frequency plane distribution.

(c) Intensity distribution in the frequency plane behind the narrow slit spatial filter. The spatial filter orientation corresponded to an angle of $\theta = 45°$ from the positive x_f-axis (f_x-axis).

(d) Intensity distribution in the second image plane with the spatial filter oriented as indicated in (c). This image corresponds to the squared value of a constant bias term plus the optically computed convolution function of the two sinusoidal signals.

(a)

(b)

(c)

(d)
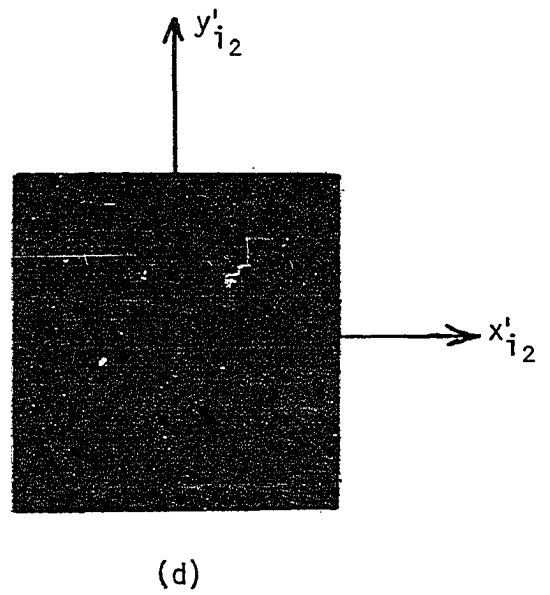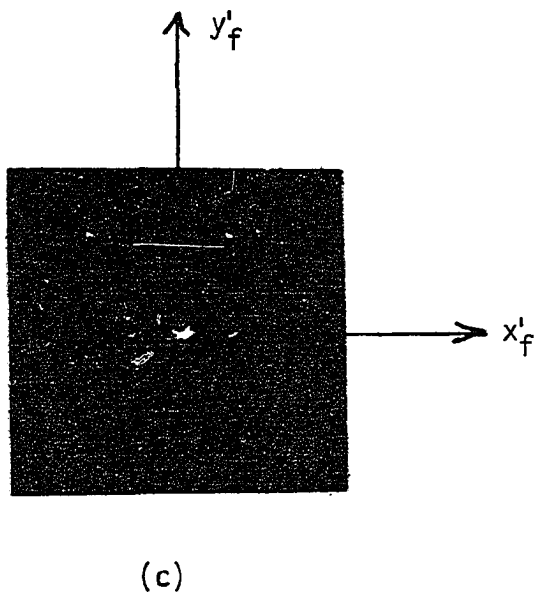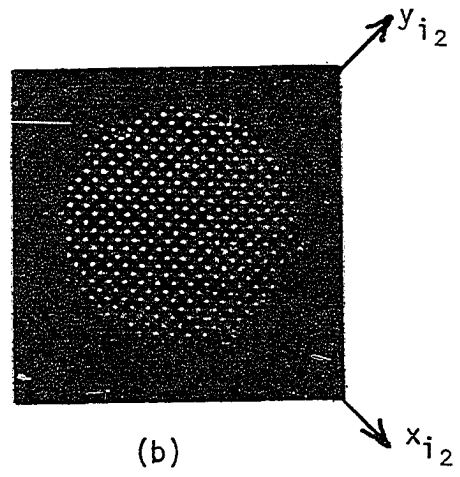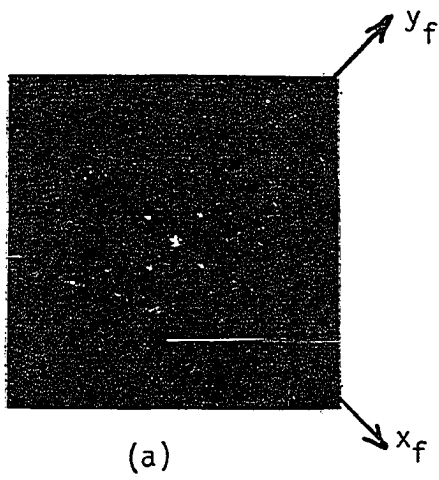
diagonal line. The photograph of the intensity distribution in the second image plane for this case is given in Figure 58d. This intensity distribution corresponds to the squared value of a constant bias term plus the optically computed convolution function. The constant term could have been removed by optically filtering the zero frequency distribution at the origin of the frequency plane. However, since intensity is being detected in the image plane, this constant bias term was not removed.

It is evident, from Figure 58b, that approximately 20 cycles of these 10 Hz sinusoidal signals were being optically processed. The number of cycles in the optically computed convolution function is, from Figure 58d, approximately 28 cycles. This result agrees with that predicted by Equation 2-64. A plot[1] of the relative intensity as a function of distance along the x'_{1_2}-axis is given in Figure 59. The horizontal axis represents displacement time τ with units of seconds.

Theoretically, this plot should be sinusoidal in nature containing uniform peak-to-peak amplitude sine waves across the computed interval. Also, the envelopes connecting both the maximum and minimum peaks should both be parallel to the horizontal axis. This experimental result does in part compare favorably with the theoretically predicted result. However, the deviation from the predicted result was due primarily to the fact that the circular aperture used to limit the area of the input plane was not

---

[1]This plot is directly related to the squared value of a constant bias term plus the optically computed convolution function. Such plots will be referred to as the optically computed convolution function for brevity, and will be denoted by the function $[P'_{12}(\tau)]^2$. The prime superscript will indicate that a bias constant is included in this function.
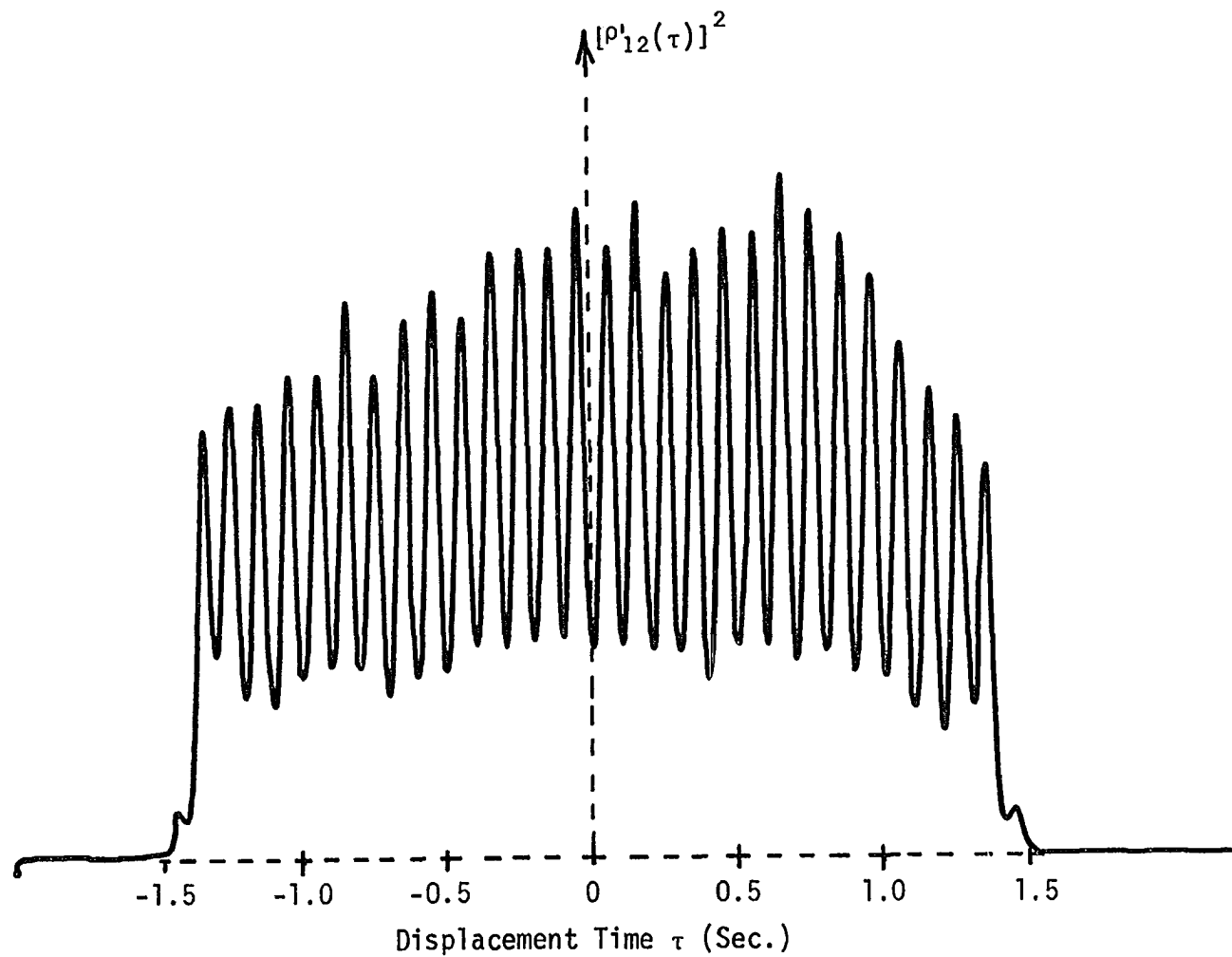
Figure 59. Optically computed convolution function for two 10 Hz 1.0 volt peak-to-peak sinusoidal signals.

placed in the input plane, but instead was positioned in a plane preceding the first lens (see Figure 56). Since the distribution in the second image plane is a spatially filtered image of the input plane and since the circular aperture was not located in the image plane, the image plane distribution contained a slightly misfocused image of this circular aperture plus a focused spatially filtered input plane distribution. Thus, there were some diffraction effects at the edge of the image due to this misfocused circular aperture.

Other factors may have caused the slight inaccuracies in this optically computed result. These include: nonuniform transverse amplitude of the illuminating laser beam; dust on the transparencies and/or the lenses; misalignment of the lenses and/or the spatial filter; imperfect lenses; and/or inaccuracies in the transparency records.

The photographs shown in Figure 60 were taken at various planes in the optical system. The x_0-axis input signal used in this demonstration contained a record of a 10 Hz 1.0 volt peak-to-peak sinusoidal signal, and the y_0-axis input transparency contained a record of a 15 Hz 1.0 volt peak-to-peak sinusoidal signal. A photograph of the intensity distribution behind the spatial filter is given in Figure 60b. The spatial filter orientation corresponded to an angle $\theta = -45°$ from the positive x_f-axis (f_x-axis). The photograph given in Figure 60c shows the intensity distribution in the second image plane for this spatial filter orientation. The intensity distribution in the image plane thus corresponded to the

Figure 60.   Photographs of the intensity distribution at various planes
in the optical system.   The x_0-axis input transparency was
a record of a 10 Hz 1.0 volt peak-to-peak sinusoidal sig-
nal.   The y_0-axis input transparency was a 15 Hz 1.0 volt
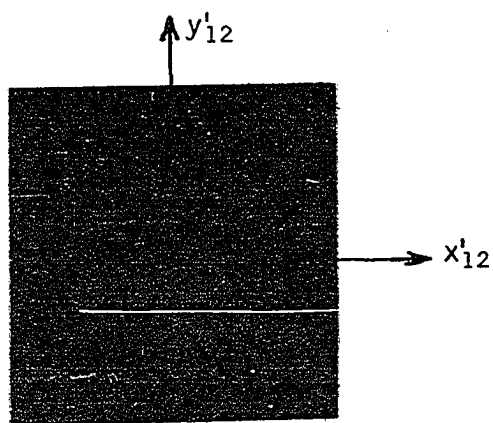peak-to-peak sinusoidal signal.

(a)   Intensity distribution in the frequency plane.
(b)   Intensity distribution in the frequency plane directly
behind the spatial filter.
(c)   Intensity distribution in the second image plane.
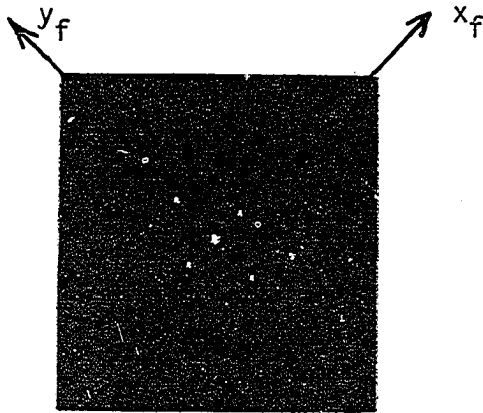
(a)
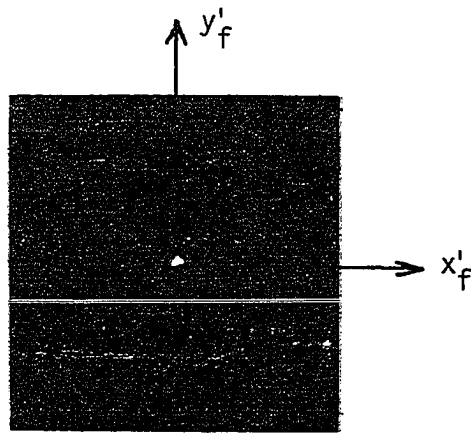
(b)

(c)

optically computed correlation function[1] for the input signals. Since the input signal transparencies did not contain any common nonzero frequency components, the image intensity along the x'_{i_2}-axis was essentially constant over the computed interval.

A comparison was made between the optically computed and mathematically computed convolution and correlation functions. The signals used in this comparison were two equal ramp waveforms as illustrated in Figure 61. Two such signals were transcribed on separate density modulated transparencies. The duration period, T, of these waveforms was 0.35 seconds and the peak amplitude was 1.0 volt. A photographic print of one of the transparencies is given in Figure 62. Photographs of the intensity distribution in the second image plane are given in Figure 63. The intensity distribution shown in Figure 63a corresponds to the optically computed convolution function for the ramp waveforms, while the distribution shown in Figure 63b corresponds to the optically computed autocorrelation function for these waveforms. The relative intensity plots for these optically computed functions are given in Figure 64a. The mathematically computed squared convolution and autocorrelation functions, for the functions shown in Figure 61, are given in Figure 64b. It is evident that the optically computed functions are similar to those computed mathematically. The autocorrelation function in both cases is symmetrical about the $\tau = 0$ axis with the peak occurring at $\tau = 0$. The convolution function is non-

---

[1]The notation $[\psi'_{12}(\tau)]^2$ or $[\psi'_{11}(\tau)]^2$ will be used to denote, respectively, the optically computed crosscorrelation or autocorrelation functions. The prime superscript will indicate that a bias constant is included in these functions.
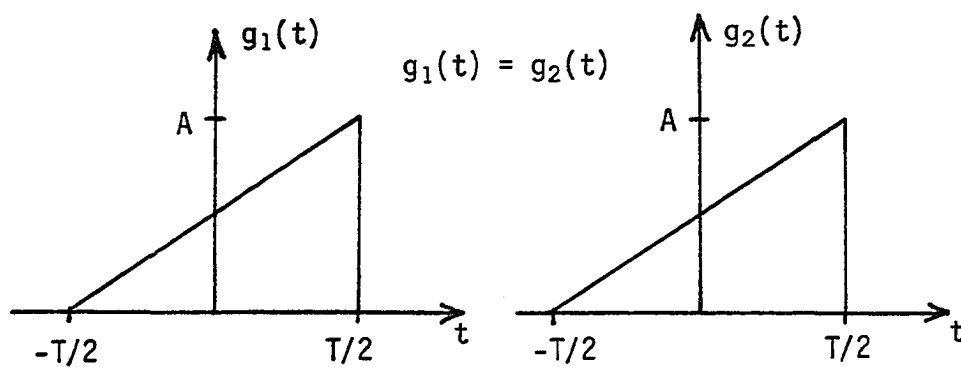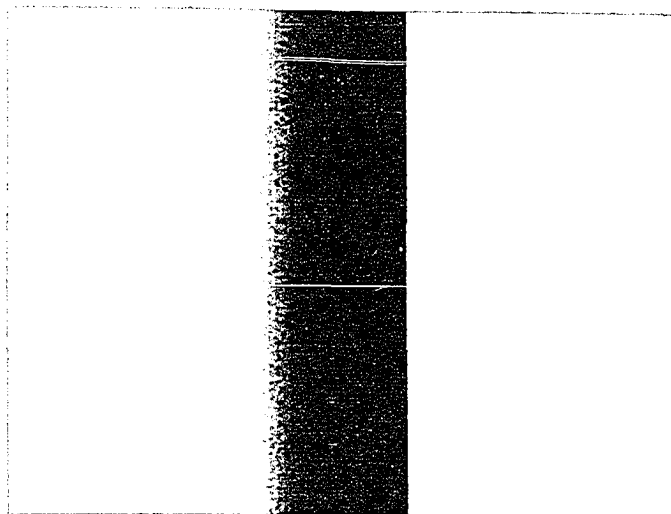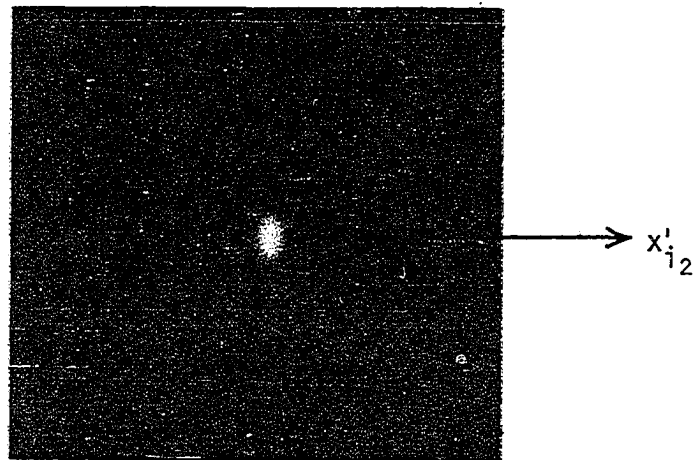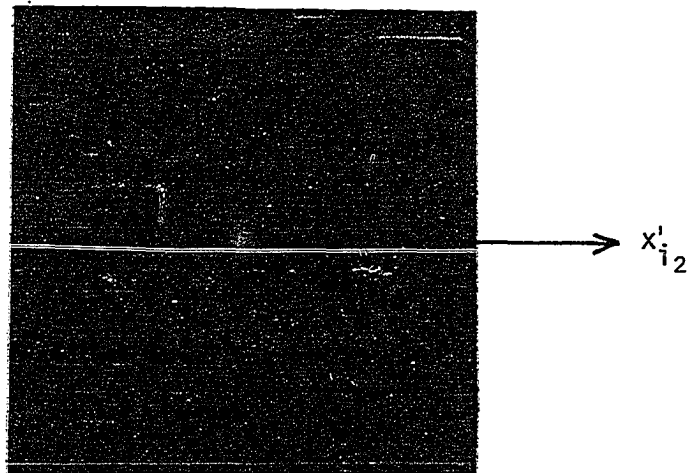
Figure 61. Two equal ramp waveforms.

Figure 62. A photographic print of the density modulated record of a ramp signal.

(a)

(b)

Figure 63. Photograph of the intensity distribution in the second image
plane. The input transparencies each contained the record of
a ramp waveform.

(a) The intensity distribution corresponds to the optically com-
puted convolution function for the two waveforms. The spatial
filter orientation corresponded to an angle $\theta = 45°$.

(b) The intensity distribution corresponds to the optically com-
puted autocorrelation function for the ramp waveforms. The
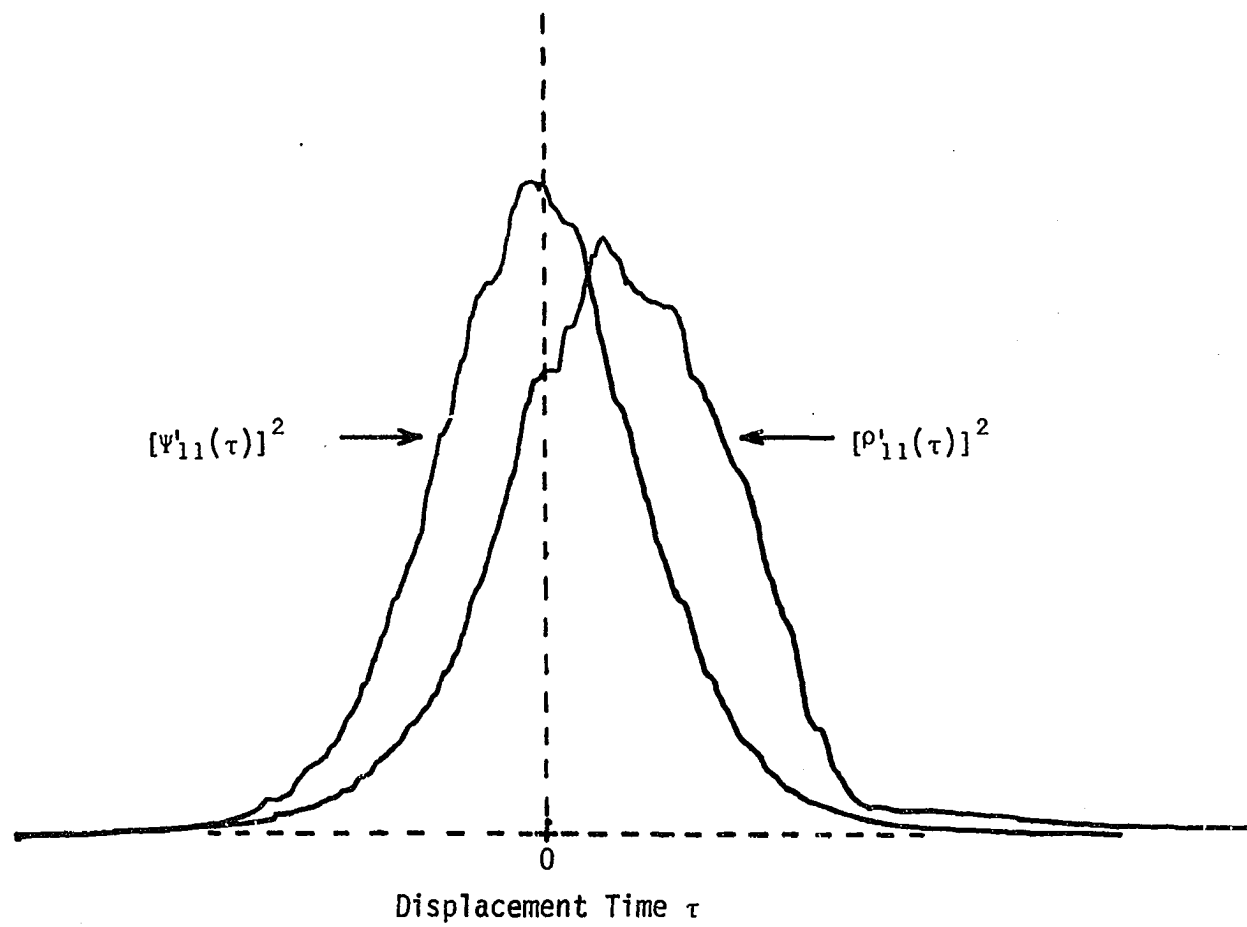spatial filter orientation corresponded to an angle $\theta = -45°$.

Figure 64a. Optically computed convolution and autocorrelation functions for identical ramp function inputs.

$$\left[\frac{8}{A^2T}\right]^2 \psi_{11}^2(\tau) \longrightarrow \qquad \longleftarrow \left[\frac{8}{A^2T}\right]^2 \rho_{11}^2(\tau)$$
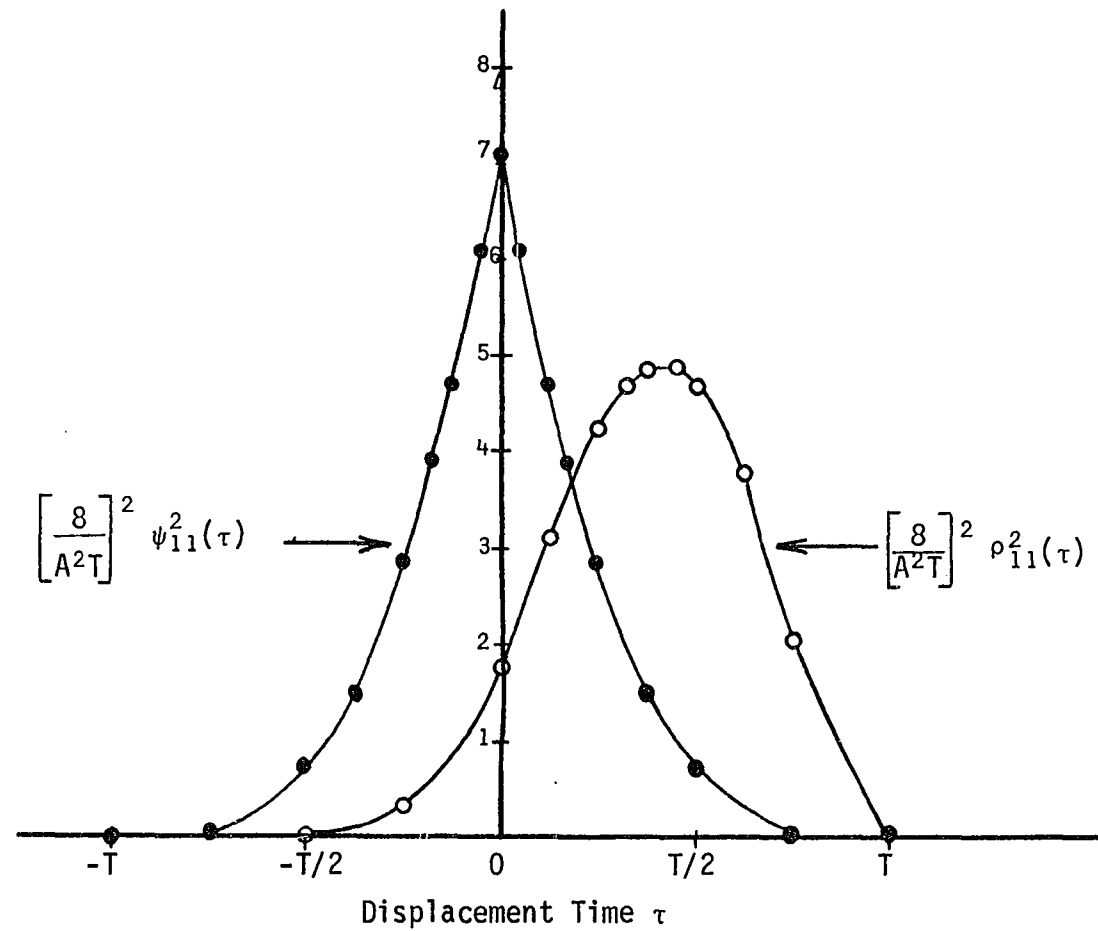
Displacement Time τ

Figure 64b. Mathematically computed squared convolution and autocorrelation functions for the functions given in Figure 61.

symmetrical, and in both results the peak occurs at a positive displacement time. However, the ratio of the peak value of the autocorrelation function to the peak value of the convolution function is lower for the optically computed results than the results predicted mathematically. A source for this error may have been the width, W, of the spatial filter slit. The maximum theoretical accuracy of this optical technique occurs when the slit width approximately equals the diameter of the central maximum of the Airy disk. Thus, reducing the filter width may reduce the error. However, a reduction in slit width not only presented orientation problems, but it also reduced the light intensity representing these optically computed results.

The accuracy of the transparency record of the ramp waveforms was investigated as another source of error in these optically computed results. This was accomplished by positioning one of the transparencies along the x_0-axis in the input plane. With the spatial filter removed from the frequency plane, a plot of the relative intensity distribution along the x_{i_2}-axis in the second image plane was recorded (see Figure 65). This relative intensity profile is directly related to the intensity transmittance of the input transparency. Theoretically then, the intensity profile should be related to a squared ramp function. Thus, it is evident from this observation that the transcribed record is inaccurate. This inaccuracy may be attributed to the inherent 60 Hz intensity modulation of the CRT beam, and to the intensity halo around the CRT beam. The effect of the halo in distorting the transcription of this waveform
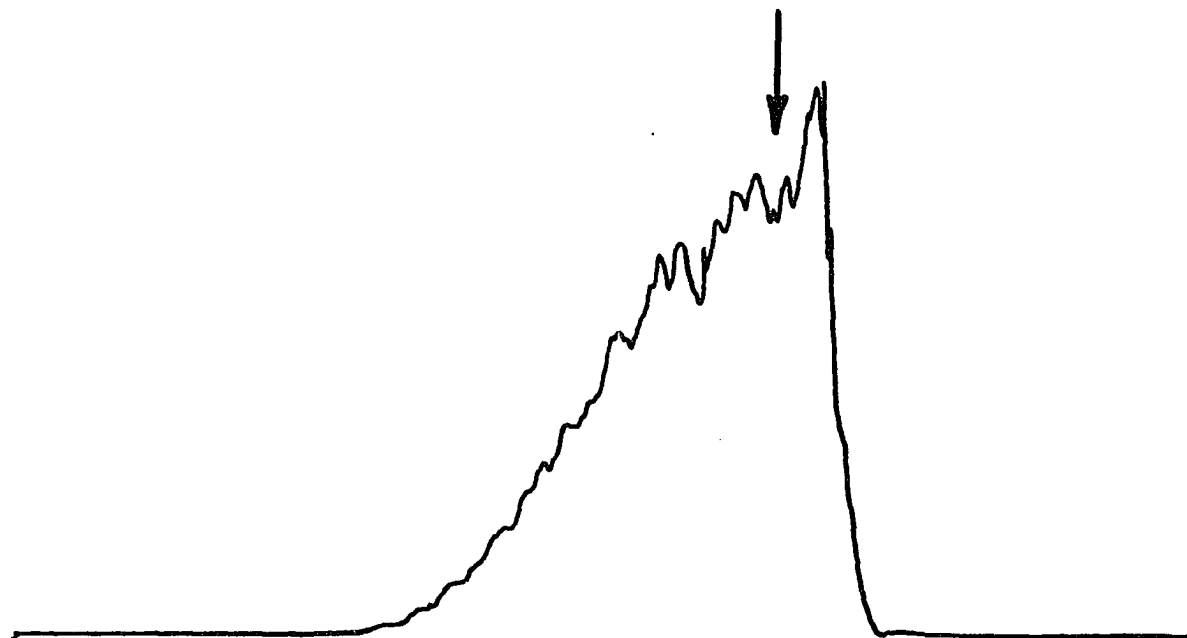
Figure 65. A plot of the relative intensity along the x_{i2}-axis for a transparency containing the record of a single pulse ramp waveform placed along the x_0-axis in the input plane.

is prevalent near the waveform peak[1] (indicated by the arrow in Figure 65). The effect of the beam halo is clearly evident in the spatially filtered intensity profiles given in Figure 66. Thus, when considering the quality of these input transparencies, the optically computed convolution and autocorrelation results compare favorably with the mathematically predicted results.

The functions $[\rho'_{12}(\tau)]^2$, $[\rho'_{21}(\tau)]^2$, $[\psi'_{12}(\tau)]^2$, and $[\psi'_{21}(\tau)]^2$ were optically computed using a transparency record of the simulated stenotic instantaneous blood pressure waveform and a transparency record of the simulated stenotic instantaneous blood flow waveform. The purpose of these computations was to demonstrate the convolution and crosscorrelation properties

$$\rho_{12}(\tau) = \rho_{21}(\tau) \qquad (2\text{-}70)$$

and

$$\psi_{12}(\tau) = \psi_{21}(-\tau) \qquad (2\text{-}71)$$

The results of this demonstration are given in Figure 67. The optically computed convolution functions are shown in Figures 67a and 67b. The subscripts 1 and 2 refer, respectively, to the instantaneous pressure waveform and the instantaneous flow waveform. It is evident, when noting the relationship of two contiguous peaks, that these optically computed functions do satisfy the convolution property given in Equation 2-70.

---

[1]The intensity of the halo around the CRT beam was directly related to the beam intensity. Thus, as the beam intensity increased at the instant just past the waveform peak, the halo intensity also increased. Since the halo intensity also affected the film density, the halo then distorted the peak of the transcribed record of this waveform.
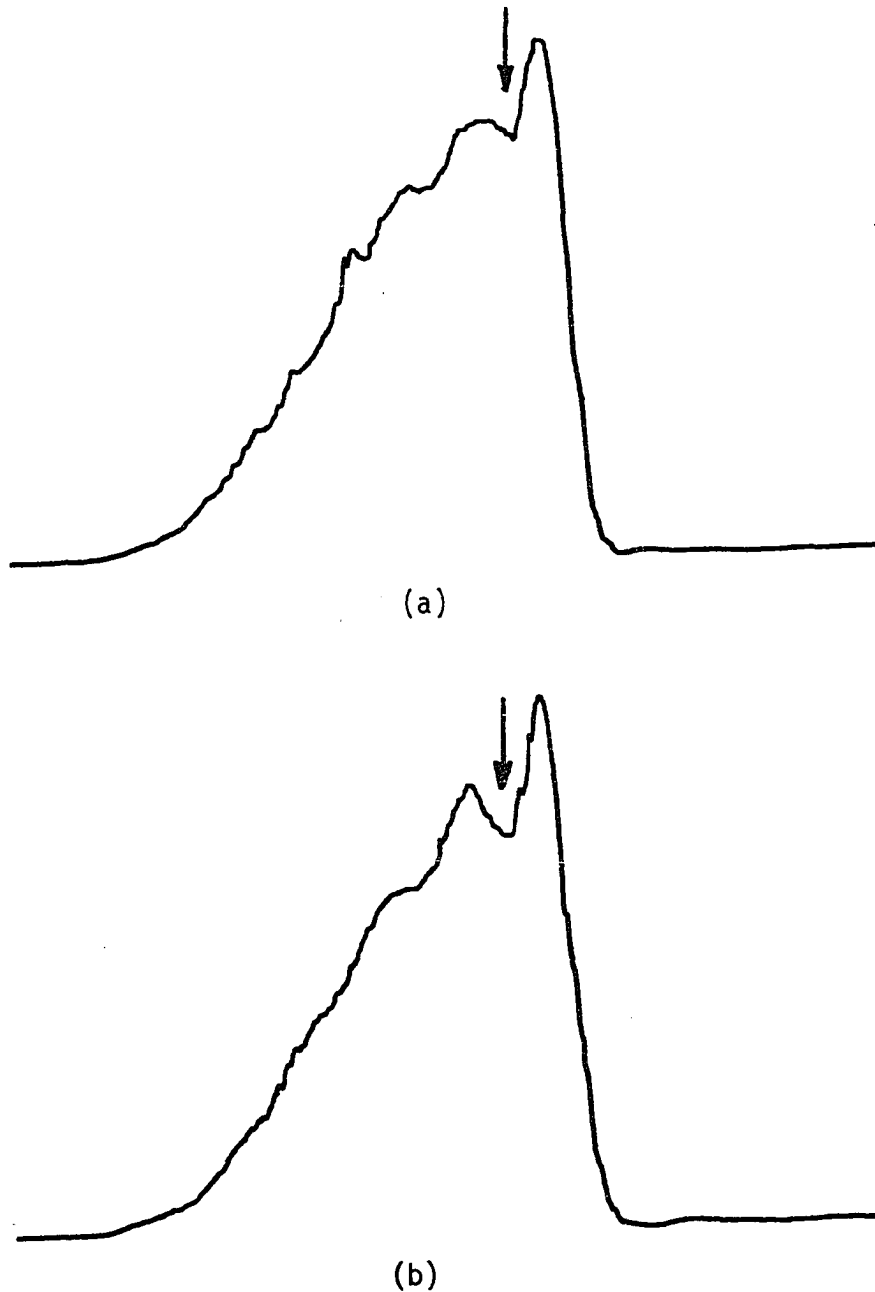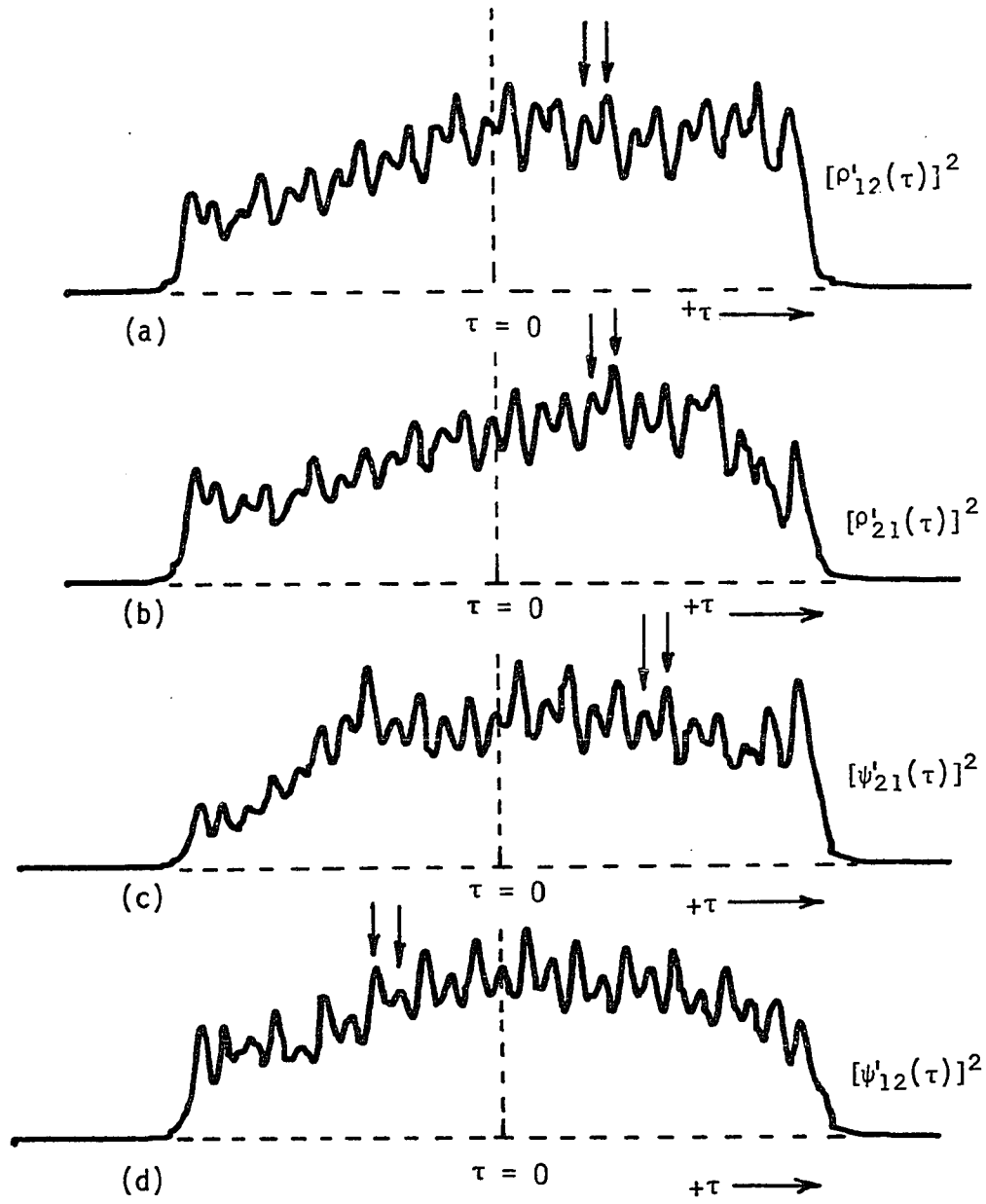
Figure 66. Optically filtered intensity profiles of the transcribed ramp waveform.

(a) The frequency components greater than 30 Hz have been optically removed by a low-pass spatial filter.
(b) The frequency components greater than 15 Hz have been optically removed by a low-pass spatial filter.

Figure 67.   Optically computed convolution and crosscorrelation functions for the simulated stenotic instantaneous blood pressure and flow waveforms.

(a)   Optically computed convolution function for the blood pressure and blood flow waveforms.
(b)   Optically computed convolution function for the blood flow and blood pressure waveforms.
(c)   Optically computed crosscorrelation function for the blood flow and blood pressure waveforms.
(d)   Optically computed crosscorrelation function for the blood pressure and blood flow waveforms.

$[\rho'_{12}(\tau)]^2$

(a) $\tau = 0$ $+\tau \longrightarrow$

$[\rho'_{21}(\tau)]^2$

(b) $\tau = 0$ $+\tau \longrightarrow$

$[\psi'_{21}(\tau)]^2$

(c) $\tau = 0$ $+\tau \longrightarrow$

$[\psi'_{12}(\tau)]^2$

(d) $\tau = 0$ $+\tau \longrightarrow$

Similarly, by comparing the two optically computed crosscorrelations functions given in Figures 67c and 67d, it is evident that the crosscorrelation property of Equation 2-71 is satisfied. Since these experimental results agree well with the theoretical predictions, it can be stated that this optical processing technique does in fact produce the convolution and correlation functions for two real one-dimensional signals.

The plots shown in Figure 68 represent the optically computed crosscorrelation functions for the instantaneous blood pressure and the instantaneous blood flow waveforms. The plot given in Figure 68a is the optically computed crosscorrelation function for the normal blood pressure and the normal blood flow waveform, while Figure 68b shows the plot of the optically computed crosscorrelation function for the normal blood pressure waveform and the simulated stenotic blood flow waveform. Comparing the two plots, it is clear that there is a measure of similarity between the pressure waveform and both the normal and simulated stenotic waveforms. Also, it is clear in comparing the relative peak-to-peak amplitude in both plots that there is greater correlation[1] between the normal pressure and flow waveforms than for the normal pressure and simulated stenotic waveforms.

A photograph of the intensity distribution in the second image plane produced by two EEG input signal transparencies is given in Figure 69a. The spatial filter position corresponded to an angle $\theta = -45°$. Thus, the distribution along the x'_{i_2}-axis corresponded to the optically computed

---

[1]The vertical scales on both plots of Figure 68 are equal and the transcribed signals on the input transparencies were equal in peak-to-peak amplitude.

Figure 68. Optically computed crosscorrelation functions for the
instantaneous blood pressure and instantaneous blood flow
waveforms.

(a) Crosscorrelation of the normal instantaneous blood pressure
and normal instantaneous blood flow waveforms.
(b) Crosscorrelation of the normal instantaneous blood pressure
and simulated stenotic instantaneous blood flow waveform.

$[\psi'_{12}(\tau)]^2$

Displacement Time τ (Sec.)

(a)

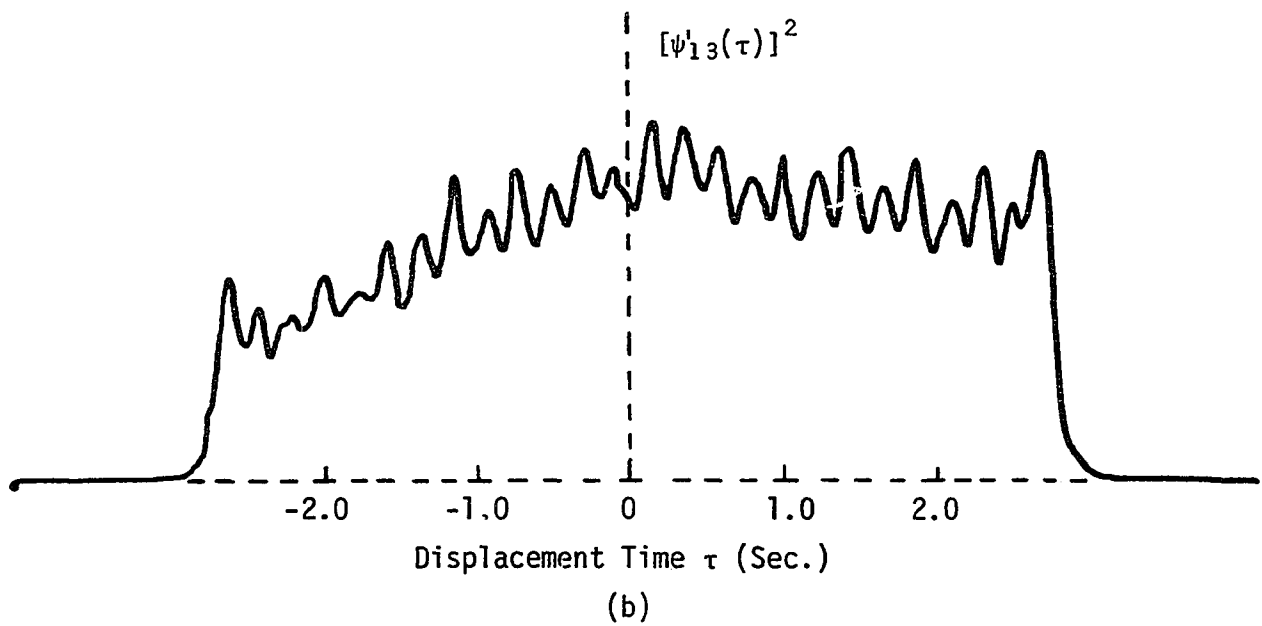$[\psi'_{13}(\tau)]^2$
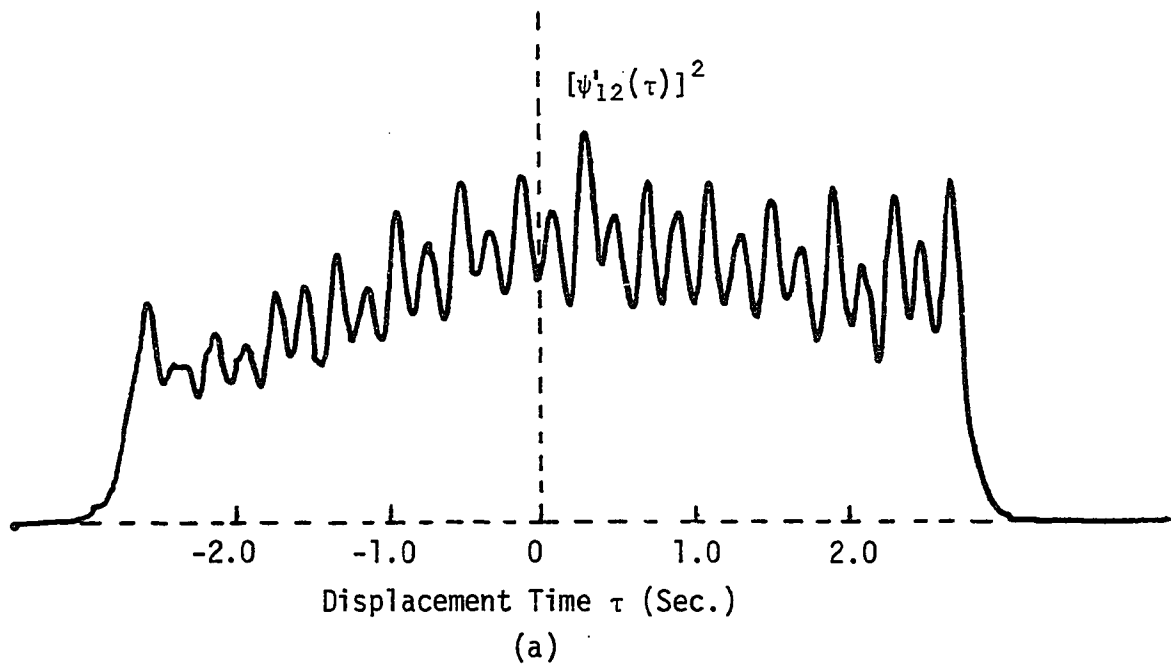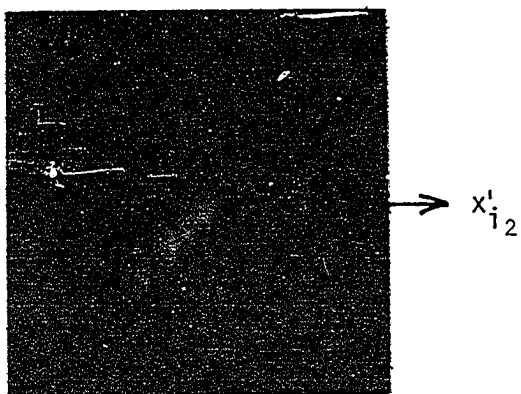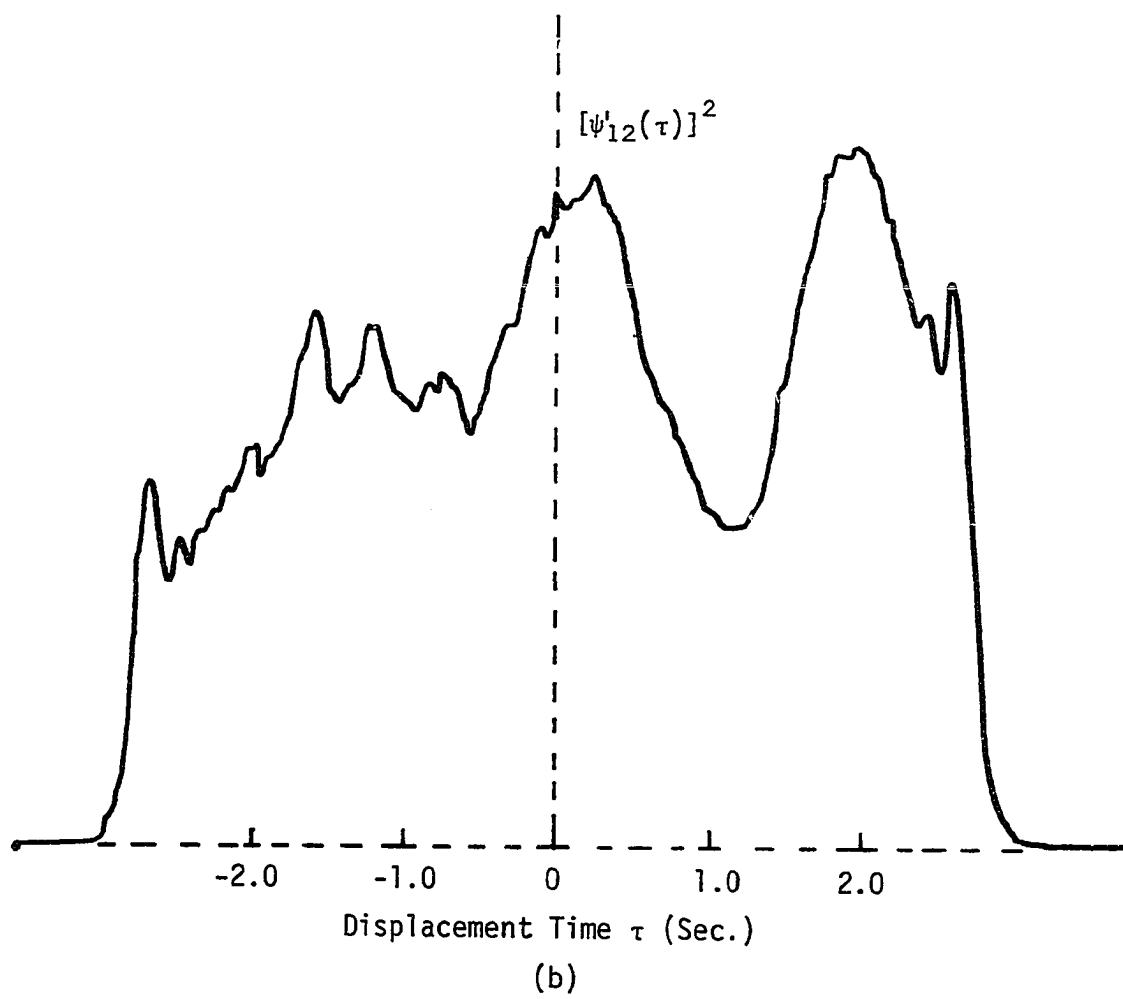
Displacement Time τ (Sec.)

(b)

Figure 69a. Photograph of the intensity distribution in the second image plane produced by two EEG signal transparencies.

Figure 69b. Optically computed crosscorrelation function for two EEG signals.

(a)

$[\psi'_{12}(\tau)]^2$

Displacement Time τ (Sec.)

(b)

crosscorrelation function. It is evident from this photograph that there was intensity variation also along the y'_{i_2}-axis. The variations in the y'_{i_2}-axis give evidence that the slit width, W, was larger than optimum for continuous spectra.

Figure 69b shows a plot of the optically computed crosscorrelation function for these EEG signals. Care must be exercised in interpreting this plot since the nonoptimal slit width permits the passage of frequency components not common to both signals. Also, strictly speaking, using short segments of a nonstationary random function does not permit accurate computation of crosscorrelation function.

CONCLUSIONS AND RECOMMENDATIONS

The inherent two-dimensional parallel processing capabilities of a relatively simple optical system enable simultaneous spectral analysis of two appropriately cascaded density modulated signal transparencies representing real one-dimensional inputs. It has been shown that these spectral descriptions of two independent inputs are simultaneously available along the f_x- and f_y-axes of the frequency plane. Furthermore, the off-axis distribution contains spectral information which can be used to determine the convolution and correlation relationships between the input functions.

For real input functions, the off-axis distribution along the +45° diagonal in the frequency plane is seen to be the product of the common spectra of the inputs, the Fourier transform of which is the folded convolution function for such real inputs. These frequency domain components can be utilized for such a computation by simply placing a narrow slit spatial filter along the +45° diagonal in the frequency plane and inverse transforming through the use of a second lens system.

The off-axis distribution along the -45° diagonal in the frequency plane contains the product of the frequency spectrum of one input function and the folded spectrum of the second input function. For real input functions, the Fourier transform of this distribution is the correlation function relating the inputs. As in the case of convolution, a narrow slit filter oriented along the -45° diagonal permits the second lens system to transform only these off-axis components of interest.

In contrast to the Vander Lugt [20] technique for convolution and correlation, this method does not require the laborious production of a holographic frequency plane filter. This constitutes a significant advantage when one-dimensional data records are to be analyzed.

Evidence that the optical system investigated did indeed produce the theoretically expected convolution and correlation functions fell into three categories. First, comparison of the optically computed convolution and autocorrelation functions for identical ramp waveforms to the mathematically exact functions shows obvious similarity of form and position. Inaccuracies for this test can be attributed to imperfections of the real optical system and the transcribed signal records.

The symmetry relationships

$$\rho_{12}(\tau) = \rho_{21}(\tau) \tag{2-72}$$

and

$$\psi_{12}(\tau) = \psi_{21}(-\tau) \tag{2-73}$$

for the convolution and crosscorrelation of two input functions asymmetrical about their axis were also shown to be valid for the optically computed results. Periodic blood pressure and blood flow waveforms were used in these tests.

Finally, analysis of essentially random EEG signals resulted in a random crosscorrelation function as would be expected for such a case.

In future refinements of this processing technique, some recommendations for improving the performance and accuracy are suggested. As recommended in the conclusions of Part I, a new film density modulation recording system should be developed. By appropriate scaling of the input

record, the size of the frequency plane distribution can be increased, and thus increase the resolution.

Additional recommendations necessary for convenient and accurate convolution and correlation computations are suggested. Using an input circular aperture of larger diameter will reduce the size of the Airy distribution which will increase the resolution. Intentionally predistorting the input signals to match the film density-log exposure characteristics will increase the transcribed signal amplitude of the density modulated record. This will increase the optical signal to noise ratio, and also increase the light amplitude of the optically computed results. Micropositioners controlling the orientation of the input signal transparencies and the spatial filter would reduce positioning errors, and thus permit using a smaller slit width spatial filter. Also, a change in the detection system is suggested. A square root amplifier would permit direct plotting of the convolution and correlation functions.

In conclusion, the utility of coherent optical processing for the analysis of real one-dimensional signals, from biological or other sources, has been demonstrated. The coherent optical system has the inherent parallel processing capabilities that suit it to such sophisticated computations as Fourier transformation, convolution, and correlation.

BIBLIOGRAPHY

1. Lee, Y. W. Statistical Theory of Communication. New York: Wiley, 1960.

2. Lathi, B. P. Signals, Systems and Communication. New York: Wiley, 1965.

3. Bracewell, R. N. The Fourier Transform and Its Applications. New York: McGraw-Hill, 1965.

4. Papoulis, A. The Fourier Integral and Its Applications. New York: McGraw-Hill, 1962.

5. Golden, D. P., Jr., Wothuis, R. A., and Hoffler, G. W. "A spectral analysis of the normal resting electrocardiogram." IEEE Trans. on Biomedical Engineering BME-20, No. 5 (September 1973): 366-372.

6. Sklar, B., Hanley, J., and Simmons, W. W. "A computer analysis of EEG spectral signatures from normal and dyslexic children." IEEE Trans. on Biomedical Engineering BME-20, No. 1 (January 1973): 20-26.

7. Rideout, V. C., Bahr, D. E., Beneken, J. E. W., and deWit, B. "Energy spectra of heart sounds as a function of time and frequency." Proceedings of the San Diego Biomedical Symposium 12 (1973): 133-136.

8. Steadman, J. W., Paulter, E. L., Morgan, R. J., and Su, H. "Cross-correlation analysis of the spontaneous electrical activity in nerves." Proceedings of the San Diego Biomedical Symposium 11 (1972): 261-266.

9. Goodman, J. W. Introduction to Fourier Optics. New York: McGraw-Hill, 1968.

10. Preston, K., Jr. Coherent Optical Computers. New York: McGraw-Hill, 1972.

11. Stroke, B. W. An Introduction to Coherent Optics and Holography. 2nd ed. New York: Academic, 1969.

12. Shulman, A. R. Optical Data Processing. New York: Wiley, 1970.

13. Gabor, D. "A new microscope principle." Nature 161, No. 4098 (May 1948): 777-778.

14. Gabor, D. "Holography, 1948-1971." Proc. IEEE 60, No. 6 (June 1972): 655-668.

15. Leith, E. N., and Upatnieks, J. "Wavefront reconstruction with continuous-tone objects." J. Opt. Soc. Am. 53, No. 12 (December 1963): 1377-1381.

16. Collier, R. J., Burckhardt, C. B., and Lin, L. H. Optical Holography. New York: Academic, 1971.

17. Feleppa, E. J. "Holography and Medicine." IEEE Trans. on Biomedical Engineering BME-3, No. 3 (May 1972): 194-205.

18. O'Neill, E. L. "Spatial filtering in optics." IRE Trans. on Information Theory IT-2, No. 2 (June 1956): 56-65.

19. Cutrona, L. J., Leith, E. N., Palermo, C. J., and Porcello, L. J. "Optical data processing and filtering systems." IRE Trans. on Information Theory IT-6, No. 3 (June 1960): 386-400.

20. Vander Lugt, B. A. "Signal detection for complex spatial filtering." IRE Trans. on Information Theory IT-10, No. 2 (April 1964): 139-145.

21. Preston, K., Jr. "A comparison of analog and digital techniques for pattern recognition." Proc. IEEE 60, No. 10 (October 1972): 1216-1231.

22. Hård, S., and Feuk, T. "Character recognition by complex filtering in reading machines." Pattern Recognition 5, No. 2 (June 1973): 75-82.

23. Krulikoski, S. J., Jr., and Kowalski, K. C. "Automatic optical profiling." Photogrammetric Engineering 37, No. 1 (January 1971): 78-84.

24. Dobrin, M. D. "Optical processing in the earth sciences." IEEE Spectrum 5, No. 9 (September 1968): 59-66.

25. Nyberg, S., Orhang, T., and Svensson, H. "Optical processing for pattern properties." Photogrammetric Engineering 37, No. 6 (June 1971): 547-554.

26. Stroke, G. W., and Halioua, M. "Attainment of diffraction limited imaging in high-resolution electron microscopy by 'a posteriori' holographic image sharpening." Optik 35, No. 1 (March 1972): 50-65.

27. Krusos, G. A., Hilal, S. K., Seaman, W. B., and Myers, G. H. "Reduction of penumbra in x-ray images by optical spatial filtering." Applied Physics Letters 16, No. 1 (January 1970): 37-40.

28. Andrews, H. C., Tescher, A. G., and Kruger, R. P. "Image processing by digital computer." IEEE Spectrum 9, No. 7 (July 1972): 20-32.

185

29. Stroke, G. W. "Optical computing." IEEE Spectrum 9, No. 12 (December 1972): 24-41.

30. Casasent, D. P. "A hybrid digital/optical computer system." IEEE Trans. on Computers C-22, No. 9 (September 1973): 852-858.

31. Pernick, B. J., Yustein, D., and Bartolotta, C. "An optical spectrum analyzer for power spectral density measurements." Applied Optics 8, No. 1 (January 1969): 65-73.

32. Felstead, E. B. "Optical Fourier transformation of area modulated spatial functions." Applied Optics 10, No. 11 (November 1971): 2468-2475.

33. Anderson, R. L., and Everett, R. L. "Electroencephalographic and electrocardiographic data reduction by coherent optical techniques." SWIEECO Conf. Rec., 1970, pp. 139-141.

34. Taylor, C. J., Pullan, B. R., and Ashworth, B. "Frequency analysis of time varying electrical signals by an optical method." Medical and Biological Engineering 11, No. 1 (January 1973): 102-103.

35. Lee, T. C., and Gossen, D. "Generalized Fourier-transform holography and its applications." Applied Optics 10, No. 4 (April 1971): 961-963.

ACKNOWLEDGMENTS

I would like to express my appreciation to the many people who have helped in making this dissertation a reality.

I would like to thank Dr. Alvin A. Read, my co-major professor, for initially suggesting this research topic and for supplying the needed technical expertise and tolerant guidance. His supervision is gratefully recognized.

I particularly want to express my appreciation to Dr. William H. Brockman, my co-major professor, for his unwavering encouragement during my graduate studies. The appreciation and thanks that I can show here are very meager when compared to the help and guidance which I have received.

Finally, a very special thanks is extended to my wife, Julie, who made many sacrifices during the course of my studies. Her unfailing encouragement and support have helped me immensely.

APPENDIX: CIRCUIT DIAGRAMS

The complete circuit diagram of the detection system is given in Figures 70, 71, and 72.

The diagram of the actual circuit used in recording area modulated strip chart records is shown in Figure 73. The sum of the input signal, $g(t)$, and the 80 Hz sinusoidal voltage is inverted at the output of the operational amplifier. Thus, the positive half of this sum was clipped off, and the negative half was recorded on the rectilinear chart recorder. The principle of this area modulation recording technique is unchanged even though the modulated chart record is inverted.

The diagram of the electronic circuit used to intensity modulate the oscilloscope beam for producing the density modulated transparencies is given in Figure 74.
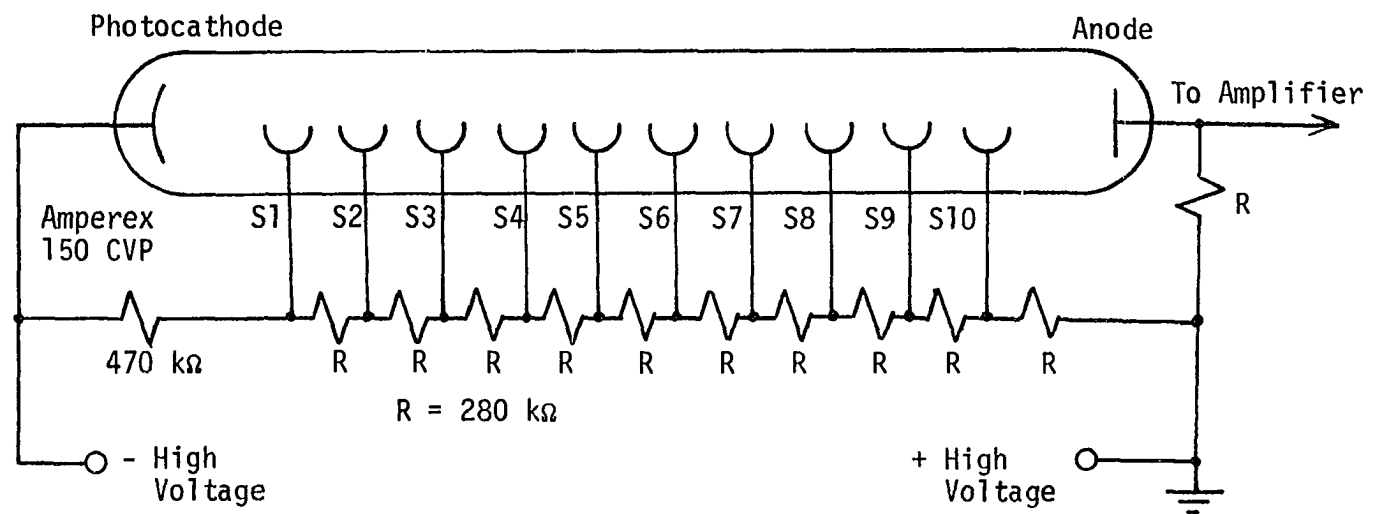
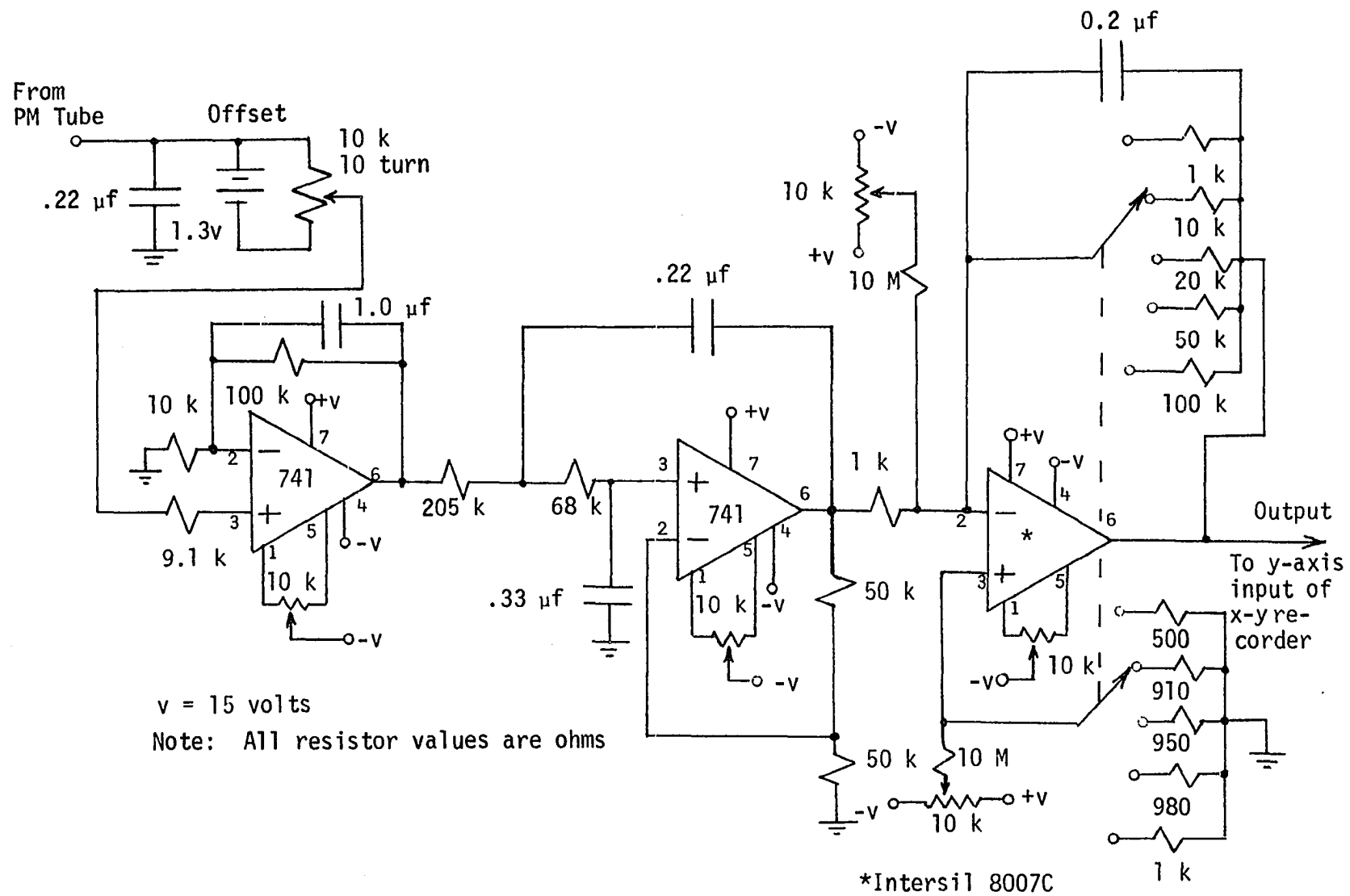Figure 70. Photomultiplier tube circuitry.

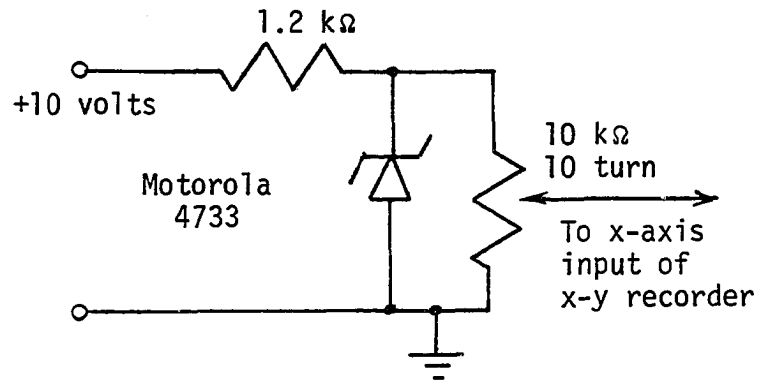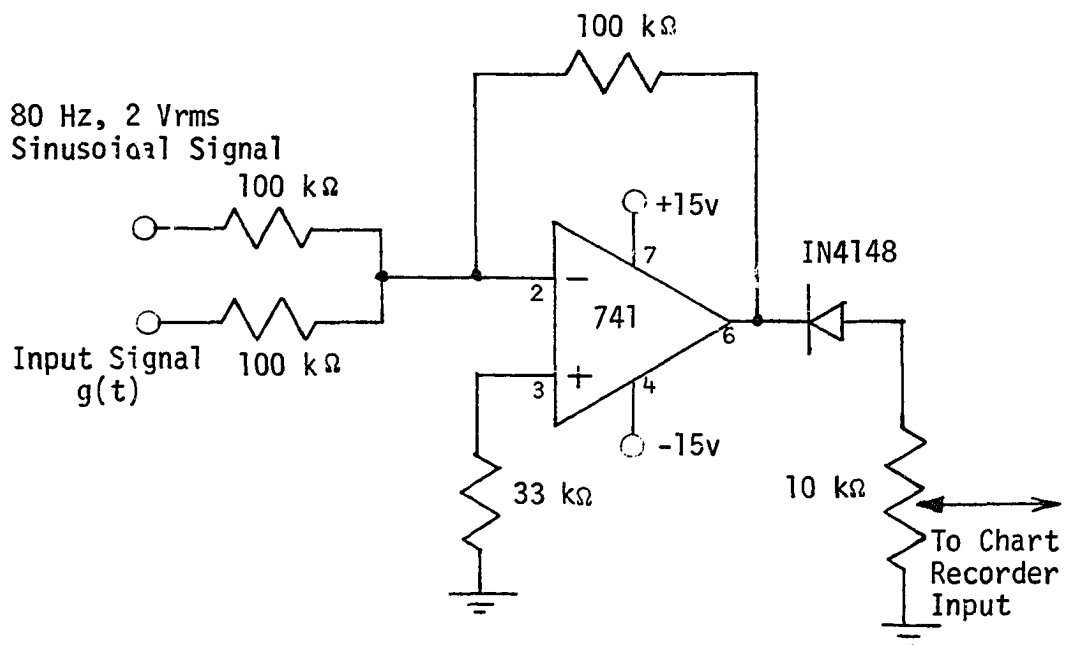Figure 71. Low frequency variable gain amplifier.

Figure 72. X-position detector circuit.

Figure 73. Circuit used to record area modulated chart records.

Figure 74. Circuit used to intensity modulate a CRT beam.